Università di Firenze, Università di Perugia, INdAM consorziate nel CIAFM

DOTTORATO DI RICERCA
IN MATEMATICA, INFORMATICA, STATISTICA

CURRICULUM IN MATEMATICA
CICLO XXXIII

Sede amministrativa Università degli Studi di Firenze
Coordinatore Prof. Paolo Salani

Approximation by operators and applications to Digital Images and to concrete real world problems

Settore Scientifico Disciplinare MAT/05

Dottorando:
Marco Seracini

Tutore
Prof. Gianluca Vinti

Coordinatore
Prof. Paolo Salani

Anni 2017/2020

"In theory there is no difference between theory and practice in practice there is."

— Yogi Berra

"Was sich überhaupt sagen läßt, läßt sich klar sagen; und wovon man nicht reden kann, darüber muß man schweigen."

— Ludwig Wittgenstein

Contents

[1] Results contained in this section are published in [48].
[2] Results contained in this section are published in [39, 40, 47].
[3] Results contained in this section are almost ready to be submitted.
[4] Results contained in this section are published in [7, 8].
[5] Results contained in this section have been submitted in [10, 11].

Acknowledgements

This thesis is the final product of three years of intense work.

At the end of this period, I would like to dedicate a few lines to some of those people who have been close to me during this path of personal and professional growth.

I thank my advisor Prof. Gianluca Vinti, whitout which nothing of what I did in these years could be possible.

I thank Prof. Carlo Bardaro for his suggestions, his precious support, and all the many things he taught me, together with the Analysis Research Group of the Department of Mathematics and Computer Science at the University of Perugia, with which I have worked during the whole period.

I thank Prof. Stephen Brown of MIT for his availability and his support during my permanence in USA, for his patience and all the interesting discussions he shared, and continues to share, with me.

I sincerely thank my parents and my brother Stefano for having been always at my side supporting me.

I thank my PhD colleagues for the sincere relationship we have established in this experience.

The last thought is to remember two people we are missing as from the professional point of view as for their deep humanity: Prof. Mimmo Candeloro and Prof. Carlo Casolo, both recently passed away.

Introduction

Starting from the 80's, thanks to the improvement of the computation power, the reduced dimension and the economical availability of computers, Signal Theory has increased its attention on multi dimensional data. In particular, image elaboration, concerning both processing as analysis, in static and dynamic conditions, has gained a meaningful importance in the scientific community. The bottleneck to pass from the pure mathematical theory, investigated years before, to the applications, is often represented by the impossibility to satisfy the hypothesis in real-world cases, so that approaches to negotiate the suitability of the results with the theoretical frameworks are needed. The resulting mathematical models on this respect should take into account of the multidimensional setting and of the necessary adaptation of the analytical theory in a discrete domain, a crucial passage for the reliability of the applications. This thesis reflects the above mentioned concepts dealing mainly with the applications of some approximation problems belonging to the area of Approximation Theory and Signal Processing, to real-world problems arising from medical and engineering fields through the implementation of some theoretical results for the reconstruction of digital images, suitable for the considered problems. In particular, the main topic concentrates on the theory of discrete linear operators of sampling type, considering in particular the so called Sampling Kantorovich (SK) operators, used as main mathematical instrument in order to reconstruct digital signals/images. In order to first frame the state of the art of the problem, the starting point is represented by the well known Whittaker-Kotelnikov-Shannon sampling theorem, whose formulation was firstly introduced around the years 50's [126, 106, 107, 84]. It reads as follows.

Theorem 1. *(WKS Sampling Theorem)*

Let $f \in L^2(\mathbb{R})$ such that supp $\widehat{f} \subseteq [-\pi w, \pi w]$, $w > 0$, where $\widehat{f}$ denotes the Fourier transform of the function f. Then

$$\sum_{k\in\mathbb{Z}} f\left(\frac{k}{w}\right) sinc(wt-k) \;=\; f(t), \qquad t \in \mathbb{R}.$$

The WKS sampling theorem states the conditions for the exact reconstruction of a function $f \in L^2(\mathbb{R})$, by means of the above interpolation formula given its samples values $f(\frac{k}{w})$ calculated in the, so called, nodes $\frac{k}{w}$. For an interesting discussion about the above formula, see e.g., [71]. Although this result has had a very strong impact both in the mathematical literature as in the applications, the theorem has both theoretical and applicative disadvantages. From the theoretical point of view, requiring that the function to be reconstructed belongs to L^2 (which means that the signal has finite energy), having its Fourier transform compact support (the signal is band-limited), means requiring (by the Paley-Wiener theorem [105]) that f is the restriction to the real axis of an entire function of exponential type, which in turns imply that the signal must be too regular, strongly restricting the field of action in the case of physical data (i.e., signals that in practice are

found). Moreover, from the applicative point of view, the above interpolation formula requires the knowledge of the samples values $f\left(\frac{k}{w}\right)$ all over $\mathbb{R}$, with k varying in all integers, thus requiring the sampling of the signal on infinite time nodes of it, which in practice is not possible; furthermore, the evaluation of the signal should be done both in the past of a fixed instant $t \in \mathbb{R}$ as in the future, which means making a prediction. Furthermore, in concrete application problems, signals are duration-limited (i.e. their extension in the domain is bounded) and this is not compatible with the requested band-limitation (this depends by the Heisenberg uncertainty principle). For these reasons, the assumptions of WKS sampling theorem need to be weakened.

Starting from the 60's, the mathematical community began to work on this problem with the price of losing the exact reconstruction but having instead an approximated reconstruction, that is, with some approximation errors to estimate.

In this direction, Weiss in 1963 [124] and Brown in 1967 [24] proved that

Theorem 2. *Let $f \in L^2(\mathbb{R}) \cap C(\mathbb{R})$ ($C(\mathbb{R})$ being the space of bounded and uniformly continuous functions) such that $\hat{f} \in L^1(\mathbb{R})$; then one has the following estimate for the approximation error*

$$|(S_w f)(t) - f(t)| \leq \sqrt{\frac{2}{\pi}} \int_{|v| \geq \pi w} \left|\hat{f}(v)\right| dv, t \in \mathbb{R}.$$

The above estimates imply the uniform convergence of $(S_w f)(t)$ towards f as $w \to +\infty$, since

$$\lim_{w \to +\infty} \int_{|v| \geq \pi w} \left|\hat{f}(v)\right| dv = 0,$$

being $\hat{f} \in L^1(\mathbb{R})$. It is also possible to prove that the constant $\sqrt{\frac{2}{\pi}}$ is optimal, in the sense that it can not be improved further. Moreover, the above inequality reveals, in terms of signals, the property of the operators $(S_w f)(t)$ to behave as low-pass filters: in fact, the integral on the right side, depends mainly on the high-frequency components of the Fourier transform $\hat{f}$ of the function f.

To further relax the WKS sampling assumptions, around 80's, a new class of operators, called generalized sampling operators, has been introduced by the famous mathematician P. L. Butzer and his school at RWTH-Aachen, with the aim to solve all the previous mentioned critical issues connected with the classical sampling theorem, (see e.g., [31, 32, 28]).

For a function $\varphi : \mathbb{R} \to \mathbb{R}$ with $\varphi \in C_c(\mathbb{R})$ and a bounded function $f : \mathbb{R} \to \mathbb{R}$, the generalized sampling operators are defined as

$$(S_w^{\varphi} f)(x) \ := \ \sum_{k \in \mathbb{Z}} f\left(\frac{k}{w}\right) \varphi(wx - k), \qquad x \in \mathbb{R}, \ w > 0.$$

The above operators are bounded linear operators mapping L^∞ into L^∞ and $C(\mathbb{R})$ into itself, with respect to the L^∞ and $C(\mathbb{R})$ norms, respectively. Here the operator norm is $\|S_W^{\varphi}\|_{[C(\mathbb{R}),C(\mathbb{R})]} = \sup_{u \in \mathbb{R}} \sum_{k \in \mathbb{Z}} |\varphi(u-k)|$, where $m_0(\varphi) = \sup_{u \in \mathbb{R}} \sum_{k \in \mathbb{Z}} |\varphi(u-k)|$ is the absolute discrete moment of order zero of the function φ.

Moreover, it is possible to prove that $(S_w^{\varphi} f)(x)$ converges to $f(x)$ as w tends to $+\infty$, when the kernel φ satisfy the following condition:

$$\sum_{k \in \mathbb{Z}} \varphi(x - k) \ = \ 1,$$

for every $x \in \mathbb{R}$, and in every point x of continuity for f (when f is bounded and continuous) and uniformly with respect to x (when f is bounded and uniformly continuous). This represents the so called generalized sampling theorem.

The generalized sampling formulation has, compared to the classical WKS sampling theorem, the advantages to require only a finite number of samples, that in addition, can be taken only in the past with respect to the point to reconstruct (this last result being valid assuming $\varphi \in C_c(\mathbb{R}^+)$). As it is natural to expect, the weakening of the hypotheses has its downside, represented by the introduction of an error in the reconstruction of f. Controlling this error is important to quantify the goodness of the reconstruction: for these reasons, besides results of convergence, there are results of order of approximation, higher order derivatives, saturation and many others (see e.g., [30, 31, 32, 121, 28]). For the extension to the theory in multidimensional setting, see [27].

Although the theory of reconstruction using these operators has solved all the drawbacks of the formula of the classical sampling theorem, considerably weakening the hypotheses, these operators are not very suitable to be studied in a context of functions/signals that are not necessarily continuous. In fact, it is not difficult to show (see the counterexample in [15]) that they do not map L^p into itself, that is, they are not continuous in L^p; and indeed their expression shows how strongly they are related to the evaluation of the function on single nodes $\frac{k}{w}, k \in \mathbb{Z}, w > 0$. To overcome this problem, to lead the way for a theory that would allow the reconstruction of a more broad class of signals (therefore not necessarily restricted to $C(R)$), in [15] the Sampling Kantorovich (SK) operators have been introduced and studied.

In the one-dimensional case and (for a sake of simplicity) for equi-spaced sampling, given a locally integrable function, they are defined as

$$(K_w^\chi f)(x) := \sum_{k=-\infty}^{\infty} \Big\{ w \int_{k/w}^{(k+1)/w} f(u)\, du \Big\} \chi(wx - k) \quad x \in \mathbb{R}, w > 0, \tag{1}$$

where $f : \mathbb{R} \to \mathbb{R}$ is such that the above series converges for every $x \in \mathbb{R}$, and χ is a kernel function. Under suitable assumptions on χ, it is possible to prove convergence results for the above operators.

In this thesis, dealing with applications, we are more interested to the extension of the above operators in a multivariate setting where we may now define the multidimensional sampling Kantorovich operators as

$$(K_w^\chi f)(\underline{x}) \ := \ \sum_{\underline{k} \in \mathbb{Z}^n} \chi(w\underline{x} - \underline{k}) \cdot \left[\frac{w^n}{A_{\underline{k}}} \cdot \int_{R_{\underline{k}}^w} f(\underline{u})\ d\underline{u} \right] \quad \underline{x} \in \mathbb{R}^n, w > 0,$$

where $R_{\underline{k}}^w = \left[\frac{t_{k_1}}{w}, \frac{t_{k_1+1}}{w}\right] \times \left[\frac{t_{k_2}}{w}, \frac{t_{k_2+1}}{w}\right] \times ... \times \left[\frac{t_{k_n}}{w}, \frac{t_{k_n+1}}{w}\right]$, $A_{\underline{k}} := \Delta_{k_1} \cdots \Delta_{k_n}$, $\Delta_{k_i} := t_{k_i+1} - t_{k_i}$ and $f : \mathbb{R}^n \to \mathbb{R}$ is a locally integrable function such that the above series converges for every $\underline{x} \in \mathbb{R}^n$.

For the above SK operators, the following results have been provided [49].

Theorem 3. *Let $f : \mathbb{R}^n \to \mathbb{R}$ be a bounded and continuous function. Under suitable assumptions on the kernel χ, for each $\underline{x} \in \mathbb{R}^n$ there holds*

$$\lim_{w \to \infty} (K_w^\chi f)(\underline{x}) \ = \ f(\underline{x}).$$

Moreover, if f is uniformly continuous and bounded, there holds

$$\lim_{w\to\infty} \|K_w^\chi f - f\|_\infty \;=\; 0.$$

Moreover, recalling the main motivation that stimulated the introduction and the study of the SK operators, results in Orlicz spaces[6] have been proved, from which we can deduce, as a particular case, the following convergence theorem in L^p.

Theorem 4. *Let χ be a kernel satisfying suitable assumption and let $f : \mathbb{R}^n \to \mathbb{R}, f \in L^p, p \geq 1$. Then $K_w^\chi f \in L^p$, and there holds*

$$\lim_{w\to\infty} \|K_w^\chi f - f\|_p = 0.$$

Moreover, order of approximation results, inverse and saturation results and Voronoskaja type formulas for the exact order of approximation, have been proved in [50, 52, 53].

In addition, the pointwise behaviour of SK operators in the discontinuity points, has been also studied in [45].

Supported by solid theoretical basis, the theory of the SK operators has been implemented. The algorithmic implementation, firstly introduced in [49], has been rewritten in different programming languages (C++, Python, Php, Matlab) and optimized until to reach a good computational complexity: this optimization has reduced considerably the execution time [48]. Furthermore, it offers a realistic model for the effective sampling process, thanks to which the quality of signal reconstruction exceeds other methods extensively investigated in literature, as proved in [48]. It should be pointed out that the effect of the reconstruction through the SK operators confers, on the one hand an increase in the resolution and, on the other hand, an elimination of the noises caused by high frequencies. In other words, the SK operators act as "microscopes" and as low pass filters at the same time.

In particular, in Chapter 2, Section 2.3, working with 2D digital images, the behavior of the SK operators has been numerically compared with bilinear and bicubic interpolation besides Finite Impulse Response (FIR) and Infinite Impulse Response (IIR) quasi-interpolation methods (for these last quasi-interpolation method, see e.g., [43]). The achieved results stated that SK operators have better performance for signal reconstruction compared to the other considered ones [48].

Thanks to the reduction of the algorithmic computational cost of the SK operators above mentioned, it has been possible to apply the SK operators for the innovative solution of some real-world problems in the Medical as in the Engineering fields: the proposed methodologies matched together the SK operators with other Digital Image Processing (DIP) algorithms.

From the medical point of view, in Chapter 3, Section 3.1., the segmentation of the pervious lumen of the aorta artery without contrast medium introduction has been performed [39, 40, 47]. Here the first crucial step is given by the reconstruction of the considered CT images by means of SK operators. Then segmentation algorithms were designed and implemented. Finally, a single algorithm has been developed that allows in a short time (about 9 seconds per image) to reconstruct and to segment the patient lumen of the aneurysmal aortic vessel. Results analyzed by Dice, Tanimoto and other similarity indexes available in literature, as well as by Hausdorff distance and some problem-specific parameters, have shown a good matching with the contrast medium CT image sequences. i.e., the gold standard reference (see Fig.1); moreover, an improvement in the segmentation with respect to images not processed by the SK algorithm, has been shown.

[6] The Orlicz spaces have beeen introduced in the years 30's by the Polish mathematician W. Orlicz, as natural extension of L^p-spaces and they play a fundamental role in Functional Analysis as in many other branches of Mathematical Analysis where these spaces find various applications.

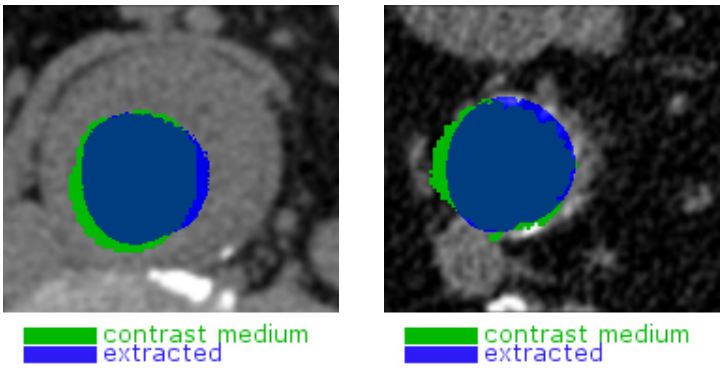

Figure 1. Two examples of the comparison between the segmented pervious lumen of the aorta artery without contrast medium extracted after the application of SK algorithm (in blue) and the corresponding contrast medium gold standard reference (in green). The quality of the matching is evident.

To the knowledge of the author, this has been the first attempt, proved in literature, to segment pervious lumen of occluded vessels without contrast medium introduction.

In the ophthalmological field (Chapter 3, Section 3.2), SK algorithm has been used to enhance the visualization of images of the retinal fundus, achieved by Optical Coherence Tomography of the Superficial Capillary Plexus (SCP) as of the Choriocapillaris tissue (CC). The obtained results have been evaluated as qualitatively by medical specialists as quantitatively using cluster counting, Shannon Entropy and co-occurrences matrices. The comparison to estimate the parameters was made using fluorangiography as the gold standard for the SCP images, while the histological specimens of cadavers, for the CC images. In both cases the improvement has been meaningful (see Fig. 2). Here a new hybrid thresholding method, suitable for the problem under consideration, has been introduced in order to distinguish the macula from the capillary plexus as faithfully as possible.

For what concerns the engineering applications, in Chapter 4 two main problems have been examined: the first one related to the segmentation of thermal bridges (Section 4.1), the second one connected with the study of acoustic bridges (Section 4.2).

Thermal bridges are areas of buildings where constructive elements exhibit a high gradient of temperature. The presence of these areas results in an energy loss for the building. Precisely, estimating the contours of thermal bridges allows to quantify the amount of these losses (see Fig. 3). It has been proved that, using SK algorithms on thermographic images, together with suitable segmentation methods, improves the correctness of estimation from 3% to 11% compared to not SK reconstructed data [7, 8].

Similarly to thermal bridges, acoustic bridges are zones of the environment where the presence of noise sources determines strong variations of acoustic power[7] (see Fig. 4). These variations give rise to environmental pollution. Their individuation allows to reduce the effect of noise sources on the neighborhood. Using SK algorithm together with a well suited triangulation method, has proved to be efficient in the three-dimensional localization of such sources of noise. The estimated error in the case study has been quantified to be around $46cm$ at a distance from the source of $12.25m$, i.e., around 4%.

[7]The individuation of acoustic bridges is not restricted to environmental noise but can be conducted in many other investigation areas, e.g., engine diagnostic.

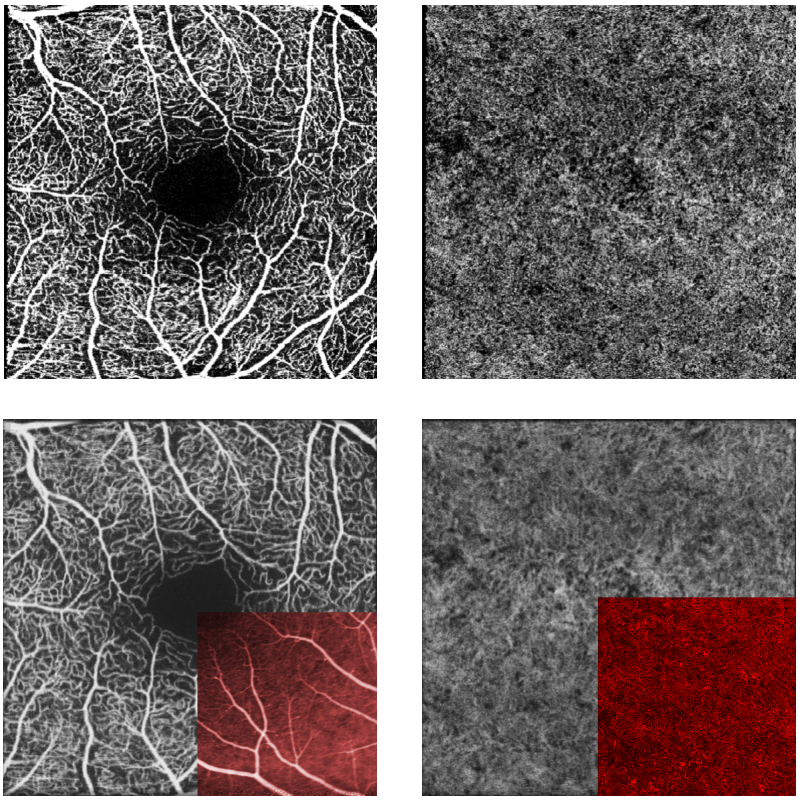

Figure 2. From left to right: Superficial Capillary Plexus and Choriocapillaris tissue. In the first row the original Optical Coherence Tomography images, in the second row the images processed by means of SK algorithm. The qualitative visual improvement is evident. The small red squares in the images of the second row are the fluoroangiographic and the autoptic references.

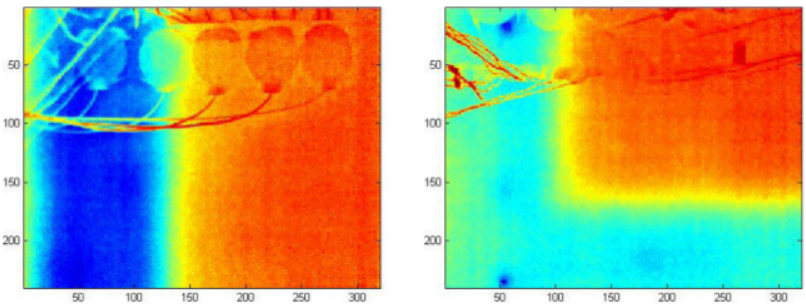

Figure 3. Examples of thermal bridges acquired by a thermal camera: pillar (left), beam-pillar-joint (right). The red zones are the ones with higher temperature.

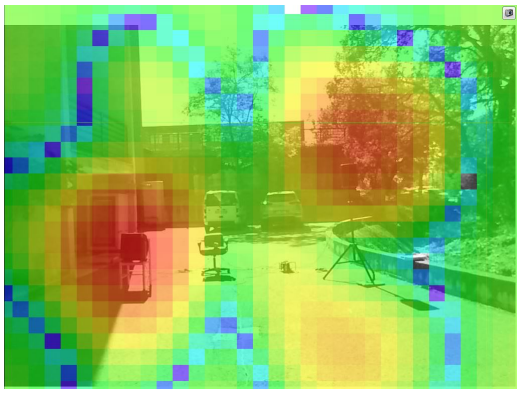

Figure 4. Experimental data of an acoustic bridge recorded by an Acoustic Camera (AC). The round red areas are the ones where the sound pressure is bigger, corresponding to two speakers in the experimental setup.

The whole thesis is structured as follows: Chapter 1 provides a summary of some arguments that have been valued fundamental for the self-contained character of the thesis; in Chapter 2 the theory behind the SK operator is reviewed, with particular attention to its multidimensional formulations. Here the implementation of the reconstruction algorithm for digital images by the SK operators has been obtained and the numerical results demonstrating the good performances of the SK algorithm have been discussed. Chapters 3 and 4 represent the part of the thesis dedicated to concrete applications to real world problems, as discussed above. The thesis ends with the conclusions that outline, in a summarizing fashion, the original achieved results.

Chapter 1

Preliminary Overview

In this first chapter an overview of topics, whose knowledge is necessary to make this thesis self contained, is presented. The reader who is familiar with Fourier Analysis, Approximation Theory, Sampling, Image processing and Filtering can skip this section.

1.1 Fourier Transform

The theoretical tool mostly used in Signal Theory is the Fourier Transform (FT), introduced by Jean Baptiste Joseph Fourier in 1822, in his work *Théorie analytique de la chaleur* [66].

Given $f_{2\pi}$, a periodic function of period 2π, such that $f_{2\pi} \in L^2[-\pi, \pi]$, where $L^2[-\pi, \pi]$ is the set of 2π periodic square summable functions in the closed interval $[-\pi, \pi]$, the best approximation of $f_{2\pi}$, in the space generated by the orthonormal system $\mathcal{S}_N = \{\varphi_0, \varphi_1, ..., \varphi_N\}$ of $L^2[-\pi, \pi]$, is expressed by

$$s_n(x) = \sum_{k=0}^{n} \hat{f}_k \varphi_k(x)$$

and it is called the partial sum of the Fourier series associated with $f_{2\pi}$, where $\hat{f}_k, k = 0, 1, ..., n$ are the Fourier coefficients whose values depend on $f_{2\pi}$ and $\mathcal{S}_N$.

In the particular case of the real trigonometric system (i.e., $\mathcal{S}_N = \{\cos(kx), \sin(kx)\}$, $k = 0, 1, 2, ...n$), the following equality stands

$$f_{2\pi} = \frac{1}{2}\hat{f}_c(0) + \sum_{k=1}^{\infty}(\hat{f}_c \cos(kx) + \hat{f}_s \sin(kx)) \tag{1.1}$$

with

$$\hat{f}_c(k) = \frac{1}{\pi}\int_{-\pi}^{\pi} f_{2\pi}(x)\cos(kx)dx, k = 0, 1, 2, ...,$$

and

$$\hat{f}_s(k) = \frac{1}{\pi}\int_{-\pi}^{\pi} f_{2\pi}(x)\sin(kx)dx, k = 1, 2, ...$$

The equality expressed in (1.1) defines the trigonometric Fourier series of $f_{2\pi}$. Using an exponential notation, it is possible to rewrite

$$f_{2\pi} = \sum_{k=-\infty}^{+\infty} c_k e^{ikx}, \tag{1.2}$$

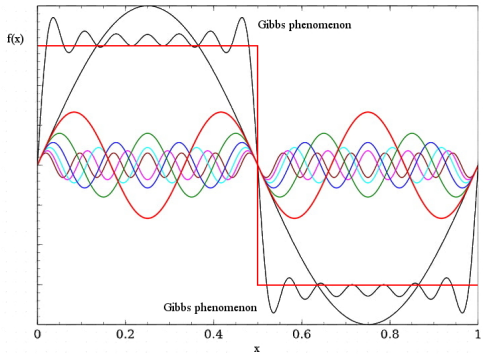

Figure 1.1. Decomposition by the Fourier series of a periodic square wave in its first 7 ($\sin(\cdot)$, $\cos(\cdot)$) components. The function to reconstruct is the unitary square wave, in figure denoted by $f(x)$ (in red). The signal resulting after the reconstruction exhibits the so called Gibbs phenomenon, i.e., an undesired oscillation due to the truncation of the series (in this specific case to the 7^{th} term).

with $c_k = \frac{1}{2\pi}\int_{-\pi}^{\pi} f_{2\pi}(u)e^{-iku}du, k \in \mathbb{Z}$. The equation (1.2) is the complex form of the Fourier series of $f_{2\pi}$ [130].

In a similar fashion, it is possible to extend the Fourier expansion to not periodic functions. Given $f \in L^1(\mathbb{R})$, the function

$$\hat{f}(\lambda) = \int_{-\infty}^{+\infty} f(t)e^{-i\lambda t}dt$$

defines the Fourier transform (FT) of f.

In each point $x \in \mathbb{R}$ such that the Dini's[1] condition is satisfied, it is possible to define the Inverse Fourier Transform (IFT) of f given by

$$f(x) = \frac{1}{\sqrt{2\pi}}(P.V.)\int_{-\infty}^{+\infty} \hat{f}(\lambda)e^{i\lambda x}d\lambda,$$

where (P.V.) denotes the principal value of the integral [29, 123].

What has been introduced in $\mathbb{R}$ can be obviously extended to $\mathbb{R}^n$, $n \geq 1$.

From a physical point of view, the variable λ expresses the pulsation (related to the frequency of oscillation (ν) by the relation $\nu = 2\pi\lambda$) and the FT shows the way to reconstruct the original function f by the combination of oscillating functions[2].

More than one century later Whittaker, Kotelnikov and Shannon will demonstrate how to reconstruct a function f starting by the knowledge of a set of sampled points. The Fourier Transform theory, as given in its original form, can be formulated in $L^p(\mathbb{R})$ spaces with $1 < p \leq 2$.

On the other hand, introducing the theory of distributions, it is possible to extend the theory of FT to a wider class of functions belonging to $L^p(\mathbb{R})$, with $p > 2$. This approach is particularly useful when a real signal is modeled by e.g., a Dirac impulse, an Heaviside step function or other theoretical models.

In Figure 1.1 the first seven terms of the Fourier series associated to the periodic square wave are shown.

[1] Dini's condition requires that with $f \in L^1$, exists $x_0 \in \mathbb{R}$ and exists $\delta \in]0, a[$, with $a \in \mathbb{R}$ conveniently chosen, such that $\int_0^\delta |f(x_0+u)+f(x_0-u)-2f(x_0)|u^{-1}du < +\infty$.

[2] From the well known Euler's formula $e^{ix} = \cos(x) + i \cdot \sin(x)$.

Further result connected with the FT concerns the convolution product. Given two measurable functions f and g defined on $\mathbb{R}$, their convolution product is defined as

$$(f * g)(x) = \int_{-\infty}^{+\infty} f(x-u)g(u)du \quad .$$

There holds the following result.

Theorem 5. *Given $f, g \in L^1(\mathbb{R})$, then $f * g \in L^1(\mathbb{R})$ and*

$$\widehat{(f * g)}(x) = \hat{f}(x)\,\hat{g}(x)$$

Theorem 5 describes the equivalence between the convolution product in the time domain with the usual product in the frequency domain. Another version of the theorem provides the same result in case of periodic functions, the difference being only in a normalization term [29, 123, 65].

1.2 Classical Sampling Theorem

The capacity to reconstruct a signal, only starting from the knowledge of a set of samples, has always been a fascinating problem, not only theoretical but with substantial practical implications (e.g. signal transmission and elaboration).

Historically, the first and most important result has been formalized in the years between '30s and '50s of the twentieth century and today it takes the name of three scientists who independently reached a similar result: the British mathematician Edmund Taylor Whittaker, the Russian engineer Vladimir Kotelnikov and the American engineer and mathematician Claude Elwood Shannon.

Given a continuous function $f \in L^2(\mathbb{R})$, such that $\hat{f}(\lambda)$ has a compact support, i.e., $\hat{f}(\lambda) = 0$, for every $|\lambda| > \lambda_0 \in \mathbb{R}$ (band-limited), the classical form of the so called WKS sampling theorem stands.

Theorem 6. *Given $T = \frac{\pi}{\lambda_0}$, for every $t \in \mathbb{R}$*

$$f(t) = \sum_{k=-\infty}^{+\infty} f(nT)\frac{\sin(\lambda_0 t - n\pi)}{\lambda_0 t - n\pi} = \sum_{k=-\infty}^{+\infty} f(nT)\mathrm{sinc}\left(\frac{\lambda_0 t}{\pi} - n\right)$$

where T is said to be the sampling period and the sinc$(\cdot)$ function is defined as follows:

$$\mathrm{sinc}(x) = \begin{cases} 1, \text{ if } x = 0; \\ \dfrac{\sin(\pi x)}{\pi x}, \text{ otherwise.} \end{cases}$$

An equivalent set of hypothesis for the WKS sampling theorem prescribes that f must have finite energy ($f \in L^2(\mathbb{R})$) and be band-limited [72].

The WKS sampling theorem expresses the possibility to reconstruct a function having suitable properties, starting from the knowledge of a set of discrete values, multiplying the value of each sample for suitable shifted version of a sinc$(\cdot)$ function. The shifted sinc$(\cdot)$ functions play the role of an orthonormal set in $\mathbb{R}$, the same way the Fourier coefficients, together with the sin$(\cdot)$ and cos$(\cdot)$,

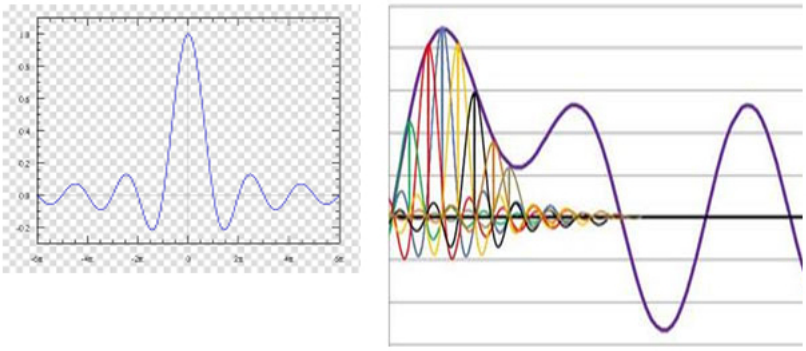

Figure 1.2. Partial decomposition of a generic signal using a set of shifted sinc(·) functions (on the right). The graphic of a centered sinc(·) function is on the left of the figure.

behave in the trigonometric Fourier series.

The value for the sampling period T must satisfy the so called Nyquist criterion [93, 94]:

$$\frac{1}{T} \geq 2\nu_{max} \,. \tag{1.3}$$

where ν_{max} is the maximum frequency in the signal to be reconstructed. If condition (1.3) is violated, spectral replicas overlap in the FT domain, causing aliasing, i.e., the generation of artifacts corrupting the original function (see Figure 1.3). Despite its elegant mathematical formulation and the assurance of an exact reconstruction, the WKS sampling theorem hides some limitations for its concrete applicability [32]:

- the finite energy and the band-limited conditions imply that f must be the restriction, to the real axis, of an entire function of exponential type;
- an infinite number of samples is needed for the reconstruction;
- the reconstruction is possible depending on the knowledge of samples also in the future, with respect to the point to reconstruct;
- due to the Heisenberg principle, real signals can not be simultaneously band-limited and duration-limited (i.e., the domain is bounded).

To tackle these limitations, an approximated version of the WKS sampling theorem has been formalized, as will be more accurately explained in the section relative to the Generalized Sampling Theorem.

Figure 1.3. Aliasing effect (image on the right) in the high frequencies band of the signal. The sampling rate is too low compared to the spectral content of the original image (on the left). Image courtesy of prof. Fredo Durant, MIT CSAIL.

1.3 Generalized Sampling Theorem

To overpass the limitations of the WKS sampling theorem, a generalized formulation has been introduced in the 80's by P. L. Butzer et al. [31, 32, 28, 26]. The main idea consisted in replacing the $\mathrm{sinc}(\cdot)$ function with another class of functions, having certain properties needed for the convergence. These functions $\varphi : \mathbb{R} \to \mathbb{R}$, are called *kernels* and they satisfy the conditions

(φ_1) $\varphi \in C_c(\mathbb{R})$ (the space of continuous functions with compact support);

(φ_2) $\displaystyle\sum_{k=-\infty}^{+\infty} \varphi(u-k) = 1$, for every $u \in \mathbb{R}$.

Given the above kernel φ and a function $f \in C(\mathbb{R})$, it is possible to define the generalized sampling operator:

$$(S_w^{\varphi} f)(t) := \sum_{k=-\infty}^{+\infty} f\left(\frac{k}{w}\right) \varphi(wt-k),\ t \in \mathbb{R}.$$

Given a kernel function, the singularity condition (φ_2) is not so easy to be verified. The following theorem proves the equivalence with another condition, expressed in terms of the Fourier transform.

Theorem 7. *Given $\varphi \in C_c(\mathbb{R})$, then*

$$\sum_{k=-\infty}^{+\infty} \varphi(u-k) = 1, \text{ for every } u \in \mathbb{R} \Longleftrightarrow \sqrt{2\pi}\hat{\varphi}(2k\pi) = \begin{cases} 1, \text{ if } k = 0; \\ 0, \text{ if } k \in \mathbb{Z}, \end{cases}$$

where $\hat{\varphi}$ is the FT of φ.

Denoting the absolute discrete moment of order zero as $m_0(\varphi) := \sup_{u\in\mathbb{R}} \sum_{k=-\infty}^{+\infty} |\varphi(u-k)|$, it is possible to prove that the generalized sampling operator is well defined in $C(\mathbb{R})$. In fact,

$$|(S_w^{\varphi} f)(t)| \leq \sum_{k\in\mathbb{Z}} \left| f\left(\frac{k}{w}\right) \right| |\varphi(wt-k)| \leq \|f\|_{\infty} m_0(\varphi) < +\infty,$$

where the last inequality holds being $f \in C(\mathbb{R})$, $m_0(\varphi) < +\infty$ (since $\varphi \in C_c(\mathbb{R})$), and passing to the supremum on the left hand-side.

Moreover, the following convergence result stands.

Theorem 8. *Let φ be a kernel. If the bounded function $f : \mathbb{R} \to \mathbb{R}$ is continuous in $t_0 \in \mathbb{R}$, then*

$$\lim_{w\to+\infty} (S_w^{\varphi} f)(t_0) = f(t_0). \tag{1.4}$$

In addition, if $f \in C(\mathbb{R})$, then

$$\lim_{w\to+\infty} \|S_w^{\varphi} f - f\|_{\infty} = 0. \tag{1.5}$$

Proof. To prove (1.4), being f continuous in t_0, for each $\varepsilon > 0$ there exists $\delta > 0$ such that, if $|t_0 - k/w| < \delta$ then $|f(t_0) - f(k/w)| < \varepsilon$. Using φ_2, it is possible to write

$$|f(t_0) - (S_w^{\varphi} f)(t_0)| = \left| \sum_{k=-\infty}^{+\infty} f(t_0)\varphi(wt_0 - k) - \sum_{k=-\infty}^{+\infty} f\left(\frac{k}{w}\right) \varphi(wt_0 - k) \right|$$

$$\leq \sum_{k=-\infty}^{+\infty} \left| f\left(\frac{k}{w}\right) - f(t_0) \right| |\varphi(wt_0 - k)|$$

$$= \left(\sum_{|wt_0-k|<\delta w} + \sum_{|wt_0-k|\geq\delta w} \right) \left| f(t_0) - f(\frac{k}{w}) \right| |\varphi(wt_0 - k)| =: I_1 + I_2$$

with $w > 0$. For I_1 there holds

$$I_1 \leq \varepsilon \sum_{|wt_0-k|<\delta w} |\varphi(wt_0 - k)| \leq \varepsilon\, m_0(\varphi)$$

with $w > 0$. For I_2, being $w > 0$ big enough such that $wt_0 - k \notin [-\delta w, \delta w]$, and $supp\, \varphi \subset [-\delta w, \delta w]$, then $I_2 = 0$. The thesis follows by the arbitrariness of ε.

Analogously, it is possible to prove (1.5) replacing the continuity condition by the uniform continuity of f. □

The following corollary shows how it is possible to reconstruct the function f using only values in the past.

Corollary 1.3.1. *Given $\varphi \in C_c(\mathbb{R})$ with supp $\varphi \subset \mathbb{R}^+$ and such that condition (φ_2) holds, then for each bounded $f : \mathbb{R} \to \mathbb{R}$, in the points of continuity t_0, there holds*

$$\lim_{w \to +\infty} (S_w^{\varphi} f)(t_0) = \sum_{\frac{k}{w} < t_0} f\left(\frac{k}{w}\right) \varphi(wt_0 - k) = f(t_0).$$

Proof. Being $\varphi(wt_0 - k) = 0$ for $\frac{k}{w} \geq t_0$, then

$$(S_w^{\varphi} f)(t_0) = \sum_{\frac{k}{w} < t_0} f\left(\frac{k}{w}\right) \varphi(wt_0 - k).$$

The thesis follows from the previous theorem. □

In 1987, P.L. Butzer, S.Ries and R.L. Stens proved that the generalized sampling operators do not converge to f in its points of discontinuity. For details see [30].

1.4 Digital Images

Digital images play a fundamental role in information theory and signal processing. Their visual information are stored on electronic media and are elaborated by computer science algorithms. For these reasons, a coherent introduction to the digital images topic needs a multidisciplinary approach.

By the mathematical point of view, a grayscale digital image is a bidimensional function I (equivalently a signal) from a discrete domain to a discrete range, formally:

$$I : L \times M \to C$$

with $L, M, C \subset \mathbb{N}$.

The mathematical model assuming $L, M, C \subset \mathbb{N}$ descends by the hypothesis that, in reality, an image is bounded in geometrical size and in the number of admissible gray values, until a certain extent practically proportional to the luminosity at each pixel. The luminosity signal is recorded thanks to suitable sensors (e.g., photodiodes), able to generate an electric signal (usually a tension) proportional to the amount of light they are excited by.

From the Computer Science point of view, each couple $(i, j) \in L \times M$ individuates the position of the corresponding pixel, whose coordinates are measured respect to a reference, conventionally fixed in the top left corner of the image itself (this convention is inherited from the standard mathematical matricial notation). Without loss of generality and with the aim to simplify the image processing procedures, whatever digital image is assumed to be rectangular, i.e., associated to a $L \times M$ matrix. More irregular shapes are constructed marking the set of pixels not belonging to the image as "undefined" (e.g., using a negative value).

The grayscale attribute, used to distinguish "black and white" images from colored ones, specifies the property of such type of images to be represented by one single luminosity channel, i.e., using a single matrix. Color type images need more than one channel (e.g., three in the RGB encoding), each one representing the intensity value of a fundamental color (usually red, green[3], blue). In figure 1.4 an example of grayscale image with the corresponding matrix is shown. In figure 1.5 an example of color scale image and its decomposition [68]

[3]Strictly speaking, green is not a fundamental color but it is used in place of yellow (that in the green color is contained) because of reduction of measurement errors, descending from the frequency band occupied by the yellow color in the light spectrum.

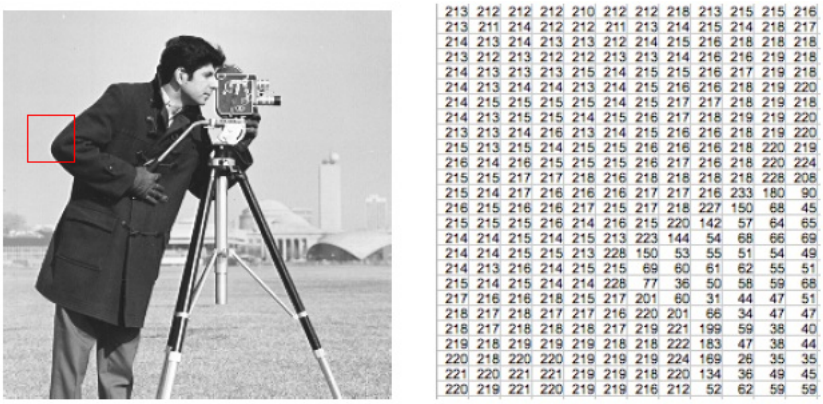

213	212	212	212	210	212	212	218	213	215	215	216
213	211	214	212	212	211	213	214	215	214	218	217
214	213	214	213	213	212	214	215	216	218	218	218
213	212	213	212	212	213	213	214	216	216	219	218
214	213	213	213	215	214	215	215	216	217	219	218
214	213	214	214	213	214	215	216	216	218	219	220
214	215	215	215	215	214	215	217	217	218	219	218
214	213	215	215	214	215	216	217	218	219	219	220
213	213	214	216	213	214	215	216	216	218	219	220
215	213	215	214	215	215	216	216	216	218	220	219
216	214	216	215	215	215	216	217	216	218	220	224
215	215	217	217	218	216	218	218	218	218	228	208
215	214	217	216	216	216	217	217	216	233	180	90
216	215	216	216	217	215	217	218	227	150	68	45
215	215	215	216	214	216	215	220	142	57	64	65
214	214	215	214	215	213	223	144	54	68	66	69
214	214	215	215	213	228	150	53	55	51	54	49
214	213	216	214	215	215	69	60	61	62	55	51
215	214	215	214	214	228	77	36	50	58	59	68
217	216	216	218	215	217	201	60	31	44	47	51
218	217	218	217	217	216	220	201	66	34	47	47
218	217	218	218	218	217	219	221	199	59	38	40
219	218	219	219	219	218	218	222	183	47	38	44
220	218	220	220	219	219	219	224	169	26	35	35
221	220	221	221	219	219	218	220	134	36	49	45
220	219	221	220	219	219	216	212	52	62	59	59

Figure 1.4. Grayscale image and its matricial representation. The matrix represents the luminosity of the red bounded area in the original image on the left.

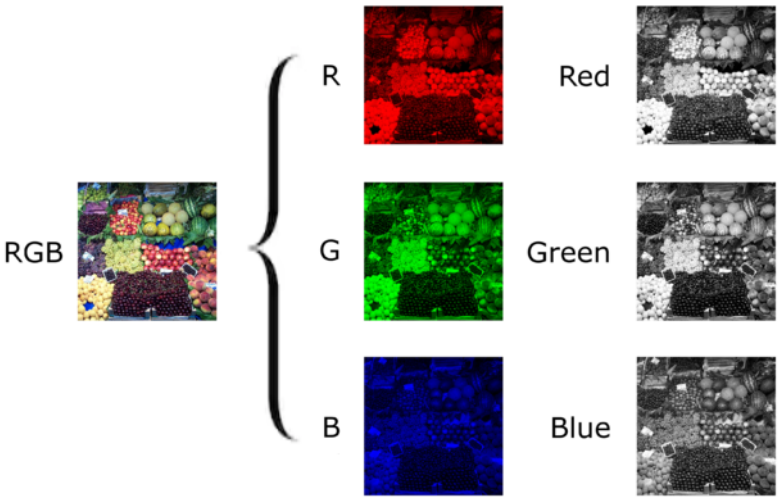

Figure 1.5. Decomposition of a native color image (on the left) in its corresponding RGB components.The last row on the right represents the luminosity (read intensity), expressed in graylevels, of each color for each channel.

In cases of 8 bit coding, $C = [0, 255]$, such that the luminance can assume 256 different gray levels ($2^8 = 256$). For medical devices, this value increases to 12 bits, resulting in $2^{12} = 4096$ possible different combinations ($C = [0, 4095]$) [14].

Digital images can be acquired directly in digital form (native digital camera) or converted into digital by an appropriate analog to digital (A/D) converter [96] (e.g. photographic scanner). The A/D conversion has the advantage of a noise reduction on the acquired signal but pays the price of a reduced resolution, due to the lower number of possible luminance values.

From a mathematical modeling point of view, a digital grayscale image can be represented using a step function $I \in L^p(\mathbb{R}^2)$, $1 \leq p < +\infty$, formally defined as [47]

$$I(x, y) := \sum_{i=1}^{N} \sum_{j=1}^{M} a_{ij} \cdot 1_{ij}(x, y) \ \ ((x, y) \in \mathbb{R}),$$

where $1_{ij}(x, y)$, $i = 1, 2, ..., L$, $j = 1, 2, ..., M$ are the characteristic functions of the sets $(i-1, i] \times (j-1, j]$ (i.e., $1_{ij}(x, y) = 1$, for $(x, y) \in (i-1, i] \times (j-1, j]$ and $1_{ij}(x, y) = 0$ otherwise). The above function $I(x, y)$ is defined in such a way that, to every pixel (i, j) the corresponding gray level a_{ij} is associated. This model will be particularly useful to guarantee the convergence of the SK operators in continuity points (see Chapter 2 for more details).

Operations modifying images (and signals in general) are referred as filters [103]. Filters take in input the original signal and provide its elaborated version. This process can present different characteristics, depending on the type of used filter. Some of these features are linearity, time invariance and causality. When a filter is linear, its effect on the input signal $f_I(t)$ can be modeled by a convolution product: using $h(t)$ to describe the filter behavior in the time domain t, the output signal $f_O(t)$ is given by (assuming to work in unidimensional setting):

$$f_O(t) = \int_{-\infty}^{+\infty} f_I(t-u)h(u)du = f_I(t) * h(t) \tag{1.6}$$

Assuming $f_I(t)$ and $h(t)$ Fourier transformable, equation 1.6 can be rewritten in frequency domain as :

$$\hat{f_O}(\lambda) = \hat{f}_I(\lambda)H(\lambda),$$

being $H(\lambda) = \hat{h}(t)$ the transfer function of the filter. The function $h(t)$ is called the *impulsive response* of the filter and it expresses the filter output to a Dirac impulse in input. Results are naturally extensible to higher dimensional spaces, as for images. In this case the frequency represents the geometrical size of the details (small details=high frequencies). If the filter is time invariant its transfer function does not change in time. Causal filters have the characteristic to have their outputs depending only on past and present inputs (a filter described by a sinc$(\cdot)$ function, as in the WKS sampling theorem, is an example of not causal filter). Classical example of linear filters is the mean filter, providing in output the mean value of the input signal. The median filter, calculating the median value of the input signal is, on the other hand, an example of not linear filter. In the frequency domain the result of a filtering procedure is the modification of the frequential content of the signal.

Due to the importance of the filtering process (e.g., noise suppression, signal transmission, interpolation and quasi interpolation and many others) several techniques have been introduced and the originating filters accordingly classified (e.g., Kalman, Butterworth, FIR, IIR). Here a short review of the Finite Impulse Response (FIR) filters and Infinite Impulse Response (IIR) filters is given.

FIR filters are a linear class of filters and, as the adjective *finite* suggests, their *impulsive responses* have compact support. In discrete setting, the impulsive response takes discrete values in the general

form:

$$h[n] = \sum_{i=0}^{N} b_i \cdot \delta[n-i] = b_n \, .$$

where N is the order of the filter, $b_i \in \mathbb{C}$ and δ is the Dirac delta function. In case of causal FIR $b_n \neq 0 \iff n \geq 0$. In terms of $\mathcal{Z}$-transform[4] the transfer function is given by

$$H(z) = \sum_{n=-\infty}^{+\infty} h[n] z^{-n}$$

For IIR filters, as the adjective *infinite* suggests, $h(t)$ has a not compact support. Compared to FIR, this kind of filters has a more complex expression, involving retroaction, i.e., effect of previous outputs on the current one. The associated mathematical model in a discrete asset satisfies the equation

$$\sum_{j=0}^{Q} a_j f_O[n-j] = \sum_{i=0}^{P} b_i f_I[n-i]$$

with P and Q parameters determining the length of the feedback chain, $a_j, b_i \in \mathbb{R}$, f_I and f_O respectively the functions to the input and to the output of the filter. The associate transfer function in the $\mathcal{Z}$-transform domain

$$H(z) := \frac{Y(z)}{X(z)} = \frac{\sum_{i=0}^{P} b_i}{\sum_{j=0}^{Q} a_j} \, ,$$

being the transfer function $H(z)$ defined as the ratio between the filter at the output $Y(z)$ and the filter at the input $X(z)$.

1.5 Interpolation and Quasi-Interpolation Operators

The sampling theory, thanks to its theorems, explains how to reconstruct a continue (in the sense of analog) signal in its original form, starting from the knowledge of a number of samples. The classical WKS sampling theorem formulation is the only one that guarantees, in line of principles, an exact reconstruction of the original waveform. To behave correctly, the sampling frequency, i.e., the number of samples measured in the time unit, must satisfy the so called Nyquist condition [93, 94]

$$\nu_s \geq 2\nu_{max}$$

where ν_s is the sampling frequency and ν_{max} the band of the signal to be reconstructed.

This condition is necessary to avoid the aliasing phenomenon, i.e., the overlapping of spectral tails.

In practice, especially in case of image processing and visualization, resizing the original signal, constituted by measured samples, is a common procedure. Topologically, a digital image can be schematized as a lattice in $\mathbb{R}^2$, each node of the lattice corresponding to a measured value (see Fig. 1.6). Theoretically, each lattice node has no geometrical size but practically they are associated with a pixel (picture element) of a visualization system (e.g., the screen of a computer): the pixel has a not negligible geometrical size, corresponding to the size of the associated element of the electronic device (e.g., led or LCD). Between each point of the lattice there are topological lacks where the values of the

[4] The bilateral $\mathcal{Z}$ transform of a discrete time signal $x[n]$ is defined as $\mathcal{Z}(x[n]) := \sum_{n=-\infty}^{+\infty} x[n] z^{-n}$, with $n \in \mathbb{Z}$ and $z \in \mathbb{C}$, given all the needed hypothesis for the series convergence [96].

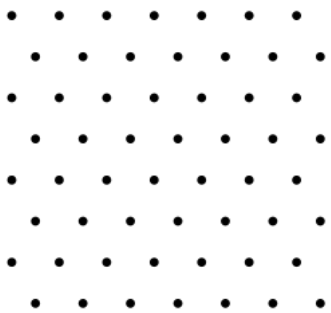

Figure 1.6. A lattice in Euclidean plane. Providing the missing points between the given nodes (whose values derive from a measurement process) is the goal of interpolation and quasi interpolation methods. Strictly speaking, these methods can be seen as particular case of the super-resolution problem [114].

image function has not been measured. The goal of interpolation and quasi-interpolation methods is to forecast the most realistic value for each of these missing points. Elaborations like zooming in and out, and in general whatever affine transformation, need the introduction of such points not directly deriving from the measuring process. In literature, many reconstruction techniques have been introduced to reach this aim.

The simplest way to reconstruct unidimensional signals magnified (e.g., by a factor 2) is to calculate the mean value between two consecutive samples, using the values originally measured. This procedure is called linear interpolation: it is linear because the new reconstructed point stands on the segment linearly connecting 2 consecutive points; it is interpolating because the points used for the calculation of the new values are in the set of samples.

Linear interpolation for one dimensional signals results in substituting the sinc$(\cdot)$ function, used in the classical WKS sampling theorem, with a triangular kernel function. In the frequency domain this is equivalent to the application of a not performing low pass filter, far in shape and characteristics from the ideal filter, causing the aliasing of data with a not complete and correct attenuation of the high frequency components [86].

Similar to the linear, the cubic interpolation is achieved approximating the sinc$(\cdot)$ function with piecewise cubic polynomials. The corresponding kernel is expressed by:

$$\varphi(x) = \begin{cases} A_1|x|^3 + B_1|x|^2 + C_1|x| + D_1, & 0 < |x| < 1 \\ A_2|x|^3 + B_2|x|^2 + C_2|x| + D_2, & 1 < |x| < 2 \\ 0 & 2 < |x| \end{cases}$$

where suitable boundary conditions are needed to calculate the parameters A, B, C, D. See, e.g. [79, 86], for a complete description and more details.

In case of bidimensional signals, linear and cubic interpolation methods are called biliniear and bicubic respectively to enhance their bidimensional character.

To extend the previous considerations, it is useful to generalize that every interpolation method can be formally described by the formulation of the sampling theorem in the generalized form, with the choice of an appropriate kernel φ. The famous B-spline interpolators originate when φ is a piecewise polynomial: linear and cubic interpolators are B-spline using polynomials of order 1 and 3 respectively.

Despite the most intuitive way to reconstruct a function looks to be using values from the set of the given samples, it has been proved that this it is not the most efficient and convenient way

[20, 21]. When a reconstruction method does not employ values from the sampling set, it is called to be quasi interpolant. In the context of this thesis, the most meaningful example of quasi interpolating algorithm is the one provided by the Sampling Kantorovich (SK) operators. In the specific case, the values for the reconstruction are calculated as mean values:

$$w \int_{\frac{(k)}{w}}^{\frac{k+1}{w}} f(u)du$$

obviously not belonging to the measured sampling set. More details about SK operators will be provided in the next chapter.

1.6 Indexes of Similarity

After processing a signal to achieve some results, their estimation is necessary to quantify the goodness of the procedures. Several indices are known in literature for this evaluation. Interpolation and quasi interpolation are, for example, in some sense, reconstruction processes. Application of segmentation methods, i.e., different objects boundary detection, needs indices to evaluate the presence of misclassification and to eventually reduce its source of error.

To evaluate the rate of similarity between two digital images, one of the most popular index in literature is the *Peak Signal to Noise Ratio* ($PSNR$) [68]. It is expressed, for a generic function $f : G \to \mathbb{R}$, $G \subset \mathbb{R}^n$, by the following formula

$$PSNR \;=\; 10 \cdot \log \left(\frac{[\max_{\bar{x} \in \mathbb{R}^n} f(\bar{x})]^2}{MSE} \right),$$

where MSE is the standard *Mean Square Error*, defined as follows

$$MSE \;=\; \frac{\int\limits_G |f(\bar{x}) - f_r(\bar{x})|^2 \, d\bar{x}}{\int\limits_G d\bar{x}},$$

f being the original signal and f_r being its reconstructed version.

The $PSNR$ is extensively used in image analysis and processing to evaluate, for example, the rate of similarity of two images after a watermarking process [91]. In the field of grayscale image reconstruction, where the domain G is discrete, the bidimensional discrete version of the MSE is achieved replacing the integral with the summation symbol, as follows:

$$MSE_d \;=\; \sum_{i=1}^{L} \sum_{j=1}^{M} \frac{|I(i,j) - I_r(i,j)|^2}{L \cdot M},$$

where I is the original image of size $L \cdot M$ and I_r is its reconstructed version.

In case of 8-bits coded graylevel images, the maximum value in the admissible range is equal to 255, hence the $PSNR$ turns to be

$$PSNR_d \;=\; 10 \cdot \log \left(\frac{255^2}{MSE_d} \right).$$

The use of the $\log(\cdot)$ function in the definition of $PSNR$ is justified mostly by engineering reasons:

- $PSNR$ expresses a ratio between energies, traditionally measured in decibel dB (logaritmic scale) in engineering measurement processes;
- the logaritmic scale provides more comparable numerical values respect to the linear scale (e.g., as in the case of a signal varying of some order of magnitude).

Thanks to its general definition, the $PSNR$ can be employed for several families of signals.

On the other hand, more specific indexes are focused on binary sets. For example, the Dice coincidence index (DCI) [59], specific for the similarity of two binary sets of points, A and B, is defined as

$$DCI \ := \ \frac{2 \cdot \#(A \wedge B)}{\#A \ + \ \#B} \, , \tag{1.7}$$

where $\#A$ is the number of elements in A, $\#B$ is the number of elements in B, and $\#(A \wedge B)$ is the number of common elements in A and B (logic AND).

With the same meaning of symbols, the Tanimoto index (TI) [61], measuring the ratio between the correctly classified elements and the total number of them, is defined as

$$TI \ := \ \frac{\#(A \wedge B)}{\#A \ + \ \#B \ - \ \#(A \wedge B)} \, . \tag{1.8}$$

Moreover, it is possible to define the misclassification error as, in some sense, complementary to TI, considering the number of misclassified elements in A and B

$$E_m \ := \ \frac{\#m}{\#A \ + \ \#B \ - \ \#(A \wedge B)} \, , \tag{1.9}$$

where $\#m$ is the number of misclassified elements.

E_m counts the total number of elements wrongly classified, both false positive and false negative, and compare them to the whole size of the sets.

An additional normalized evaluation of the difference between two binary sets can be also introduced as

$$E_n \ := \ \frac{\#m}{\#ROI},$$

where, $\#m$ has the same meaning as before and $\#ROI$ is the total number of elements in the considered Region Of Interest, equal to the size of the sets (e.g., an image can be seen as a set of points to be classified). In this way E_n turns out to be, in some way, a normalized error.

Another important factor to quantify differences between binary sets stands in their shapes: for this reason the circularity shape-factor [95], defined as

$$Circ \ := \ \sqrt{\frac{4\pi Area}{P^2}}, \tag{1.10}$$

can be used to compare the difference between the shape of a perfect circle and the boundary of a whatever set. In (1.10), $Area$ and P are respectively the area and the perimeter of the objects under analysis. Then, the shape error between A and B can be defined as

$$E_s \ := \ \left| 1 \ - \ \frac{Circ_{\,A}}{Circ_{\,B}} \right|,$$

where $Circ_{\,A}$ is the circularity of A and $Circ_{\,B}$ is the circularity of B. Without additional hypothesis E_s can assume values bigger than 1.

Moreover, Hausdorff distance H_{dc} between the border of two sets, together with the Hausdorff distance H_d between the full sets (i.e., with the inner part of the set included in the measurement), can be calculated to estimate the shape similarity. More precisely, the Hausdorff distance measures the mismatch level between two sets of points, A and B, considering the maximum value of the distance of A from B and viceversa. Let $A = \{a_1, a_2, ..., a_n\}$ and $B = \{b_1, b_2, ..., b_m\}$ be two non-empty discrete subsets of a metric space (M, d); the Hausdorff distance H_d is defined as

$$H_d := \max\{d(A,B), d(B,A)\} ,$$

where

$$d(A,B) := \max_{a_i} \min_{b_j} |a_i - b_j|, \qquad d(B,A) := \max_{b_j} \min_{a_i} |a_i - b_j| ,$$

with $i \in [1,n], j \in [1,m]$.

During a measurement process, it could be of some importance to evaluate if an algorithm systematically tends to the over-estimation or under-estimation (bias error), e.g., in a segmentation process. To consider this behavior, the following parameter can be borrowed from [127]

$$B_{pn} := \frac{\#\mathrm{fp} - \#\mathrm{fn}}{\#\mathrm{tp}},$$

where fp is the set of false positive, fn is the set of false negative and tp is the set of the true positive. If $B_{pn} > 0$ the classification procedure tends to overestimate, the other way around if $B_{pn} < 0$.

Another aspect that is important to consider concerns the difference, in terms of extracted area, between two planar sets A and B. A meaningful parameter to quantify the morphological differences between them is

$$\Delta D_c := \|C_A - C_B\|_2 ,$$

where C_A is the centroid of one set and C_B the centroid of the other one, being a generic centroid C_e in a bidimensional discrete set S constituted by N points, defined as

$$C_e := (x_C, y_C), \qquad x_C := \frac{\sum_{i=1}^{N} x_i}{N}, \qquad y_C := \frac{\sum_{i=1}^{N} y_i}{N} .$$

Further, it can be of some utility to estimate the difference between the diameters of A and B

$$\Delta D_a := |D_A - D_B| ,$$

where D_A and D_B are the diameters of the two extracted zones, being a generic diameter D in a convex or non convex set S^μ, defined as

$$D := \sup\left\{\|\underline{p} - \underline{q}\|_2, \quad \text{for every } \underline{p}, \underline{q} \in S^\mu\right\} ,$$

in the cases considered in this work being the considered points belonging only to the boundary of the sets. The difference between the area of A and B is defined as:

$$\Delta A_a := \frac{\#A + \#B - 2 \cdot \#(A \wedge B)}{\#A + \#B} ,$$

having ΔA_a a normalized formulation such that $\Delta A_a \in [0,1]$.

Chapter 2

Multivariate Sampling Kantorovich Operators

The formalization of the first version of the generalized Sampling Theorem states the reconstruction of a function $f \in C(\mathbb{R})$. To relax the assumptions and extend the result of the theorem to a class of functions not necessarily continuous, i.e., belonging to L^p spaces, the Sampling Kantorovich (SK) operators have been introduced as more suitable operators in this setting [15]. The need for the continuity of the function f depends mainly on the pointwise values $f(\frac{k}{w})$ of the samples considered in the formalization of the sampling theorems (in both the WKS or Generalized formulation).

2.1 Definitions

In one dimensional setting, given $\Pi = (t_k)_{k\in\mathbb{Z}}$, a sequence of real numbers such that:

(i) $-\infty < t_k < t_{k+1} < +\infty$;

(ii) $\lim_{k\to\pm\infty} t_k = \pm\infty$;

(iii) there exists $\Delta, \delta > 0$ such that $\delta \leq t_{k+1} - t_k \leq \Delta, \forall k \in \mathbb{Z}$;

the sampling distance Δ_k is defined as $\Delta_k := t_{k+1} - t_k$.

A function $\chi : \mathbb{R} \to \mathbb{R}$ is a *kernel* for the SK operator if:

(χ_1) $\chi \in L^1(\mathbb{R})$ and it is bounded in a neighborhood of the origin;

(χ_2) $\sum_{k\in\mathbb{Z}} \chi(u - t_k) = 1$, for each $u \in \mathbb{R}$;

(χ_3) there exists $\beta > 0$, such that $m_{\beta,\Pi}(\chi) := \sup_{u\in\mathbb{R}} \sum_{k\in\mathbb{Z}} |\chi(u - t_k)||u - t_k|^\beta < +\infty$,
i.e., the discrete absolute moments of order β are finite.

Definition 2.1.1. *Given a kernel χ, the family of operators $(K_w f)_{w>0}$,*

$$(K_w f)(x) := \sum_{t_k\in\mathbb{Z}} \chi(wx - t_k) \left[\frac{w}{\Delta_k} \int_{\frac{t_k}{w}}^{\frac{t_{k+1}}{w}} f(u)\, du \right]$$

for $x \in \mathbb{R}$, $w > 0$ and $f : \mathbb{R} \to \mathbb{R}$ a locally integrable function such that the previous series converges for each $x \in \mathbb{R}$, defines the sampling Kantorovich operators.

In general, it is possible to define the same family of operators in a multidimensional setting. In this case, we consider $\Pi = (t_{\underline{k}})_{\underline{k} \in \mathbb{Z}^n}$, and the kernel $\chi : \mathbb{R}^n \to \mathbb{R}$, with suitable properties below reformulated.

Definition 2.1.2. *Given a kernel $\chi : \mathbb{R}^n \to \mathbb{R}$, the family of multidimensional operators $(K_w f)_{w>0}$, is defined as [49]*

$$(K_w f)(\underline{x}) \ := \ \sum_{\underline{k} \in \mathbb{Z}^n} \chi(w\underline{x} - t_{\underline{k}}) \left[\frac{w^n}{A_{\underline{k}}} \int_{R^w_{\underline{k}}} f(\underline{u}) \, d\underline{u} \right], \qquad \underline{x} \in \mathbb{R}^n, \quad w > 0,$$

where $f : \mathbb{R}^n \to \mathbb{R}$ is a locally integrable function such that the above series is convergent for every $\underline{x} \in \mathbb{R}^n$,

$$R^w_{\underline{k}} \ := \ \left[\frac{t_{k_1}}{w}, \frac{t_{k_1+1}}{w} \right] \times \left[\frac{t_{k_2}}{w}, \frac{t_{k_2+1}}{w} \right] \times ... \times \left[\frac{t_{k_n}}{w}, \frac{t_{k_n+1}}{w} \right],$$

and $A_{\underline{k}} := \Delta_{k_1} \cdots \Delta_{k_n}$.

Moreover, it is possible to generalize the previous definition in the case of not equi-scaled multidimensional sequences, such that w is not constant in each direction of the space.

The multidimensional function $\chi : \mathbb{R}^n \to \mathbb{R}$, used in definition 2.1.2, is a *kernel* if the following assumptions are satisfied:

(χ'_1) χ belongs to $L^1(\mathbb{R}^n)$, and it is bounded in a neighborhood containing the origin of $\mathbb{R}^n$;

(χ'_2) for every $\underline{x} \in \mathbb{R}^n$, there holds:

$$\sum_{\underline{k} \in \mathbb{Z}^n} \chi(\underline{x} - t_{\underline{k}}) = 1;$$

(χ'_3) for some $\beta > 0$, the discrete absolute moment of order β of χ is finite, i.e.,

$$m_\beta(\chi) \ := \ \sup_{\underline{u} \in \mathbb{R}} \sum_{\underline{k} \in \mathbb{Z}^n} \left| \chi(\underline{u} - t_{\underline{k}}) \right| \cdot \| \underline{u} - t_{\underline{k}} \|_2^\beta \ < \ +\infty,$$

where $\| \cdot \|_2$ denotes the usual Euclidean norm of $\mathbb{R}^n$.

A brief list of some well known and important class of kernels which satisfy the above assumptions, and that can be used in order to implement (2.1.2), is given.

It has to be noted that the classical formulation of the sampling theorem uses the sinc$(\cdot)$ function as a kernel, whose integral on the real axis is equal to one but does not belong to $L^1(\mathbb{R})$. An example of a one dimensional kernel, is the one dimensional central B-spline of order $N \in \mathbb{N}$. It is defined as (see, e.g., [118, 119, 2])

$$M_N(x) \ := \ \frac{1}{(N-1)!} \sum_{i=0}^{N} (-1)^i \binom{N}{i} \left(\frac{N}{2} + x - i \right)_+^{N-1}, \qquad x \in \mathbb{R}, \tag{2.1}$$

where $(x)_+ = max\{x, 0\}$.

In general, checking the validity of the assumptions (χ'_γ), $\gamma = 1, 2, 3$ for a multivariate kernel is not immediate. A possibility to achieve suitable kernels in multivariate setting lies in considering the product of one dimensional versions of the same kernel type, as stated by the following lemma[1].

[1] For simplicity of notation, in what follows, only the case $t_{\underline{k}} = \underline{k} \in \mathbb{Z}^n$ of an uniform sampling scheme is going to be formally considered.

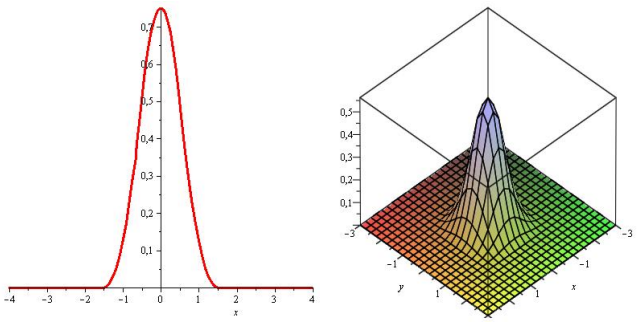

Figure 2.1. Plots of one dimensional and bidimensional central B-spline $M_3(x)$ (left) and $\mathcal{M}_3^2(\underline{x})$ (right), respectively.

Lemma 2.1.3. *Let $\chi_i : \mathbb{R} \to \mathbb{R}$, $i = 1, \ldots, n$, be unidimensional kernels. Then*

$$\chi(\underline{x}) := \prod_{i=1}^{n} \chi_i(x_i), \qquad \underline{x} \in \mathbb{R}^n,$$

is a multidimensional kernel satisfying the kernel conditions (χ'_γ), $\gamma = 1, 2, 3$.

Lemma 2.1.3 (see [27]) provides a useful procedure to construct multivariate kernels of product type starting from univariate ones.

Given the previous result, it is immediate to introduce the corresponding multivariate version of the central B-spline of order N, as

$$\mathcal{M}_N^n(\underline{x}) := \prod_{i=1}^{n} M_N(x_i), \qquad \underline{x} = (x_1, ..., x_n) \in \mathbb{R}^n. \tag{2.2}$$

Central B-spline functions are examples of compact support kernels (see figure 2.1). Another important kernel family, constructed using the sinc$(\cdot)$ function, is given by the so-called Jackson type kernels of order N (see, e.g., [29, 17, 73, 41, 42]), defined in the univariate case by

$$J_N(x) := c_N \operatorname{sinc}^{2N}\left(\frac{x}{2N\pi\alpha}\right), \qquad x \in \mathbb{R}, \tag{2.3}$$

with $N \in \mathbb{N}$, $\alpha \geq 1$, and c_N a non-zero normalization coefficient, given by

$$c_N := \left[\int_{\mathbb{R}} \operatorname{sinc}^{2N}\left(\frac{u}{2N\pi\alpha}\right) du\right]^{-1}.$$

Jackson type kernels have not compact support. An example of Jackson type kernel is shown in figure 2.2. In a similar way, as in the case of central B-splines, multivariate Jackson type kernels of order N are defined by the product of n univariate kernels as

$$\mathcal{J}_N^n(\underline{x}) := \prod_{i=1}^{n} J_N(x_i), \qquad \underline{x} = (x_1, ..., x_n) \in \mathbb{R}^n. \tag{2.4}$$

Another not compact support example is given by the multivariate Fejér kernels, defined as

$$\mathcal{F}^n(\underline{x}) = \prod_{i=1}^{n} F(x_i), \qquad \underline{x} = (x_1, ..., x_n) \in \mathbb{R}^n, \tag{2.5}$$

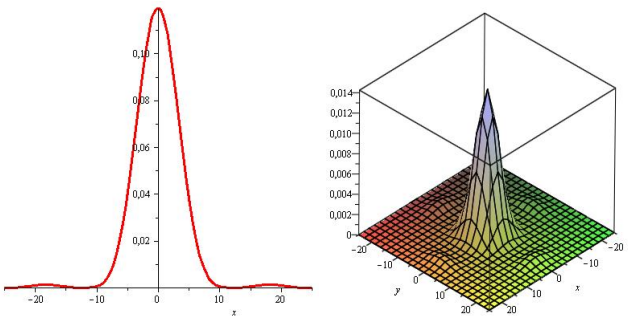

Figure 2.2. Plots of one dimensional and bidimensional Jackson type kernels $J_2(x)$ (left) and $\mathcal{J}_2^2(\underline{x})$ (right), with $\alpha = 1$.

where $F(x)$, $x \in \mathbb{R}$, denotes the univariate Fejér kernel, defined by

$$F(x) \ := \ \frac{1}{2}\,\mathrm{sinc}^2\left(\frac{x}{2}\right), \qquad x \in \mathbb{R}, \tag{2.6}$$

with the $\mathrm{sinc}(\cdot)$ function previously given.

Another important class of (radial) kernels is represented by the so called Bochner-Riesz kernels of order $N > 0$, expressed by

$$R_N(\underline{x}) \ := \ \frac{2^N}{\sqrt{2\pi}}\,\Gamma(N+1)\,||\underline{x}||_2^{-N-1/2}\,J_{N+1/2}(||\underline{x}||_2), \qquad \underline{x} \in \mathbb{R}^n, \tag{2.7}$$

where J_λ is the Bessel function of order λ [44], and Γ is the usual Euler gamma function.

Other results of approximation in both univariate and multivariate cases by means of sampling type operators, can be found in [29, 27, 17, 50, 51, 3, 53].

To the light of the given definitions, the SK operators K_w can be reviewed as an L^1-version of the generalized sampling operators, introduced by P.L. Butzer and his school in 1980s, and widely studied in last thirty years, see, e.g., [30, 27, 82, 81]: being formalized by an integral calculated in the neighborhood of the sampled point, the SK operators, as well as in the generalized sampling formulation, are a kind of quasi-interpolation operators, see, e.g., [38, 120, 111, 108].

2.2 Convergence Results

It is well known that K_w, $w > 0$, defined in (2.1.2), are approximation operators, able to reconstruct pointwise, continuous and bounded functions, and uniformly, functions which are uniformly continuous and bounded, as $w \to +\infty$, [15, 122, 97]. Moreover, the operators K_w revealed to be suitable also to reconstruct not necessarily continuous signals, in the L^p-sense.

The following theorem states the convergence properties of the above operators in (2.1.2) when one deals with continuous signals (see, e.g., [49]).

Theorem 9. *Let χ be a kernel for the operators defined in 2.1.1 and let $f : \mathbb{R}^n \to \mathbb{R}$ be a continuous and bounded function. Then, for every $\underline{x} \in \mathbb{R}^n$,*

$$\lim_{w \to +\infty} (K_w f)(\underline{x}) \ = \ f(\underline{x}).$$

Moreover, if $f \in C(\mathbb{R}^n)$, then

$$\lim_{w \to +\infty} \|K_w f - f\|_\infty = 0,$$

where $\|\cdot\|_\infty$ denotes the usual sup-norm.

Moreover, the following L^p-convergence theorem can be obtained as a particular case of a modular convergence theorem in Orlicz spaces, in order to reconstruct not necessarily continuous signals by means of SK operators, (see e.g., [49] and, for Orlicz spaces, see e.g., [92, 17]).

Theorem 10. *Let χ be a kernel for the operators defined in 2.1.1. For every $f \in L^p(\mathbb{R}^n)$, $1 \leq p < +\infty$, there holds*

$$\lim_{w \to +\infty} \|K_w f - f\|_p = 0,$$

where $\|\cdot\|_p$ denotes the usual L^p-norm.

2.3 Implementation of Sampling Kantorovich algorithm and numerical results [2]

Given the previous convergence theorems it is possible to apply the SK algorithm to image reconstruction, using methods similar to those ones described in Section 1.4.

Thanks to its integral definition, being each sample of the WKS sampling theorem replaced by a mean of the function in the interval $[k, k+1]$, the SK operator puts in evidence a model particularly suitable to describe the effective real-world sampling process.

Every real-world system able to perform a measurement needs a certain time to complete the acquisition. This time is connected, on one hand to the inertia of the instrument, on the other hand to the finite duration D of the measurement itself ($D > 0$). Due to both these reasons, the resulting sample is a mean value of the effective signal. The SK operators provides a mathematical model capable to realistically describe this acquisition procedure. Moreover, during a time periodic sampling process, a "clock" scanning the signal is needed to respect the hypothesis of equi-spaced (uniform) sampling: even using sophisticated techniques, this goal is not strictly achievable. Due to this, real-world samples are not mathematically equi-spaced: this is referred in Signal Theory as the jitter error. Providing a local average around the sample, SK algorithm constructively takes into account the jitter error.

In Table 2.1 the pseudo code of the SK algorithm is shown. The user inputs the values for the scaling factor R, the parameter w and the type of kernel χ. Starting from the original image I, having resolution of $n \times m$ pixels, the code calculates the bivariate kernel χ chosen for the reconstruction, according with the value of w. The final image will have the size of $(n \cdot R) \times (m \cdot R)$. The algorithm proceeds computing the mean values (samples), represented by the integral in the theoretical formulation, by means of the Kroenecker matrix product. The core of the code is the convolution product of χ by the samples (Iteration part in the table), at the end of which the image is saved in lossless format.

The problem of image rescaling has been widely studied in Digital Image Processing (DIP). The main difficulty to overpass when increasing the image size is due to the unknown information between two contiguous points or pixels. Typical methods developed to perform the above task are based on mathematical interpolation (see, e.g., [35, 129] or Chapter 1). For instance, bilinear and bicubic interpolation are among the most common (even if not the best performing) interpolation methods for image rescaling, being in fact B-spline of order two and four respectively (see, e.g.,

[2] Results contained in this section are published in [48].

Objective: Reconstructing and improving the resolution of the original bivariate image I by sampling Kantorovich operators based upon the bivariate kernel χ.

Inputs: Original image I ($n \times m$ pixels resolution), the parameter $w > 0$ and the scaling factor R.

- Choice and definition of the kernel function χ;
- Size of the reconstructed image: $(n \cdot R) \times (m \cdot R)$;
- Computation of matrices of the mean values (samples) of I by means of the Kronecker matrix product.
- Definition of the vectors containing the arguments of χ.

Iteration: Summation over $\underline{k}$ of all non zero terms of the form $\chi(w\underline{x} - \underline{k}) \cdot \left[w^2 \int_{R^w_{\underline{k}}} I(\underline{u})\, d\underline{u}\right]$, for a suitable fixed grid of points $\underline{x}$.

Output: The reconstructed image of resolution $(n \cdot R) \times (m \cdot R)$.

Table 2.1. Pseudo-code of the sampling Kantorovich algorithm for image reconstruction and enhancement.

[100, 34]). They are quite easy to implement and fast to execute. On the other hand, they do not provide optimal results in terms of reconstruction quality, as measured by the $PSNR$ [43].

Recently, to overcome this limit, quasi interpolation methods have been successfully used. From the theoretical point of view, they provide better performances compared to standard interpolation, as proved by suitable estimates (see, e.g., [20]). For instance, quasi[3] Finite Impulse Response (quasi FIR) and quasi Infinite Impulse Response (quasi IIR) have been applied to the rescaling problem. Numerical results confirmed the theoretical previsions, in case of non trivial multiple image rotation (see [43] again).

Concerning quasi interpolation methods, SK algorithm has been introduced in [49].

The implementation of the SK algorithm makes use of suitable kernels which, from the mathe-

[3]The adjective *quasi* here specifies the use of quasi interpolation methods for FIR and IIR filters.

matical point of view, are discrete approximate identities in the sense described in [29], such as the central B-spline, the Jackson type and the Bochner-Riesz kernels [50]. In the case of the implementation of the SK algorithm based upon the Jackson type kernels, some meaningful numerical results have been achieved in the engineering field concerning the study of thermal bridges and the behavior of buildings under seismic actions, by means of thermographic images ([41, 42, 7, 8] or Chapter 3, Section 4).

The main purpose of this paragraph is to evaluate the performance of the SK algorithm in image magnification, in term of $PSNR$ and CPU[4] time, in comparison with the above mentioned interpolation and quasi interpolation methods. The final goal is to obtain an objective map of the performances of the SK algorithm for different kernel types, studying their behavior when varying the parameter w of the operators and the order N of each kernel.

The SK (optimized) implementation is based on a numerical version of the formula before defined in 2.1.2, Chapter 2, Section 2.1.

In figure 2.3, an example of the application of the SK algorithm for reconstruction purposes is shown, employing different kernels. The initial image, denoted by "Starting image" in figure 2.3, has a dimension of 128×128 pixels, and has been obtained, reducing in size, the so called "Target" image (256×256 pixels). If the starting image is resized to the dimension of 256×256 pixels without any interpolation or quasi interpolation algorithms, i.e., by means of a mere pixel duplication, the second image of the first column in figure 2.3 is obtained ("No interpolation" image). On the second column of figure 2.3, there are the results of reconstruction (all of 256×256 pixels) obtained by the application of the SK algorithm with different w and N (i.e., varying the order of the kernel, as defined in Section 2.1). More precisely, figure "A" has been obtained by the bidimensional central B-spline $\mathcal{B}_5^2$ with $w = 5$. The figure "B" has been obtained by the bidimensional Jackson type kernel $\mathcal{J}_{10}^2$ with $w = 40$, and finally, figure "C" has been obtained by the bidimensional Bochner-Riesz kernel $\mathcal{R}_5^2$ with $w = 25$ (given a generic χ_N^n kernel, n is the dimension of the domain of the kernel of the function χ and N is its order). Complete numerical results for different values of w are provided in the tables at the end of this chapter. To perform the measurement of the similarity between the original and the reconstructed images, the standard version of $PSNR$ has been adopted: it gives an objective, not observer-dependent, evaluation of the error after the reconstruction (see, e.g., [43]).

To evaluate the $PSNR$ with Matlab©, the native function *psnr()* has been used. Before performing the calculation, the conversion of the image data from the uint8 Matlab© specific format[5], into the double format is opportune. This casting[6] operation is necessary because, if the *psnr()* function is applied to uint8 data, the result is forced to be zero even if the difference in the MSE_d is lower than zero: this, obviously, brings to erroneous numerical estimations.

As reference for the state of the art, standard bilinear and bicubic methods other than quasi FIR and quasi IIR filters, as defined in [100, 43], have been chosen. According with [20, 21], the expectation is to find better results applying quasi interpolation methods than interpolation ones. The choice of the reference algorithms is motivated by the fact that bilinear and bicubic, which are both interpolation methods, represent very performing algorithms in terms of time consuming and $PSNR$ ([79]), respectively.

On the other side, FIR and IIR are both quasi interpolation methods that appear to be more performing in the $PSNR$ sense, if compared with standard interpolation algorithms (see [43] again).

Technically, it is well known that quasi interpolation methods need the specification of certain

[4]CPU is the English Acronym for Central Processing Unit, i.e., the elaboration unit in computers.

[5]The Matlab© format uint8 specifies the unsigned 8 bit integer. Its range is from 0 to $2^8 - 1$, suitable for 8 bit grayscale image representation but not correct in case of negative values, e.g., when working with reconstruction errors.

[6]In Computer Science the specific cast operator forces one data type to be converted in another.

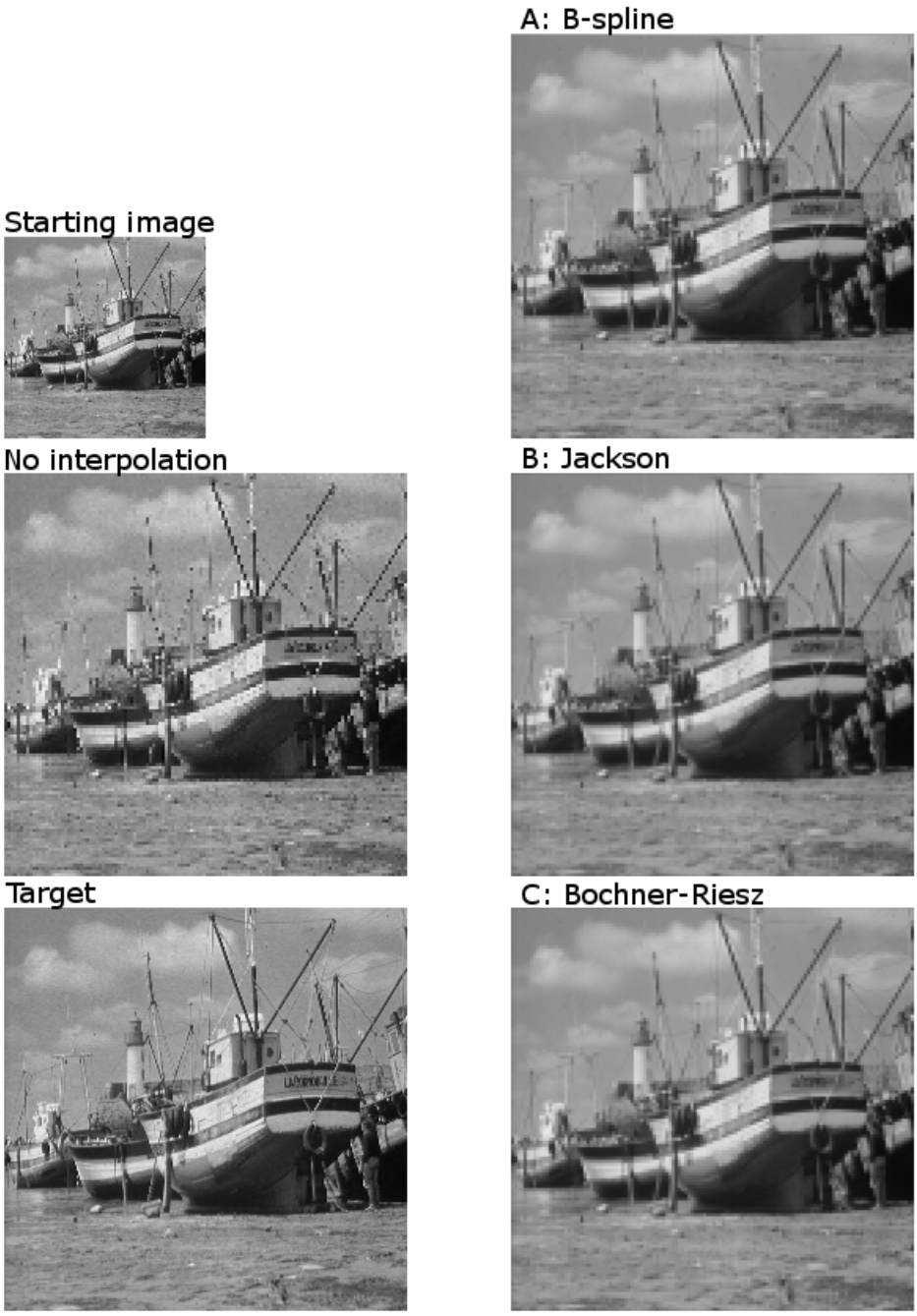

Figure 2.3. In the first column the original "Starting image", derived shrinking the "Target" image of a factor 2 in vertical and horizontal directions, together with a rescaled image without any interpolation (nearest neighborhood) are shown. In the second column, there are some reconstructions of the "Starting image" by the application of the SK algorithm with various kernels. Quantitative evaluations for the results achieved with other methods are available in tables 2.3, 2.4, 2.5, 2.6, 2.7.

boundary conditions. One of the advantages of using SK algorithm is that it can operate without specifying any particular boundary conditions: the pixels outside the border of the image do not provide any additional information and it is not necessary to resort to any speculative methods to assign to them, suitable values.

The general mathematical model describing all the reconstruction methods considered in this work can be formalized by a double convolution

$$I(\underline{x}) \;=\; \sum_{\underline{k}\in\mathbb{Z}^2} c_k\,\varphi(\underline{x}-\underline{k}), \quad (c_k) = (I_k) * (p_k), \tag{2.8}$$

where the coefficients (c_k) are obtained by a discrete filtering (p_k) of (I_k), i.e., of the digitalized original image I_k, and $\varphi(x)$ is a suitable kernel (see, e.g. [109]).

Bilinear method consists of a linear interpolation for functions of two variables: this interpolation method has been implemented in Matlab© using (2.8) with $\varphi = \beta^1$, being β^N a generic central B-spline of order N, and all $p_k = 1$.

Bicubic method consists in the implementation of (2.8) with $\varphi = \beta^3$ and all $p_k = 1$.

Quasi FIR method has been implemented by (2.8) with $\varphi = \beta^1$ and the coefficients (c_k) computed by the matrix convolution between the original image and the filtering matrix

$$A = \begin{bmatrix} -\frac{1}{144} & -\frac{7}{72} & -\frac{1}{144} \\ -\frac{7}{72} & \frac{49}{36} & -\frac{7}{72} \\ -\frac{1}{144} & -\frac{7}{72} & -\frac{1}{144} \end{bmatrix}.$$

The matrix A is generated using the following transfer function $H(z)$ (i.e., the $\mathcal{Z}$-transform of the impulsive response (h_k), $k \in \mathbb{Z}$, of the filter[7], [43])

$$H(z) = -\frac{1}{12}z^{-1} + \frac{7}{6} - \frac{1}{12}z\,.$$

Quasi IIR method has been implemented, according to (2.8), using both $\varphi = \beta^1$ and $\varphi = \beta^3$ and the coefficients (c_k) computed by the product between the original image and a suitable filtering matrix A_I.

The matrix A_I is generated using the transfer function $H(z)$ expressed by

$$H(z) \;=\; Y(z)\,X(z),$$

where $X(z)$ and $Y(z)$ are respectively the $\mathcal{Z}$-transform of the input and the output of the filter, with

$$Y(z) = \left(I - \frac{A}{m}\right)^{-1} - \frac{X(z)}{m}.$$

Here, m is a suitable coefficient determined by $H(z)$.

In case of $\varphi = \beta^1$, the transfer function (in the $\mathcal{Z}$-transform domain) is the following

$$H(z) \;=\; \frac{1}{12}z^{-1} + \frac{5}{6} + \frac{1}{12}z$$

giving $m = \frac{25}{36}$, and the matrix A consisting of Toeplitz matrices itself, in the form

[7] Shortly, the $\mathcal{Z}$-transform of h_k, $k \in \mathbb{Z}$, is defined as $H(z) := \sum_{k\in\mathbb{Z}} h_k z^{-k}$

$$A = \begin{bmatrix} A_1 & A_2 & 0 & 0 & ... & ... & 0 \\ A_2 & A_1 & A_2 & 0 & ... & ... & 0 \\ 0 & A_2 & A_1 & A_2 & 0 & ... & 0 \\ \vdots & \vdots & \vdots & \vdots & \vdots & \vdots & \vdots \\ 0 & ... & ... & ... & 0 & A_2 & A_1 \end{bmatrix}$$

with A_1 and A_2 Toeplitz matrices defined as follows

$$A_1 = -\begin{bmatrix} 0 & \frac{5}{72} & 0 & 0 & ... & 0 \\ \frac{5}{72} & 0 & \frac{5}{72} & ... & ... & 0 \\ 0 & \frac{5}{72} & 0 & ... & ... & 0 \\ \vdots & \vdots & \vdots & \vdots & \vdots & \vdots \\ ... & ... & ... & ... & ... & \frac{5}{72} \\ 0 & ... & ... & 0 & \frac{5}{72} & 0 \end{bmatrix},$$

$$A_2 = -\begin{bmatrix} \frac{5}{72} & \frac{1}{144} & 0 & 0 & ... & ... & 0 \\ \frac{1}{144} & \frac{5}{72} & \frac{1}{144} & ... & ... & ... & 0 \\ 0 & \frac{1}{144} & \frac{5}{72} & \frac{1}{144} & 0 & ... & 0 \\ \vdots & \vdots & \vdots & \vdots & \vdots & \vdots & \vdots \\ ... & ... & ... & ... & ... & ... & \frac{1}{144} \\ 0 & ... & ... & ... & 0 & \frac{1}{144} & \frac{5}{72} \end{bmatrix}.$$

In case of $\varphi = \beta^3$, the transfer function $H(z)$ (in the $\mathcal{Z}$-transform domain) is the following

$$H(z) = -\frac{1}{720}z^{-2} + \frac{31}{180}z^{-1} + \frac{79}{120} + \frac{31}{180}z - \frac{1}{720}z^2,$$

giving $m = c^2$, and the A matrix consisting of Toeplitz matrices itself, of the form

$$A = \begin{bmatrix} A_1 & A_2 & A_3 & 0 & ... & ... & 0 \\ A_2 & A_1 & A_2 & A_3 & ... & ... & 0 \\ A_3 & A_2 & A_1 & A_2 & A_3 & ... & 0 \\ \vdots & \vdots & \vdots & \vdots & \vdots & \vdots & \vdots \\ 0 & ... & ... & .A_3 & A_2 & A_1 & A_2 \\ 0 & ... & ... & ... & A_3 & A_2 & A_1 \end{bmatrix},$$

with A_1, A_2 and A_3 Toeplitz matrices defined as follows

$$A_1 = -\begin{bmatrix} 0 & bc & ac & 0 & ... & 0 \\ bc & 0 & bc & ac & ... & 0 \\ ac & bc & 0 & ... & ... & bc \\ \vdots & \vdots & \vdots & \vdots & \vdots & \vdots \\ 0 & ... & ... & ac & bc & 0 \end{bmatrix},$$

$$A_2 = -\begin{bmatrix} bc & b^2 & ab & 0 & ... & ... & 0 \\ b^2 & bc & b^2 & bc & ... & ... & 0 \\ ab & b^2 & bc & b^2 & 0 & ... & 0 \\ \vdots & \vdots & \vdots & \vdots & \vdots & \vdots & \vdots \\ 0 & ... & ... & ... & ab & b^2 & bc \end{bmatrix},$$

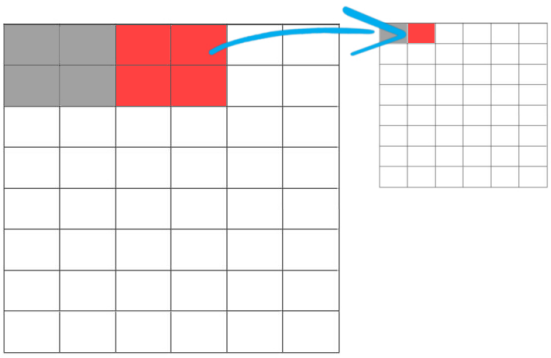

Figure 2.4. The size reduction process associates to a 2×2 pixels area (on the left) a single pixel (on the right) having as value the mean value of the 2×2 cell.

$$A_3 = - \begin{bmatrix} ac & ab & a^2 & 0 & ... & ... & 0 \\ ab & ac & ab & a^2 & ... & ... & 0 \\ a^2 & ab & ac & ab & 0 & ... & 0 \\ ... & ... & ... & ... & ... & ... & 0 \\ 0 & ... & ... & ... & a^2 & ab & ac \end{bmatrix},$$

and $a = \frac{1}{720}, b = \frac{31}{180}, c = \frac{79}{120}$.

For software simulation, a standard set of 5 square images[8] (file names: 'lena', 'baboon', 'cameraman', 'boat', 'barbara'), .png (Portable Network Graphix) file format, have been used, image sizes varying from 16×16 pixels to 64×64 pixels, by steps of powers of 2 $(16, 32, 64, 128)$: in total, 20 images grouped by dimensions.

To generate the above test sets, each 256×256 sized file has been reduced in size by powers of 2, achieving five 128×128 pixels images, five 64×64 pixels images and so on.

The size reduction process proceeded by a mean of the original digital image I_k:

$$I_R(i,j) = \frac{\sum_{u=2i-1}^{2i} \sum_{v=2j-1}^{2j} I_k(u,v)}{4}, \; i,j = 1,2,...,M,$$

with I_k of size $2M \times 2M$, I_R the resized image of size $M \times M$. In this way an "original" reference is available for comparison with the post processing results (figure 2.4 illustrates an example of the resizing procedure). Each I_R of size $M \times M$ is then reconstructed using the SK algorithm [8] and the result is compared, using the PSRN, with the reference of size $2M \times 2M$. In the implementation of the SK algorithm for the reconstruction process, three different families of kernels have been chosen: the central B-spline, the Jackson type and the Bochner-Riesz, varying w and the order N for each kernel (with its own meaning for any case) from $w = 5$ to $w = 50$ (with step size 5) and from $N = 1$ to $N = 10$ (with step size 1). As expected, the SK algorithm with central B-spline, Jackson type and Bochner-Riesz kernels showed results depending on N and w.

For the central B-spline kernels the $PSNR$ exhibits its maximum (that expresses the best achieved performance) for $N \in \{4, 5\}$ and $w = 5$. This trend reproduces for each one of the in-

[8] Using square images does not imply loss of generality respect, e.g., to rectangular shaped ones.

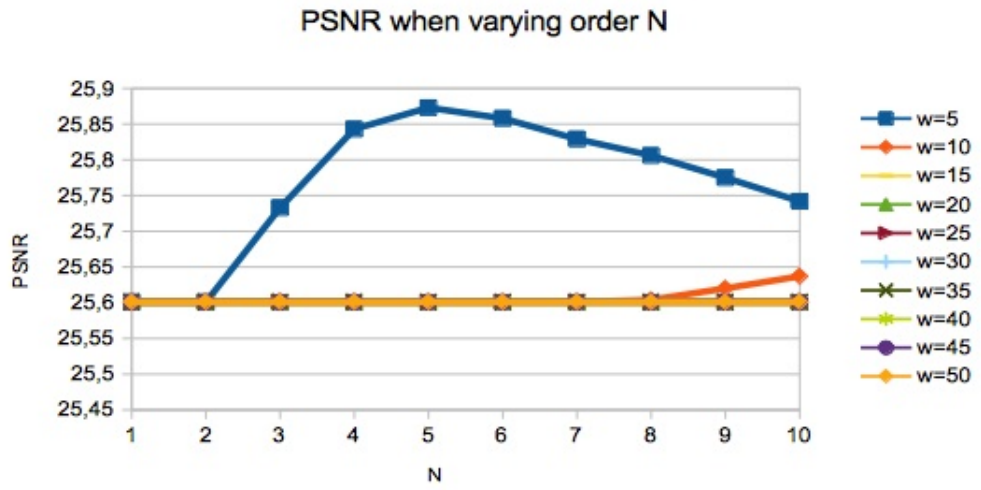

Figure 2.5. Central B-spline trend for various N. Best results are for $w = 5$ and $N = 5$. The graph refers to the reconstruction of 'lena.png', starting size 32×32 pixels, reconstructed size 64×64 pixels. The trend in the graph is qualitatively the same for all the considered images.

vestigated images, independently from the size. For instance, plotting the trend of the $PSNR$ in function of N, for some values of w (see figure 2.5), results in a concave function with some small oscillations, the latter due to numerical computation errors, as w and N increase. Consequently, for stability reasons, the results with $w \geq 15$ is risen to reference. The value $w = 15$ represents a lower bound for the resizing problem, in the sense that the error is almost constant for every N.

Moreover for $w \geq 15$ the $PSNR$ shows no significant improvements when varying w. The choice of lower values for w and N decreases the execution time, common behavior for each kernel.

The results of the application of the SK algorithm with both Jackson type and Bochner-Reisz kernels exhibit a saturation of the $PSNR$ when the order N increases.

Here the word saturation is intended in the engineering sense, meaning that the $PSNR$ has not meaningful variations increasing the parameters on which the SK operator depends.

A noteworthy example of the general trend of $PSNR$ when varying w and N is given in figure 2.6. The Jackson as well as the Bochner-Riesz type kernels exhibit an improvement of the $PSNR$ as w increases. Also in these cases, the value of the $PSNR$ saturates with respect to N.

To achieve a lower bound for w and N for the saturation of the SK algorithm a new *a posteriori* gain speed has been introduced as

$$V_{gain} := \frac{G_{i_{max}}}{|\Delta_t|}, \tag{2.9}$$

where $G_{i_{max}}$ is the maximum gain (will be defined below), in terms of $PSNR$, when varying N, between two subsequent values of w (among those considered), Δ_t is the mean difference of CPU time between two subsequent values of w. The index V_{gain} is positive if and only if $G_{i_{max}} > 0$, according to the fact that the increase of the execution time is acceptable only when the achieved results for a certain w are better than the ones from the previous values of w.

In table 2.2 the evolution of V_{gain}, as w increases, is shown. In case of Jackson type kernel since order $N = 20$, V_{gain} has a value significantly high. For instance, passing from $w = 5$ to $w = 10$, the increase of $PSNR$ is almost 114 times bigger than the increase of the CPU time, while passing

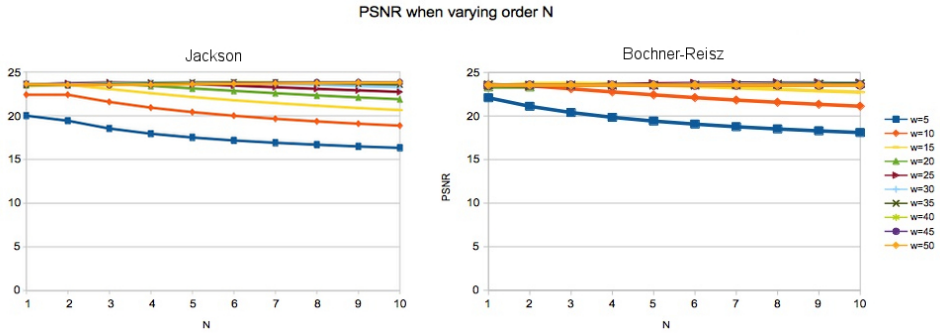

Figure 2.6. Trend of the Jackson (on the left) and Bochner-Reisz (on the right) type kernel reconstructions for various N. Best results are for $w = 5$ and $N = 5$. The graph refers to the reconstruction of 'lena.png', starting size 32×32 pixels, final size 64×64 pixels. The trend in the graph is qualitatively the same for all the considered images.

from $w = 10$ to $w = 15$, the ratio is almost 16, following a decreasing trend with the increment of w. Passing from $w = 25$ to $w = 30$ the CPU time doubles compared to the improvement of the $PSNR$, so that it appears disadvantageous to apply the SK algorithm with such value of w. Finally, some values of V_{gain} appears to be negative but approximatively close to zero: this is the effect of computational numerical errors. Analogous considerations explain the numerical results of table 2.2 relative to the reconstruction by the Bochner-Riesz kernels.

The reference methods (bilinear, bicubic, quasi FIR, quasi IIR with β^1 and β^3) show their best results in terms of $PSNR$ as the image size generally increases (results available in tables 2.3, 2.4, 2.5, 2.6, 2.7). From the results shown in table 2.8, it is evident that the SK algorithm produces better results than the reference methods, even when a small value of w (e.g., $w = 5$) is considered. The central B-spline kernels give the best results in terms of $PSNR$: this behavior stands with low values of w. When w increases the central B-spline kernels show a fast saturation compared to Jackson and Bochner-Riesz type ones (see table 2.9 again, and figure 2.7). As w increases, Jackson type kernels express the best performance.

It is possible to evaluate the SK algorithm performances by the above kernels, for different values of w and N. In table 2.9 and 2.11 respectively, the mean values of $PSNR$ and CPU time have been computed for all $1 \leq N \leq 10$, $N \in \mathbb{N}$, and for each of the reconstructed images, when varying w. Figure 2.7 and 2.9, respectively, shows the $PSNR$ qualitative trends and the CPU time for different kernels. In terms of $PSNR$, central B-spline kernels perform better for low values of w being their $PSNR$ inversely proportional to w, until $w = 15$. On the other hand, for $15 \leq w < 25$, the Bochner-Riesz kernels show better performances than any other ones. Finally, for $w \geq 25$, the best results are achieved by the Jackson type kernels (see figure 2.8).

For what concerns SK algorithm time consumption, implemented as in [7], it depends on the size of the original image being reconstructed, on the used kernel χ and on w.

All the code has been written and executed in Matlab©, version 8.4.0.150421 (R2014b) on a pc running Microsoft Windows©10 Home Version 10.0.

The SK algorithm performs significantly faster[9] respect to the quasi FIR and quasi IIR (see table

[9]To estimate the CPU time with each methods following the same implementative logic, the code has been structured in two main logically different parts: in the first part the kernel convolution matrix is computed, in the second part the convolution between the image and the kernel is calculated. The only exception to this flow is in the

Jackson

$PSNR$	w	Time (s)	V_{gain} ($PSNR$/s)
17.209	5	0.044	—
19.773	10	0.058	114.531
21.059	15	0.093	16.669
21.711	20	0.134	6.166
22.082	25	0.251	1.141
22.242	30	0.352	0.546
22.293	35	0.489	0.124
22.289	40	0.587	-0.013
22.262	45	0.692	-0.087
22.231	50	0.847	-0.070

Bochen-Riesz

$PSNR$	w	Time (s)	V_{gain} ($PSNR$/s)
18.992	5	0.060	—
21.244	10	0.073	77.898
22.018	15	0.121	5.901
21.938	20	0.403	-0.104
22.246	25	0.356	-2.233
22.209	30	0.494	-0.093
22.164	35	0.687	-0.080
19.709	40	1.302	-1.220
22.149	45	1.067	-3.620
22.126	50	1.452	-0.021

Table 2.2. Incremental time for Jackson and Bochner-Riesz type kernels reconstructions performed on square sized images of 16×16 pixels. The reported values are the means of the results for the entire set.

Original size	Rec. size	$PSNR$	Time (s)	Filename
16	32	15,483	0,019	baboon
16	32	14,582	0,019	barbara
16	32	15,774	0,019	boat
16	32	15,036	0,019	cameraman
16	32	16,006	0,023	lena
Mean		15,376	0,020	
Std. Dev.		0,573	0,002	
32	64	17,673	0,050	baboon
32	64	16,684	0,050	barbara
32	64	17,372	0,050	boat
32	64	16,957	0,051	cameraman
32	64	18,383	0,051	lena
Mean		17,414	0,050	
Std. Dev.		0,661	0,001	
64	128	19,426	0,173	baboon
64	128	19,208	0,171	barbara
64	128	19,341	0,170	boat
64	128	18,702	0,172	cameraman
64	128	20,922	0,173	lena
Mean		19,520	0,172	
Std. Dev.		0,833	0,001	
128	256	19,942	0,812	baboon
128	256	21,296	0,772	barbara
128	256	20,934	0,818	boat
128	256	20,704	0,840	cameraman
128	256	23,074	0,652	lena
Mean		21,190	0,779	
Std. Dev.		1,164	0,075	

Table 2.3. Numerical results obtained by bilinear interpolation for different image sizes for each file of the dataset. For any size, at the bottom, the mean $PSNR$, the mean execution time, and the standard deviation are computed.

Original size	Rec. size	$PSNR$	Time (s)	Filename
16	32	16,614	0,018	baboon
16	32	16,321	0,019	barbara
16	32	17,390	0,020	boat
16	32	16,617	0,020	cameraman
16	32	17,584	0,114	lena
Mean		16,905	0,038	
Std. Dev.		0,549	0,042	
32	64	18,870	0,050	baboon
32	64	18,153	0,049	barbara
32	64	18,929	0,049	boat
32	64	18,361	0,049	cameraman
32	64	19,887	0,049	lena
Mean		18,840	0,049	
Std. Dev.		0,672	0,000	
64	128	20,565	0,162	baboon
64	128	20,569	0,163	barbara
64	128	20,683	0,164	boat
64	128	20,112	0,162	cameraman
64	128	22,339	0,166	lena
Mean		20,854	0,163	
Std. Dev.		0,859	0,002	
128	256	21,000	0,650	baboon
128	256	22,465	0,619	barbara
128	256	22,278	0,665	boat
128	256	22,105	0,666	cameraman
128	256	24,486	0,622	lena
Mean		22,467	0,644	
Std. Dev.		1,264	0,023	

Table 2.4. Numerical results obtained by bicubic interpolation for different image sizes for each file of the dataset. For any size, at the bottom, the mean $PSNR$, the mean execution time, and the standard deviation are computed.

Original size	Rec. size	$PSNR$	Time (s)	Filename
16	32	16,319	0,019	baboon
16	32	15,926	0,021	barbara
16	32	17,267	0,020	boat
16	32	16,471	0,023	cameramen
16	32	17,477	0,241	lena
Mean		16,692	0,065	
Std. Dev.		0,656	0,099	
32	64	18,530	0,048	baboon
32	64	17,879	0,049	barbara
32	64	18,698	0,048	boat
32	64	18,228	0,048	cameramen
32	64	19,739	0,054	lena
Mean		18,615	0,049	
Std. Dev.		0,702	0,003	
64	128	20,256	0,170	baboon
64	128	20,354	0,160	barbara
64	128	20,492	0,161	boat
64	128	19,908	0,163	cameramen
64	128	22,178	0,165	lena
Mean		20,638	0,164	
Std. Dev.		0,888	0,004	
128	256	20,709	0,750	baboon
128	256	22,260	0,612	barbara
128	256	22,043	0,662	boat
128	256	21,868	0,769	cameramen
128	256	24,266	0,610	lena
Mean		22,229	0,681	
Std. Dev.		1,287	0,075	

Table 2.5. Numerical results obtained by FIR quasi interpolation for different image sizes for each file of the dataset. For any size, at the bottom, the mean $PSNR$, the mean execution time, and the standard deviation are computed.

Original size	Rec. size	$PSNR$	Time (s)	Filename
16	32	13,615	0,029	baboon
16	32	15,185	0,029	barbara
16	32	14,363	0,028	boat
16	32	14,990	0,026	cameraman
16	32	16,580	0,032	lena
Mean		14,947	0,029	
Std. Dev.		1,100	0,002	
32	64	14,232	0,189	baboon
32	64	17,164	0,161	barbara
32	64	16,836	0,189	boat
32	64	15,755	0,205	cameraman
32	64	18,510	0,163	lena
Mean		16,499	0,181	
Std. Dev.		1,604	0,019	
64	128	14,555	5,437	baboon
64	128	18,511	5,329	barbara
64	128	19,840	5,464	boat
64	128	16,945	5,521	cameraman
64	128	19,600	4,856	lena
Mean		17,890	5,321	
Std. Dev.		2,187	0,269	
128	256	15,629	228,440	baboon
128	256	20,060	226,970	barbara
128	256	17,404	223,610	boat
128	256	17,483	228,850	cameraman
128	256	20,428	233,970	lena
Mean		18,201	228,368	
Std. Dev.		2,011	3,749	

Table 2.6. Numerical results obtained by IIR quasi interpolation with β^1 for different image sizes for each file of the dataset. For any size, at the bottom, the mean $PSNR$, the mean execution time, and the standard deviation are computed.

Original size	Rec. size	$PSNR$	Time (s)	Filename
16	32	14,603	0,029	baboon
16	32	13,816	0,031	barbara
16	32	15,760	0,030	boat
16	32	13,823	0,028	cameraman
16	32	15,601	0,033	lena
Mean		14,721	0,030	
Std. Dev.		0,935	0,002	
32	64	14,328	0,170	baboon
32	64	13,884	0,174	barbara
32	64	15,635	0,186	boat
32	64	14,185	0,169	cameraman
32	64	14,907	0,169	lena
Mean		14,588	0,174	
Std. Dev.		0,693	0,007	
64	128	17,303	5,647	baboon
64	128	15,227	5,446	barbara
64	128	17,435	5,404	boat
64	128	13,883	5,405	cameraman
64	128	14,859	4,931	lena
Mean		15,741	5,367	
Std. Dev.		1,566	0,263	
128	256	15,694	228,850	baboon
128	256	15,913	220,950	barbara
128	256	17,658	215,050	boat
128	256	15,419	229,590	cameraman
128	256	14,670	222,110	lena
Mean		15,871	223,310	
Std. Dev.		1,104	6,028	

Table 2.7. Numerical results obtained by using IIR quasi interpolation with β^3 for different image sizes for each file of the dataset. At the bottom of each size, the mean $PSNR$, the mean execution time, and the standard deviation are computed.

Starting size	Bilinear	Bicubic	quasi FIR	quasi IIR β^1
16	15,376	16,905	16,692	14,947
32	17,414	18,840	18,615	16,499
64	19,520	20,854	20,638	17,890
128	21,190	22,467	22,229	18,201

Starting size	quasi IIR β^3	B-splines	Bochner-Riesz	Jackson
16	14,721	22,096	18,993	17,209
32	14,588	23,743	21,047	19,242
64	15,741	25,569	22,545	21,204
128	15,871	26,815	25,07	24,137

Table 2.8. The mean values of the $PSNR$ computed on all the images of the dataset, for any method considered. The last three columns of the table on the bottom refer to the kernels used for the implementation of the SK algorithm, with $w = 5$. In particular, the mean $PSNR$ is computed considering the above kernels for all the orders $1 \leq N \leq 10$. From the results of these tables, it is evident that SK algorithm gives the best performances, in terms of $PSNR$, compared to other methods. In particular, B-spline kernels gives the highest (best) values of $PSNR$.

w	B-spline	Bochner-Riesz	Jackson
5	24,5555	21,589	20,0779
15	24,2577	24,397	23,81
25	24,4577	24,412	24,733
35	24,4577	24,286	24,802
50	24,4577	24,085	24,645

Table 2.9. The mean values of the $PSNR$ computed on all the images of the dataset with their relative dimension, processed by the SK algorithm, based upon the above kernels. Also here, the mean $PSNR$ is computed considering the above kernels for all the orders $1 \leq N \leq 10$. Note that, the $PSNR$ increases with w.

Starting size	Bilinear	Bicubic	quasi FIR	quasi IIR β^1
16	0,020	0,038	0,065	0,029
32	0,050	0,049	0,049	0,181
64	0,172	0,163	0,164	5,321
128	0,779	0,644	0,681	228,368

Starting size	quasi IIR β^3	B-spline	Bochner-Riesz	Jackson
16	0,030	0,035	0,039	0,044
32	0,174	0,083	0,206	0,172
64	5,367	0,236	0,523	1,254
128	223,310	0,844	4,565	3,447

Table 2.10. The mean values of CPU time (expressed in seconds) computed on all the images of the dataset, for the considered methods. The last three columns of the table on the bottom refer to the kernels used for the implementation of the SK algorithm, with $w = 5$. In particular, the mean CPU time is computed considering the above kernels for all the orders $1 \leq N \leq 10$. From the results of these tables, it is evident that bilinear and bicubic give the best performances. In particular, B-spline kernels show the best performance.

w	B-spline	Bochner-Riesz	Jackson
5	0,2997	6,236	7,204
15	0,4581	38,272	34,326
25	0,6965	132,379	98,632
35	0,9944	241,444	182,441
50	1,6	205,64	351,601

Table 2.11. The mean values of the CPU time (expressed in seconds) on all the images of the dataset with their relative dimension, processed by the SK algorithm, based upon the above kernels. Also here, the mean CPU time is computed considering the above kernels for all the orders $1 \leq N \leq 10$.

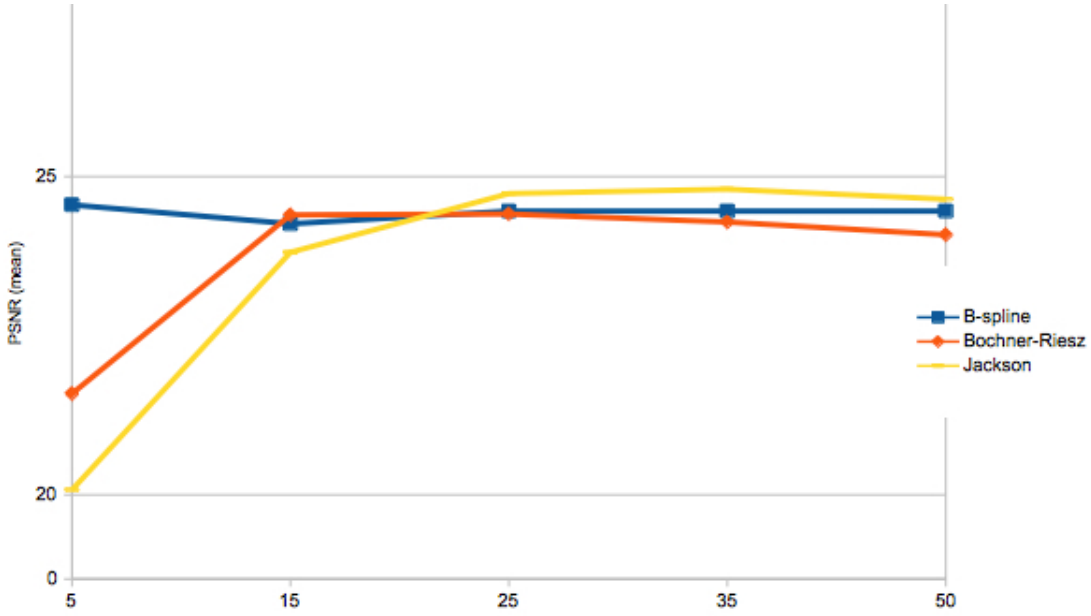

Figure 2.7. Trend of $PSNR$ after the images' reconstruction by the SK algorithm. The saturation process occurs as w increases.

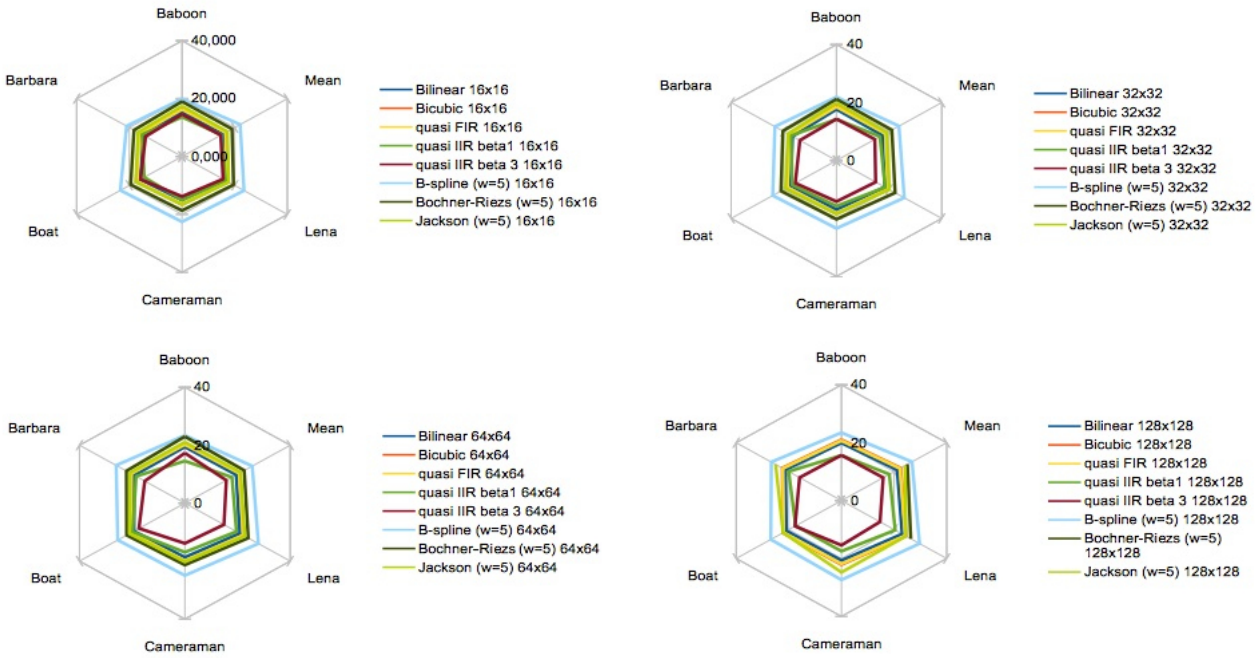

Figure 2.8. Graphical representation of the numerical results listed in table 2.8.

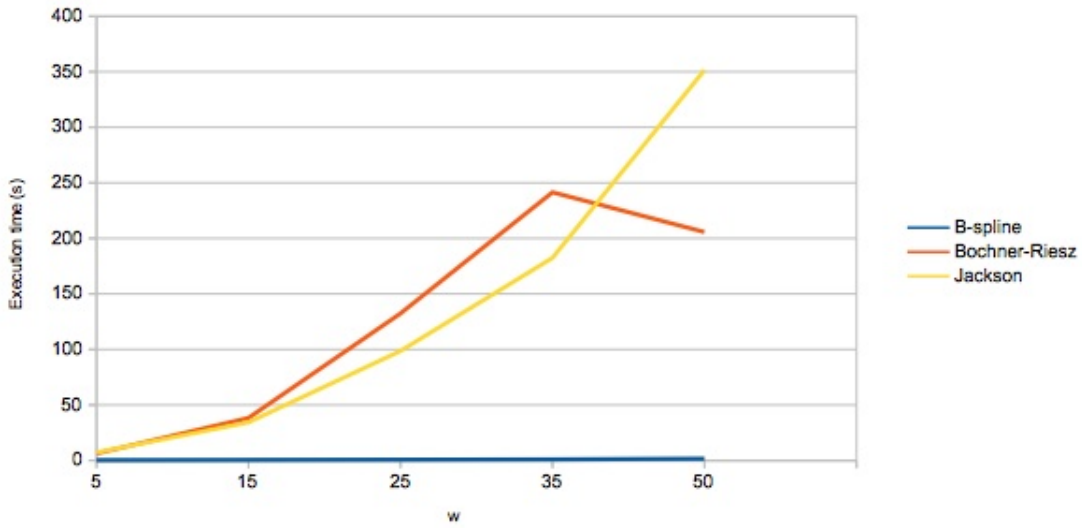

Figure 2.9. Trend of the CPU time after the images' reconstruction by the SK algorithm.

2.10 again). In particular, the CPU time of the quasi IIR depends on the complexity of the algorithm used to invert the matrix $(I - A)$: it is well known that the time for this calculation increases with the size of the matrix A that is proportional to the size of the image to reconstruct (as happens, e.g., in Cholesky factorization [69] and other well known methods). In terms of CPU time the best performances of the SK algorithm are achieved in case of central B-spline kernels, that result to be almost constant when varying w, while in case of both Jackson and Bochner-Riesz kernels, the CPU time increases with an exponential behavior with respect to w (see figure 2.9).

In conclusion, experimental results have shown better performances of SK algorithm in terms of $PSNR$ and CPU time than the other considered reconstruction methods. Summarizing what previously discussed, for values of $w \leq 15$, central B-splines provide the best results; for $15 < w < 25$, the Bochner-Riesz kernels is the most performing; if $w \geq 25$, the Jackson type kernels are the best ones. These results suggest how to proceed in the choice of the kernel and w before the application of SK algorithm in concrete cases, such those studied in [7, 8, 47] (see also Chapter 3).

The experimental trends achieved for each used kernel show the typical saturation behavior of the approximation processes with respect to $w > 0$. The numerical results confirm that the proposed algorithm is suitable for image processing and reconstruction.

quasi FIR implementation that uses the custom Matlab© provided function conv2(). The output from the IIR filter has not been calculated in the $\mathcal{Z}$-transform domain, which would result in a faster implementation. This because similar methods are not available yet for SK operators.

Chapter 3

Application of Sampling Kantorovich Operators to problems arising from medical pathologies

Thanks to the proved theoretical aspects, multivariate SK operators are particularly suitable to be applied to practical problems, especially those needing for the refinement of low resolution data or for noise reduction. With this aim, the mathematical theory has been translated into a computer science executable algorithm. The initial software version, characterized by long execution times, has been optimized until to reach an acceptable reduction of the computational cost, for some orders of magnitude.

Given the limits imposed by the WKS sampling theorem together with the Nyquist criterium, and without the integration of some other sources of information, the impossibility to implement super resolution techniques using only the SK algorithm clearly appears. On the other hand, the multivariate SK theory effectively models the real functioning of sample and hold circuits, describing what really happens in the sampling process of real signals. In what follows the theoretical results have been applied and verified on partially elaborated data (e.g., CT images after the reconstruction from native Hounsfield absorption values), after a pre-elaboration process operated by the measurements devices (see Figure 3.1). Exploiting the SK model characteristics, future applications of such methodology could interest signals at early stages of elaboration (e.g., immediately downstream of the measuring sensors).

3.1 Detection of Aortic Aneurysms [1]

In this section a new algorithm, specifically developed for the segmentation of the pervious lumen of the aorta artery in CT (Computed Tomography) images without contrast medium, is introduced. In the diagnosis of vascular pathologies, such as stenosis of main vessels or aneurysms, CT images play a central role (see, e.g., [58]). In particular, in order to diagnose aneurysm of the aorta artery (see, e.g., [110]) it is necessary to identify the pervious lumen of the vessel inside the artery, i.e., the zone in which the blood flows, and to quantify the rate of the possible occlusion. In CT images, to distinguish the contours of the pervious lumen from the rest of the vessel is generally

[1] Results contained in this section are published in [39, 40, 47].

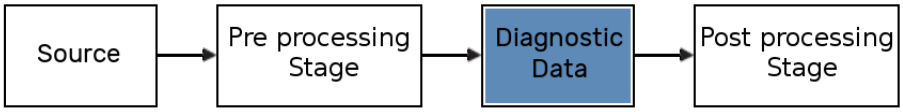

Figure 3.1. A scheme illustrating the signal acquisition and elaboration. After the measurement process a pre-elaboration stage transforms the native raw data into an usable, diagnosable version. Post processing algorithms focus on improvement of signal quality or evaluation of diagnostic parameters. Currently, multivariate SK algorithm operates at the diagnostic data stage.

not possible. To solve the above problem, the vascular surgeons resort to the introduction, in the body of the patient, of a contrast medium, which changes the blood radio opacity with respect to the neighborhood zones, making the pervious section recognizable with respect to the adjacent anatomical structures. However, for patients with severe kidney diseases or allergic problems, the introduction of contrast medium is very inconvenient. For this reason, the availability of techniques for the automatic segmentation of the pervious lumen of the vessels in CT images without contrast medium becomes crucial, the CT being considered the gold standard diagnostic procedure in presence of aortic aneurysms. Actually, due to the similarity of the gray levels in the different zones to segment, this process represents a challenging task in research. The novel approach of the proposed procedure mainly resides in enhancing the resolution of the image by the SK operators. After the application of suitable DIP techniques, the pervious zone of the artery can be distinguished from the occluded one. Numerical tests have been performed using 233 CT images, grouped in 5 sequences, for each one suitable numerical errors being computed or introduced ex novo to objectively evaluate the performance of the new proposed method. Each scan has been acquired by a Philips spiral Tomograph, model Billiance 16, 120 kVp (see Table 3.2 for more details). Corresponding CT scans with contrast medium have been recorded as reference. The number of sequences considered is comparable, if not larger in any case, with the number of sequences used in other valuable works in literature, e.g., [112, 57, 127]. The proposed procedure is completely automatic in all its parts after the initial Region Of Interest (ROI) selection. The main advantages of this approach relies in the potential possibility of performing diagnosis of vascular pathologies even in case of patients with severe kidney diseases or allergic problems, for which contrast medium can not be used.

Currently, a software procedure able to segment the pervious and the occluded zones exploiting standard CT images (i.e., without contrast medium), has not been developed yet.

Starting from standard CT images, a square ROI of size $n \times n$, depicting the aorta artery, is selected and processed using the SK algorithm. The ROI selection is operated, along the axial plane, in a way that the entire CT scan of the portion where the aorta shows the atheroma, is included in the square boundaries of the selection.

Naturally, to avoid this manual selection and reduce the operational time, it is possible to think to adopt one of the numerous automatic algorithms proposed in literature for the segmentation of the aorta artery (see, e.g., [80, 127, 85]). After the application of the SK operator to the ROI, the algorithm proceeds with the analysis of a "circular" area inscribed in it. The selected zone is processed with a wavelet filter, from which the image of the residual low frequency component is extracted. Then, a suitable mask image is used in order to remove the possible effects of spurious structures, such as plaques of calcium or measurement artifacts, and normalization and equalization

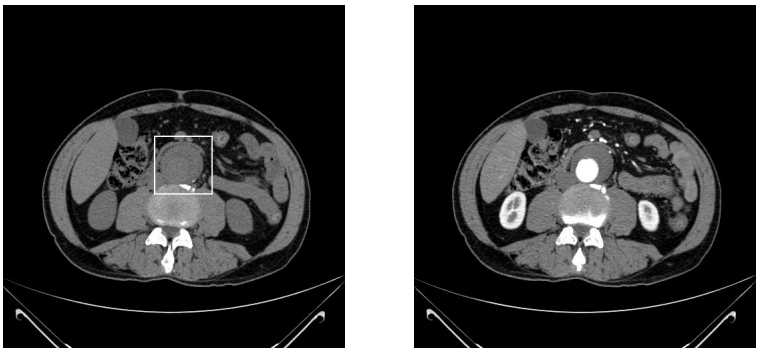

Figure 3.2. On the left: CT image without contrast medium. In the square is depicted the aorta artery. On the right: CT image with contrast medium, corresponding to the CT on the left (reference).

procedures are applied. Finally, the estimated pervious area in the lumen of the artery, is extracted by a certain adaptive thresholding.

In order to analyze the performance of the proposed procedure, some definitions of well known numerical errors are computed using the corresponding contrast medium images as reference. In particular, standard Dice coincidence [59] and the Jaccard/Tanimoto [74, 61] indexes are calculated, together with the new *misclassification error*. The well known Hausdorff distance and a *shape error* are used to quantify the difference in the shapes of the reference CM, extracted from the contrast medium CT, and C_F, resulting by the SK algorithm. The B_{pn} [127] bias term is computed to consider the direction of bias in the extraction procedure; geometric measurements like centroid distance ΔD_c, aortic area difference ΔA_a, aortic diameter difference ΔD_a, using the generalized definition of diameter for convex and not convex shapes [54], are calculated for both C_F and CM. The results show that the procedure is able to localize the position of the pervious lumen inside the artery with a good accuracy in matching the contrast medium reference.

The role of the bidimensional SK operators is fundamental in order to process such kind of digital data (e.g., images) and reduce the errors in the segmentation procedure (see, e.g., [75, 51, 7, 8]).

The above method, as well as the evaluation of the segmentation errors, have been implemented in Matlab© and Python vers. 2.6.7..

Examples of practical reconstruction and enhancement of some biomedical images that leads to interesting arguments from the diagnostic point of view, can be found in [89].

In Figure 3.2 (left) a CT image without contrast medium depicting the aorta artery is shown. The images have been achieved converting the CT scans, natively acquired in Hounsfield scale, from a 12 bits DICOM format to 8 bits graylevels files in the lossless .png (Portable Network Graphics) format. The set of resulting images has been achieved after the application of a standard windowing procedure, selected by medical specialists, according to their diagnostic needs. In general, in order to investigate some pathology of the vascular apparatus, such as aneurysms or stenosis, CT images (see, e.g., [1]) as those showed in Figure 3.2 (left) are not useful. For instance, in the above image the aorta artery is delimited by a square ROI of 240×240 pixels, and the lumen is not distinguishable from the entire vessel. Indeed, to perform a correct diagnosis, images with contrast medium, like the one shown in Figure 3.2 on the right, are necessary. The white area in the aorta of Figure 3.2 (right) represents the pervious lumen of the vessel highlighted by the contrast medium.

In what follows, images like the one of Figure 4.4, i.e., representing only the ROI of size $n \times n$, are used.

In the first step, the image into the ROI is processed using the SK algorithm: the code of

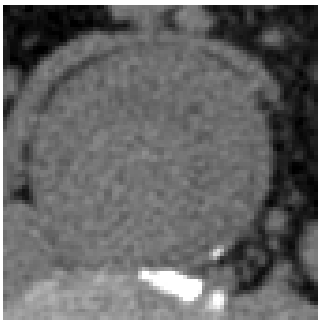

Figure 3.3. ROI of the CT image without contrast medium of figure 3.2 (left), and depicting the aorta artery.

the algorithm is applied using the bidimensional Jackson type kernel and generated by the one dimensional $\mathcal{J}_{12}^{1}(x)$, with scaling factor $R = 2$, where R is the parameter defined in table 3.1, so that the analitical form of the corresponding function is available. This step will reveal to be particularly useful in the whole procedure for the reduction of the errors in the segmentation, as it will be shown in the following numerical examples.

The procedure continues working on the portion C of the above image (processed by the SK algorithm) obtained selecting the artery with a "circular curve" inside the enhanced ROI. The goal of this manual procedure, in some sense avoidable as said before, is to exclude from the ROI other vascular structures too similar in terms of gray levels to the aorta artery but not belonging to it. For technical reasons, in order to work always with square matrices, all the pixels outside the above selected area are set to zero (zero padding). A filter based on the wavelet decomposition by the "Mexican hat" mother wavelet, implemented by the "á trous" algorithm (see, e.g., [62, 67]), is applied to the image C obtained from the previous step. The implementation of the wavelet decomposition consists on a filter bank in the frequencies domain, splitting the different components of the image into 5 levels (or bands), C_i, $i = 0, 1, ..., 4$, each one with its own frequencial content. The images C_i contain the high frequency contributions to C. The number of levels has been chosen according to the physical dimensions of the structures under analysis, supposing that the size of the lumen of the vessel is bigger that a square of $2^4 \times 2^4$ pixels (where the exponent 4 denotes the lowest wavelet decomposition frequency), see, e.g., Table 3.2 for the features of the experimentally used images.

From the image C, and the above components C_i, $i = 0, 1, ..., 4$, the *residual image* (see, e.g., [64]) C_r can be calculated as follows

$$C_r \;:=\; C \;-\; \sum_{i=0}^{4} C_i. \tag{3.1}$$

that contains, by construction, the lowest frequencies components of C (see, e.g., Figure 4.8). In general, it is possible to observe that, the pervious zone is hidden inside the vessel but has an higher mean gray value than the occluded one, this difference not being distinguishable at naked eye: it is possible to verify such assertion by increasing the contrast of the original image until to visualize white marks in the pervious zone on a black background. Since in general, the high frequency components of C are too detailed in relation to the dimension of the lumen of the vessel, in C_i, $i = 0, 1, ..., 4$, it is possible to identify the area of interest, while, since C_r contains the low frequency components of C, it allows to evidence the major structures inside the image. Sometimes, in the original image C, light structures (close to the white saturation value) consisting of plaques of

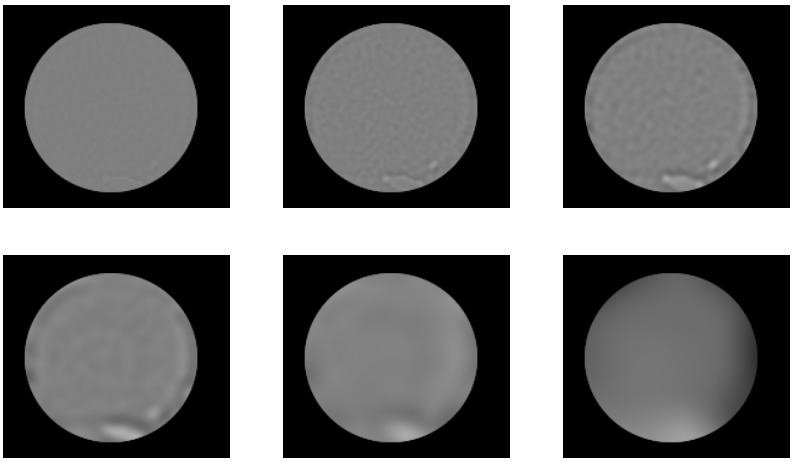

Figure 3.4. Result of the wavelets filter application to a circular portion of the image in Fig. 3.3, previously processed by the SK algorithm. High frequencies components move from top left to down right. Image C_r is in the right bottom corner (second row).

calcium (or other mineral materials) inside the aorta artery, can be found, their presence reducing the contrast of the entire image, influencing the final segmentation of the pervious zone. In order to reduce the effect of such white structures, the algorithm generates a mask image C_p, as follows:

1. the image $\overline{C} = (\overline{c}_{i,j})$ is achieved, i.e., the negative version of $C = (c_{i,j})$;
2. $\widehat{C} := |C - \overline{C}|$ is computed, the symbol $|\cdot|$ denoting the pointwise absolute value of the difference between the above matrices; in the resulting image all the pixels that in C were sufficiently close to the boundary of the interval $[0, 255]$ belong to a sufficiently small left neighborhood of 255, while all the other pixels assume values in a sufficiently small right neighborhood of 0;
3. a threshold equal to 127 is applied to $\widehat{C}$, resulting in the binary image $\widetilde{C}$;
4. for technical reasons, the auxiliary matrix A is generated by applying a threshold equal to 127 to C too;
5. finally, $C_p := \widetilde{C} \wedge A$ is calculated, with the pointwise matrix operation $\wedge$ defined by:

$$\widetilde{c}_{i,j} \wedge a_{i,j} := \begin{cases} 255, & if \quad \widetilde{c}_{i,j} = a_{i,j} = 255, \\ 0, & otherwise, \end{cases}$$

   for any pixels of $C = (\widetilde{c}_{i,j})$ and $A = (a_{i,j})$. The final image $C_p = (c^p_{i,j})$ contains, on a black background, only the light areas of the original image C (i.e., the plaques of calcium), represented by white pixels.

At this point, exploiting the finally achieved mask image C_p, it is possible to eliminate from C_r the artifacts generated by the presence of calcifications. For notation simplicity, the new image filtered by C_p is denoted with the same pre-filtering symbol C_r. In order to enhance its contrast and to increase the difference among the various pixels, C_r is linearly normalized and equalized, achieving $C_{r,\,N,\,E}$. The crucial step of the procedure is the segmentation of the pervious lumen of the artery, consisting in the determination of a suitable threshold for $C_{r,\,N,\,E}$.

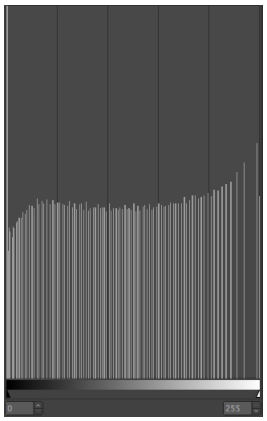

Figure 3.5. Monotone histogram

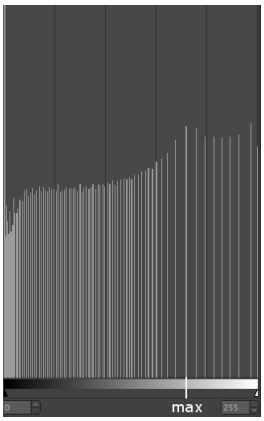

Figure 3.6. Two relative maximums histogram

The above threshold value is automatically computed exploiting the two possible trends of the histogram associated with $C_{r,N,E}$ (see Figure 3.5 and Figure 3.6):

1. increasing on the gray levels interval [127, 255] (see Figure 3.5);
2. with two relative maximums $s_1 < s_2$, assumed respectively at g_1 and g_2, on the gray levels interval [127, 255] (see Figure 3.6).

The above classification can be obtained after the application of a "low pass filter", i.e., analyzing the behavior of the histogram of the image in a neighborhood of each point under analysis, and neglecting all the variations less than a suitable fixed value (varying between the $0 - 20\%$ on the basis of the shape of the histogram) along the vertical axes. In particular, the distance between the two contiguous bars of the histogram closer to the determined maximum, results at least bigger or equal to d_m increased by $2\sigma_d$, where d_m denotes the mean value of the distances between any pair of contiguous bars of the whole histogram, and σ_d represents the associated standard deviation. In the first of the above cases, the shape of the histogram suggests that, the lighter zones, i.e., the areas of $C_{r,N,E}$ with gray levels belonging to the interval [127, 255], are quite homogeneous, in the sense that they can be associated to the same anatomical structure, hence the threshold is chosen equal to the mean value of the range $[0, 255]$, i.e., $\theta_1 = 127$.

In the second of the above cases, the presence of the two maximums is connected to the existence of two different anatomical zones, both placed in the areas corresponding to the range of gray levels [127, 255]. For this reason, the threshold value $\theta_2 = g_1 + 1$ is preferred, since the above procedure for the computation of the maximum provides that the closest gray level bar bigger than g_1 (and also than θ_2) in the histogram is sufficiently spaced along the horizontal axes, to justify the presence of two distinct anatomical structures. Note that, the experimental evidence confirms the previous assertion. By the application of the above threshold, a binary image C_F, where the white pixels represent the extracted lumen of the artery, is achieved. The thresholding values coming from the procedure described above have been compared with the ones deriving from the application of Otsu method [98]. As shown in what follows, the results of the proposed method are ameliorative if compared with the ones achieved applying Otsu.

For a pseudo code see table 3.1. An example of the result obtained from the procedure described is shown in figure 4.6, where the pervious zone has been extracted from the original image of figure

Objective: Segmentation of the ROI depicting the aorta artery, in order to extract the lumen of the vessel.

Inputs: ROI of the CT images without contrast medium, I, $n \times n$ pixel resolution

Main steps:

- Application of the sampling Kantorovich algorithm to I, with scaling factor $R = 2$, Jackson-type kernel J_{12}, and $w = 15$, obtaining an $N \times N$ image, with $N = n\,R$;
- Selection of the circular area surrounding the artery and generation of the image C;
- Application of the wavelet filter, and generation of the image C_r;
- Computation of the mask image C_p;
- Removal of the plaques of calcium from C_r using the mask C_p;
- Normalization and equalization of C_r, obtaining $C_{r,N,E}$;
- Computation of the threshold value for the final segmentation;

Output: Image C_F showing the lumen of the artery.

Table 3.1. Pseudo-code of the segmentation algorithm.

4.4. The advantages coming from the applications of the SK algorithm can be seen in figure 4.9: the contour of the pervious zone, extracted from the image processed by the SK algorithm, is more accurate than the corresponding one obtained elaborating the original image. The gold standard reference for the comparison is, again, the CT image with contrast medium.

Remark 3.1.1. Note that, the above procedure can be simplified by avoiding a double manual selection of the ROI, e.g., directly using a ROI of circular shape surrounding the aorta artery. Automatic methods for such selections are also available in literature. To not loose the focus on the SK algorithm such technical details have been omitted in the discussion.

The results coming from numerical simulations have been compared, by superposition, with the extracted areas of the lumen of the vessels in the corresponding contrast medium reference images.

Figure 3.7. Final result of the segmentation algorithm applied to the image in Figure 3.3.

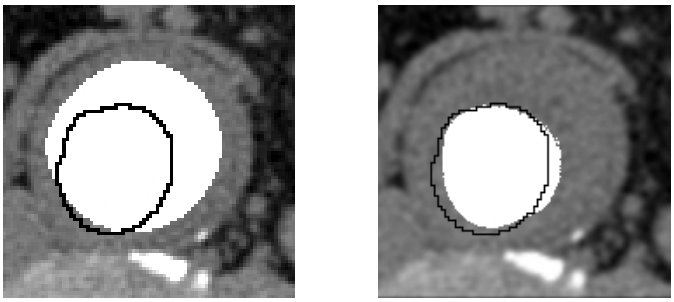

Figure 3.8. On the left, the lumen of the vessel (white area), extracted from the original image (i.e., Figure 3.3), is compared with the pervious zone from the corresponding CT image with contrast medium contoured by a black line. On the right, the lumen of the vessel (white area), extracted from the original image previously reconstructed by the SK algorithm, is compared with the pervious zone as before. The advantages in the approximation produced by the SK algorithm appears evident.

From now on, the symbol $CM = (cm_{i,j})$ will denote the area on the CT image with contrast medium corresponding to the ROI (of the original CT without contrast medium) in such a way that, they are superposable.

Seq. n. 1	#51
Slice's thickness	2.5 mm
Spacing between slices	1,25 mm
Resolution	1,280 pixel/mm
Pitch	0,953
Seq. n. 2	#9
Slice's thickness	3.0 mm
Spacing between slices	3,00 mm
Resolution	1,314 pixel/mm
Pitch	1,375
Seq. n. 3	#98
Slice's thickness	2.0 mm
Spacing between slices	1,00 mm
Resolution	1,463 pixel/mm
Pitch	0,938
Seq. n. 4	#44
Slice's thickness	2.5 mm
Spacing between slices	1,25 mm
Resolution	1,164 pixel/mm
Pitch	0,891
Seq. n. 5	#31
Slice's thickness	2.5 mm
Spacing between slices	1,5 mm
Resolution	1,219 pixel/mm
Pitch	0,953

Table 3.2. CT technical features. Image size, for each sequence, is 512×512.

One of the biggest problem in medical image analysis remains the lack of gold standard references (e.g., atlas), while manual segmentation appears time consuming as well as strictly connected with the available visualization devices and the expertise of the medical users [55]. To overpass this limitation, an automatic way for the segmentation of the pervious lumen of the aorta, in contrast medium images, is suggested.

Before proceeding with the segmentation it is necessary to filter possible artifacts due to the presence of calcifications inside the artery, and to superpose the two different images taking into account of some anatomical or artificial landmarks.

Some algorithms available in literature, preliminarly tested for the segmentation of the contrast medium area (see, e.g., [76, 19, 78]), revealed to be scale variant, influencing negatively the accuracy and the reproducibility of the method. The main errors could occur extracting areas with not convex shape and with multiple edges, reasons good enough to prefer other segmentation techniques.

To generate the reference C_p, previously determined and suitably scaled without interpolation at the same size of CM, a suitable mask is applied to remove, from the image, the plaques of calcium placed in the artery. This filtering operation follows the rule

$$CM(i,j) = \begin{cases} 0, & if\ C_p(i,j) = 1, \\ CM(i,j), & otherwise, \end{cases}$$

for each point (i,j) belonging to CM. Note that, in order to not alter the data contained in CM, assumed as reference, it is preferable to reduce the size of C_p instead of increasing the size of CM.

Being the contrast medium highly radio opaque, a suitable threshold to segment the pervious area is $\eta = 127$, whose value is equal to the midpoint of the range $[0, 255]$. After the thresholding operation the binary image CM_b is obtained. The choice of η seems to be the most suitable since the effect on the CT by the contrast medium introduction is the saturation of the gray levels of the pixels corresponding to the interested areas. Indeed, the above choice allows to include in the pervious zone the pixels of the boundary corresponding to hardware CT sensors having, during the data acquisition phase, at least a half occupied by the contrast medium (i.e., with a gray level greater than $\eta = 127$). The reference extraction process described above uses images deriving from a windowing procedure analogous to the one applied in case of no contrast images, with parameters selected by medical specialists. In Table 3.3 a pseudo code of the algorithm for the automatic extraction of the pervious area CM_b, from CM, is given.

Finally, CM_b is comparable, by superposition, to C_F. In Figure 3.9 the white area of CM_b is superposed to the original CT image without contrast medium. Various errors are computed in order to evaluate the accuracy of the results, e.g., DCI, TI, E_m (see Section 1.6).

In Table 3.4 some results concerning the previous analysis applied to some of the images belonging to the above sequences are provided. In the images of the central column of Table 3.4 it is possible to note how the segmentation algorithm is able to distinguish the calcifications without including them in the pervious zones. This aspect is not negligible since, in general, in CT images with contrast medium it is not possible to distinguish plaques of calcium from the pervious areas.

Moreover, some other considerations have to be done on the errors calculated in Table 3.4. The DCI and TI show good values of similarity and E_m low error rates. In particular, E_m values are quite the same of the complementary of TI (i.e., 1-TI) and bigger than the complementary values of DCI (i.e., 1-DCI). For this reason it is possible to use this index to compare with other segmentation methods, i.e., where the threshold is calculated using the standard Otsu method [98]. In particular, it appears that the new proposed thresholding procedure gives, in general, better results than Otsu (see Table 3.6). This could be explained considering that Otsu does not select the threshold as the minimum value between two maxima in a bimodal histogram but minimizes the intra classes

Objective: Extraction of the pervious area from CM

Inputs: CM image, $n \times n$ pixel resolution
C_p image, $N \times N$ pixel resolution, $N = n\,R$, $R = 2$

Main steps:

- Resize of C_p by the scaling factor $1/R$;
- Deletion of the pixels corresponding to the plaques of calcium from CM using the scaled C_p
- Thresholding of the above modified CM

Output: Binary image CM_b, where the pervious area (contrast medium area) is white

Table 3.3. Pseudo-code of the algorithm for the automatic extraction of the pervious area of CM.

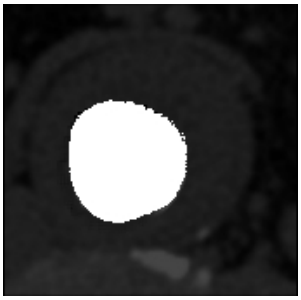

Figure 3.9. In white the pervious zone of the vessel obtained from CM_b. In the background, in transparency, the original image for reference (C_F).

variance. In CT images without contrast medium the gray levels of the signal are so similar that a strict separation between the two modalities could be not possible, resulting in a more approximated and less accurate segmentation. For sake of completeness, in the algorithmic implementation for this particular issue, the Otsu thresholding method does not take into account the pixels of the histogram at value 0: these pixels represent the background signal, they derive from previous image elaborations and, if not excluded, they will affect the segmentation process, representing a third modality of the distribution in the histogram.

CT Image	EX image	CM Image	DCI	TI	E_m
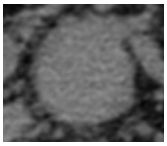	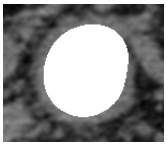	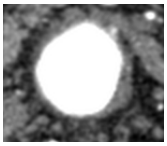	0,90	0,82	0,17
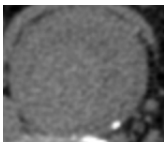	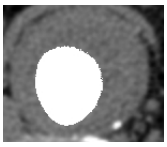	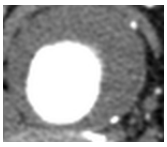	0,90	0,81	0,18
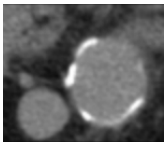	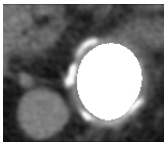	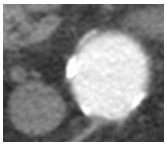	0,92	0,85	0,15
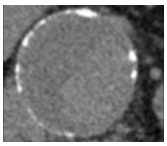	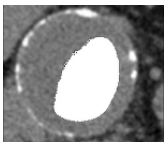	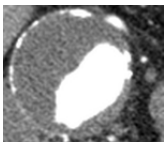	0,79	0,64	0,35
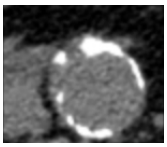	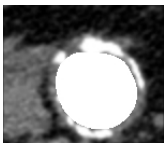		0,94	0,89	0,11
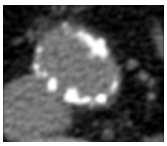	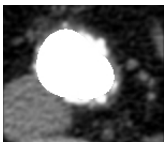	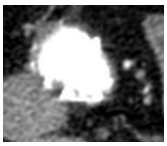	0,92	0,86	0,14
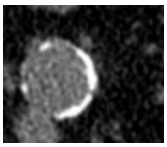	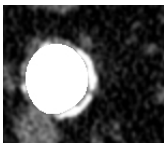	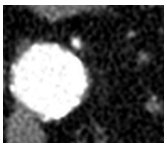	0,92	0,85	0,14

Table 3.4. Starting from left: in the first column the square ROI selected from the original CT image; in the second column the corresponding results after the application of the segmentation algorithm; in the third column the corresponding CT image with contrast medium. The last three columns report, respectively, the corresponding Dice Coincidence Index (DCI), the Tanimoto Index (TI) and the misclassification error (E_m).

In order to give a complete evaluation of the above numerical results it is opportune to consider that the starting images are completely homogeneous and useless to perform even an approximate medical diagnosis. As introduced in Section 1.6, the misclassification error is a severe measurement

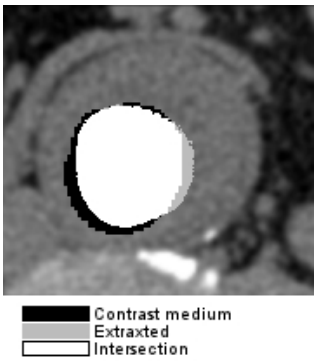

Figure 3.10. Superposition of the pervious zone extracted by the algorithm (in light gray) and the lumen of the vessel individuated by the contrast medium reference (in black). The white zone represents the pixels correctly classified. In the above image E_m=0,24.

of the discrepancies between the extracted contours and the original contrast medium image, if compared to the visual diagnostic methods commonly used by vascular surgeons (see Figure 3.10). For this reason the normalized version E_n of the misclassification error can be evaluated. Another important factor in order to plan a surgical vascular intervention, is the shape of the occlusion, estimated by the circularity shape factor [95], connected with the shape error E_s.

In this specific case, thanks to the regularization property of the SK operators, it results $Circ_{CM} \leq Circ_{C_F}$, thus $0 < \dfrac{Circ_{CM}}{Circ_{C_F}} \leq 1$.

Moreover, Hausdorff distance H_{dc} between the contours of the extracted zone compared with the contrast medium reference, together with the Hausdorff distance H_d between the full set given by the extracted zone compared with the contrast medium reference, have been calculated.

It could be of some importance to evaluate if the algorithm tends to over or under estimate the pervious zone. To consider this behavior the index B_{pn} can be used.

Other than the misclassification and the shape errors, it is important to consider which is the difference in terms of extracted area between C_F and CM_b, considering that from a medical point of view the blood flow depends on the area of the pervious zone. To estimate the morphological differences between the extracted zones and the references, the distance between the centroids of the sets ΔD_c, the difference between the extracted diameters ΔD_a, in this case restricting the definition only to the boundary of the bidimensional sets, geometrically being of interest the blood flow in the aorta artery.

The difference between the area in C_F and CM_b, can be quantified: ΔA_a has a normalized formulation and it always belongs to the interval $[0, 1]$.

In Table 3.5, DCI, TI, E_m, E_s, E_n are shown for each image of an entire sequence and in mean for all the sequences; in Table 3.6 the same measurements, together with $E_{m_{Otsu}}$ and B_{pn}, are reported in mean.

Seq. 5	DCI	TI	E_m	E_s	E_n
	0,82	0,70	0,30	0,13	0,22
	0,84	0,72	0,28	0,11	0,20
	0,82	0,70	0,30	0,11	0,22
	0,84	0,72	0,28	0,16	0,19
	0,83	0,71	0,29	0,11	0,20
	0,83	0,71	0,29	0,09	0,21
	0,83	0,71	0,29	0,09	0,21
	0,82	0,69	0,31	0,07	0,23
	0,83	0,70	0,29	0,09	0,21
	0,81	0,68	0,32	0,09	0,24
	0,82	0,70	0,30	0,13	0,22
	0,81	0,67	0,32	0,13	0,24
	0,85	0,73	0,27	0,22	0,18
	0,83	0,72	0,28	0,17	0,20
	0,85	0,73	0,27	0,21	0,19
	0,84	0,72	0,28	0,22	0,20
	0,85	0,73	0,27	0,25	0,19
	0,87	0,76	0,24	0,16	0,16
	0,87	0,76	0,24	0,23	0,16
	0,89	0,80	0,20	0,30	0,13
	0,88	0,79	0,21	0,21	0,13
	0,87	0,77	0,23	0,26	0,15
	0,88	0,79	0,21	0,34	0,13
	0,89	0,80	0,20	0,32	0,12
	0,88	0,79	0,21	0,20	0,13
	0,91	0,84	0,16	0,16	0,09
	0,88	0,78	0,22	0,29	0,13
	0,88	0,79	0,21	0,27	0,11
	0,92	0,85	0,15	0,32	0,08
	0,92	0,84	0,16	0,26	0,09
	0,92	0,85	0,15	0,28	0,09
Mean	0,86	0,75	0,25	0,19	0,17
Std. Dev.	0,03	0,05	0,05	0,08	0,05

Table 3.5. Numerical errors for the sequence N. 5.

Seq. n°	DCI	TI	$E_{m_{mean}}$	$E_{m_{mean-Otsu}}$	$E_{s_{mean}}$	$E_{n_{mean}}$	B_{pn}
1 (Mean)	0,82	0,71	0,28	0,31	0,05	0,12	0,07
(Std. dev.)	0,08	0,12	0,12	0,18	0,03	0,06	–
2 (Mean)	0,86	0,77	0,24	0,25	0,18	0,14	-0,00
(Std. dev.)	0,05	0,07	0,07	0,07	0,08	0,05	–
3 (Mean)	0,79	0,62	0,37	0,46	0,09	0,13	-0.37
(Std. dev.)	0,06	0,14	0,14	0,13	0,08	0,07	–
4 (Mean)	0,79	0,67	0,33	0,32	0,13	0,16	0,02
(Std. dev.)	0,12	0,16	0,16	0,15	0,13	0,08	–
5 (Mean)	0,86	0,75	0,25	0,28	0,19	0,17	-0,32
(Std. dev.)	0,03	0,05	0,05	0,07	0,08	0,05	–
Mean	0,82	0,69	0,31	0,37	0,11	0,14	0,07
Std. Dev.	0,08	0,13	0,13	0,16	0,09	0,07	–

Table 3.6. Mean and standard deviation of the numerical errors for each of the analyzed sequences.

Geometrical and morphological measurements and related morphological errors have been reported in mean in Table 3.7.

Seq. n°	$\Delta H_{d_{mean}}$	$\Delta H_{dc_{mean}}$	$\Delta D_{c_{mean}}$	$\Delta D_{a_{mean}}$	$\Delta A_{a_{mean}}$
1 (Mean)	13,47	13,91	7,32	0,35	0,17
(Std. dev.)	5,04	5,46	3,49	0,13	0,08
2 (Mean)	15,51	15,87	9,36	0,26	0,14
(Std. dev.)	2,91	3,07	4,04	0,03	0,05
3 (Mean)	23,06	23,17	9,22	0,37	0,24
(Std. dev.)	11,87	11,85	4,53	0,10	0,11
4 (Mean)	19,78	20,47	2,81	0,28	0,21
(Std. dev.)	6,79	6,88	1,59	0,06	0,12
5 (Mean)	14,13	14,15	2,02	0,23	0,14
(Std. dev.)	2,89	2,84	1,38	0,01	0,03
Mean	18,86	19,15	7,06	0,33	0,19
Std. Dev.	9,58	9,06	5,24	0,11	0,10

Table 3.7. Mean and standard deviation of the numerical geometrical and morphological errors for each of the analyzed sequences. All the values are measured in pixels.

All the indexes for the evaluation of similarity of binary sets have been introduced in Section 1.6. As demonstrated by the results of Table 3.4, the extraction algorithm identifies the position of the pervious zone into the vessels with a good degree of approximation.

On the other hand, for the sake of completeness, there are some aspects that have to be taken into consideration in order to give a complete analysis of the performance of the described methodology. The results are strongly connected to the "visible" part of each image that depends on the real anatomical texture of the biological tissues as well as on the accuracy of the CT exam (e.g., contrast setting of the CT apparatus, noise during the measurement, etc). Moreover, starting from images whose distribution of gray levels is homogeneous, it is difficult to obtain very accurate numerical results. The DCI similarity indexes show values bigger or approximatively equal to 80%.

The resolution of the measure strictly depends on the procedure for the computation of the

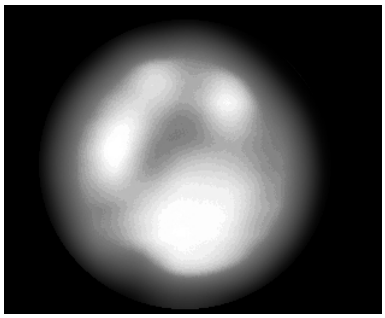

Figure 3.11. An example of a 3-zones image in which the three white zones are not each other four-connected.

threshold: the areas of the extracted zones varies with the number of pixels, corresponding, in the histogram of $C_{r,N,E}$, to the gray levels closer to the threshold.

Another point to take into account is the presence, in the entire sequences or just in some images of them, of different, not 4-connected (polyominoes), light zones in $C_{r,N,E}$: even if one of the above is the real pervious zone, the only discriminating criteria that can be used to choose the right one, is its geometrical dimension, assuming that the pervious zone is the most extended one in the set. When this condition is not satisfied a wrong extraction could result, affecting the value (in percentage) of the mean errors.

Despite this reason, critical images, like the one shown in Figure 3.11, have not been excluded a priori, in order to perform a complete cases analysis.

The new proposed method obtains a separation between the lumen of the aorta artery and the vessel itself, more accurate with respect to the one obtained from the original not reconstructed image. The possibility to identify the lumen of the vessel without the use of the contrast medium is crucial from a medical point of view, and could allow the vascular surgeons to perform accurate diagnosis of the pathologies of the vascular apparatus even without the introduction of contrast medium.

The proposed procedure opens the way to overcome the inability for the doctors to perform a vascular diagnosis without contrast medium, given that CT images with contrast medium still represents the gold standard procedure to diagnose aneurysmatic pathologies. Moreover, the presence of errors in the evaluation of the extraction seems to not affect the final medical diagnosis.

The developed procedure is completely automated after the ROI selection (as observed in Remark 3.1.1) in the extraction of the pervious zones as well as in the calculation of the errors. Further, differently from other studies proposed in literature (see, e.g., [125, 80]), here also the reference CT image with contrast medium is extracted automatically allowing the reproducibility of the test, which results, for this reason, not operator dependent.

The execution time of the procedure on an entire set allows the processing of an entire sequence in a reasonable time.

Even if the method has been tested on a considerable number of images, further investigations are needed to confirm its validity even in general cases of noisy CT scans, to determine a Signal To Noise Ratio limit for its applicability. This task could be the object for future investigations. The results of this application want to point out the possibility of a software segmentation of the pervious aortic lumen directly from the analysis of the CT scans even when the acquired signal appears homogeneous and even if different functional zones are not distinguishable at naked eye.

3.2 Investigation of Retinal Tissues for diagnostic purposes [2]

The aim of this section is to provide an improvement in the reconstruction and visualization of retinal choriocapillaris images from normal patients. The implemented method starts from multiple Optical Coherence Tomography (OCT) scanned sequences, performs a registration, an average and a filtering on them using for this last step the SK operator. The resulting images are then analyzed with some well known methods in literature in order to quantitatively evaluate the improvement achieved. Also fluoroangiographic and histological images are introduced like references to support the reliability and the goodness of the results.

The OCT technology allows to reconstruct the vascularization of both the Superficial Capillary Plexus (SCP) on the retinal fundus as well as that of the deeper Choriocapillaris (CC) tissues.

The process of multiple acquisition and averaging of CC images, which are rigidly connected with SCP corresponding scans, has been recently introduced in some works ([117, 115, 116, 37]). The idea is to acquire multiple sequences (at least 4, see [37]) from the same patients, to register the SCP images taking one scan as reference, and to operate the same geometrical transformation on the corresponding CC images, for each sequence. The registration procedure uses the ImageJ/Fiji Turboreg algorithm [113], in order to operate a first affine transformation and a first rough superposition of the SCP images coming from the previous multiple sequences. In general, the above registration algorithm is based on the minimization of the MSE between the two involved images. Each SCP affine transformation is recorded and subsequently applied to each corresponding CC images for each sequence of the set under analysis. In this way SCP images and corresponding CC images are subjected to the same modifications. After this first coarse registration procedure, a supplementary finer one, based on the ImageJ/Fiji bUnwarpJ algorithm [104, 4], is performed on the SCP and, as before, reported on the corresponding CC images, using the ImageJ/Fiji Multi-Scale Oriented Patches (MOPS) feature extraction method [63, 87, 25]. This algorithm operates an elastic transformation on the source image (the one to be modified) in order to minimize the MSE respect to the target (the one assumed as reference).

The process, computationally heavy, could result in a not correct registration if target and source are considerably different one from the other. For this reason this kind of registration will not be applied to the fluoroangiographic image. The whole procedure ends with an averaging operation on one hand, between all the achieved SCP, and on the other hand, between all the CC images. The mean process is certainly useful to reduce, or to the limit suppress, the noise of the measurement, assuming its model being linear.

At this point the SK algorithm is applied to both the images resulting from the averaging procedure, SCP_{AV} and CC_{AV} respectively; this is driven by two distinct reasons:

- to increase the image size in order to help the medical visual inspection and diagnosis;
- to filter the noise inherently connected with the OCT acquisitions.

By hypothesis, the random noise present in the data can be generally characterized by an additive model, considering that OCT scanning process is itself the result of a mean on multiple acquired signals: this justify the application of an SK-like filter (see [48]).

The morphology of the vessels in both the SCP and CC tissues tends to create "4-connected zones" (polyominoes) that, from now on, will be generically designed as *clusters*. The presence of clusters depends on the anatomy of the ocular fundus, whose vessels, in depth developing through different tissues, creates a capillary network going from more superficial layers to deeper ones. This behavior is more evident in the anatomy of the CC tissues but it is realistic in SCP ones too.

[2] Results contained in this section are almost ready to be submitted.

Figure 3.12. Example of SCP images after the application of local Otsu (center) and Phansalkar (right) thresholding procedures on the original image (left). The Otsu method results in an over-segmentation of the macular zone while the Phansalkar tends to over connect vessels.

For evaluation reasons, after the reconstruction and filtering process, given healthy patients, it is convenient to measure the number of clusters and the area they cover to understand if the applied methodology results in a quantitative enhancement.

Before the clusters counting, a local thresholding procedure is needed. In literature, several local automatic thresholding methods are available.

Despite this, a new hybrid thresholding procedure is proposed, mixing the results achieved by Otsu [98] and Phansalkar [102]. More in detail, local (i.e., adaptive) Otsu thresholding method over-segments uniform zones, like the macula in the SCP images (see Figure 3.12 left), resulting in a wrong classification. This is because the Otsu method assumes a bimodal distribution of the gray values in the area under analysis, even if this is not necessarily always true. On the other hand, Phansalkar procedure is strongly dependent on the choice of the thresholding parameters and it risks to over connect vessels. For these reasons, a combination of them can result to be the best choice. In Figure 3.12 an example of the distinct application of the two methods is shown.

In Figure 3.13 the difference D between the application, on the same image, of the local Phansalkar thresholding procedure and the local Otsu method is shown. D is calculated according to the following formula

$$D = \max\{(B_P - B_O), 0\},$$

where B_P is the binary image achieved through the application of the local Phansalkar thresholding procedure and B_O is the binary image resulting from Otsu. It is evident (see Figure 3.13 again) that the local Phansalkar thresholding procedure tends to under segment the image and risks to produce artificial connections among different vessels.

In the SCP images elaboration, a mixed automatic method that performs a local Phansalkar thresholding in the macular zone and a local Otsu thresholding in the remaining part is preferable (see Figure 3.14).

On the other hand, the CC images (see, e.g., Figure 3.15 right), where there are not uniform areas, have been thresholded using a local Otsu procedure.

For what concerns the reference images, a different logic has driven the segmentation of the histological tissue. Starting from the knowledge of the anatomy of the vascular network, it is expected that the thresholding procedure will result in a strongly connected network or, to the limit case, in one single connected cluster covering the whole image. The histologic image, acquired with an electronic microscope, has a higher resolution and much more details than the CC OCT scanned images. In frequency domain this implies the presence of more meaningful high frequency

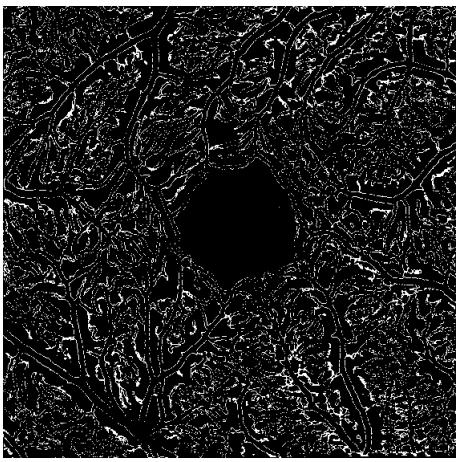

Figure 3.13. Image D. It is evident the under segmentation compared to the local Otsu method and the consequently risk to over connect vessels.

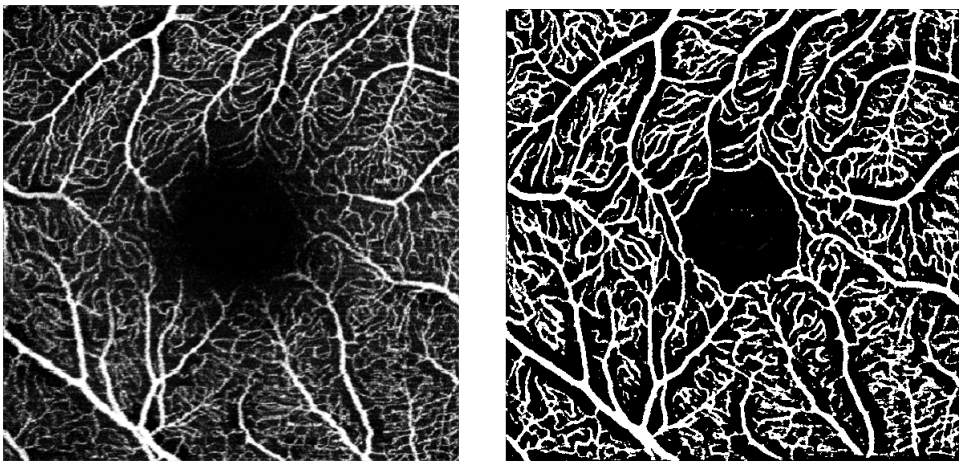

Figure 3.14. Example of the application of the proposed hybrid thresholding methodology on one single SCP image (original on the left). On the right, the macular area results from the local Phansalkar thresholding, the remaining part is binarized using the local Otsu procedure.

components. Due to these components, that can also operate like impulse noise, and to the fact that Otsu method is based on bimodal distribution of the histogram associated to the image or to subsets of it, it tends to give not realistic results, producing over-segmentation (the situation in some sense is the opposite to the one previously described). For this reason the Phansalkar thresholding procedure has been preferred in this case. A prove of the correctness of the choice is given carrying the frequency spectrum of the histological image at a comparable level with the CC OCT scans, i.e., applying a suitable linear filter to suppress the exceeding high frequency components. In the latter case, if the Otsu thresholding method is applied, the results are assimilable to what achievable with the Phansalkar procedure (see Figure 3.18). In what follows, in each binary image, the white points represent, if not diversely specified, pixels belonging to vessels, the other way around the black points.

To perform an analysis of the results, two well known textural indexes have been used. More precisely, the Angular Second Moment (ASM) and the Entropy (E), see Appendix I of [70]. In short, the ASM is defined as:

$$ASM(\theta) = \sum_i \sum_j \{p_\theta(i,j)\},$$

where $i = 1, ..., N$, $j = 1, ..., M$ with $N \times M$ the image size; $\theta \in [0, 2\pi)$ is the angle of evaluation of $p_\theta(i,j)$, that is the so-called normalized co-occurrences matrix[3].

The entropy E, on the other hand, is defined as:

$$E = \begin{cases} 0, & \text{if } p_\theta(i,j) = 0, \\ -\sum_i \sum_j p_\theta(i,j) \log(p_\theta(i,j)), & \text{otherwise.} \end{cases}$$

The presence of a *log* in the formula means that noisy images have bigger entropy than filtered ones. In addition, both ASM and E are normalized to the image size, so that, when operating any dimension changes, they are taken into account.

The averaging process has been operated on twenty normal eyes of different patients, each one OCT scanned six times. Each scan consists of one couple of one SCP and one corresponding CC image, taken at a convenient depth in the ocular fundus, both coded in 8 bits gray scale levels.The spatial resolution of the scan is 3.125 micron/pixel. Each image has an initial area of 1504×972 pixels, reduced considering that the different rotation in the first affine registration process causes some layers to outgo the borders of the target image. This outgoing process, if not considered, would result in a wrong averaging, having lacking signal zones superposed to valid ones (see Figure 3.16). As reference, the best image from the diagnostic point of view, for each sequence, has been chosen like target in the registration process.

To quantitatively evaluate the quality of the SK reconstruction, an image coming from fluoroagiography taken at the same scale of the corresponding SCP sequences, has been used as gold standard. At the same time, an higher resolution histological image, acquired using an electronic microscope, has been analyzed to prove the behavior of vessels network in the CC tissue.

In Figure 3.15 the reconstructions of an SCP and a CC sequence are shown, after the registration and the averaging process. In Figure 3.17 the results after the application of the SK algorithm to the images of Figure 3.15 are shown. The SK algorithm has been applied using the bidimensional Jackson kernel with N=2, w=15 and zoom factor R=2.

In the SCP case, the matching with the gold standard image has been proved registering:

1. the SCP averaged (SCP_A) to the fluoroangiographic reference;

[3]Another term frequently used in literature to design this kind of matrices is "transition matrices".

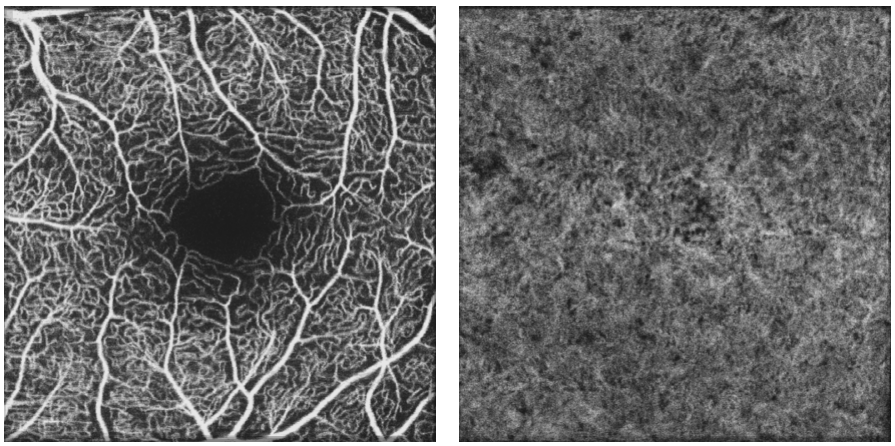

Figure 3.15. Example of results after the registration and the averaging process (no SK applied yet). On the left an example of the SCP image, on the right the corresponding CC.

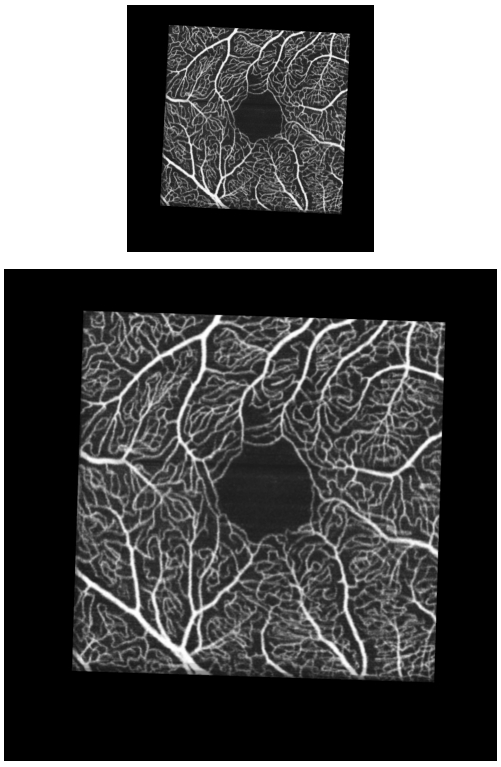

Figure 3.16. Averaged image registered to the fluoroangiographic reference: original size (top), after the SK reconstruction (down). Note the rotation of the image due to the registration process.

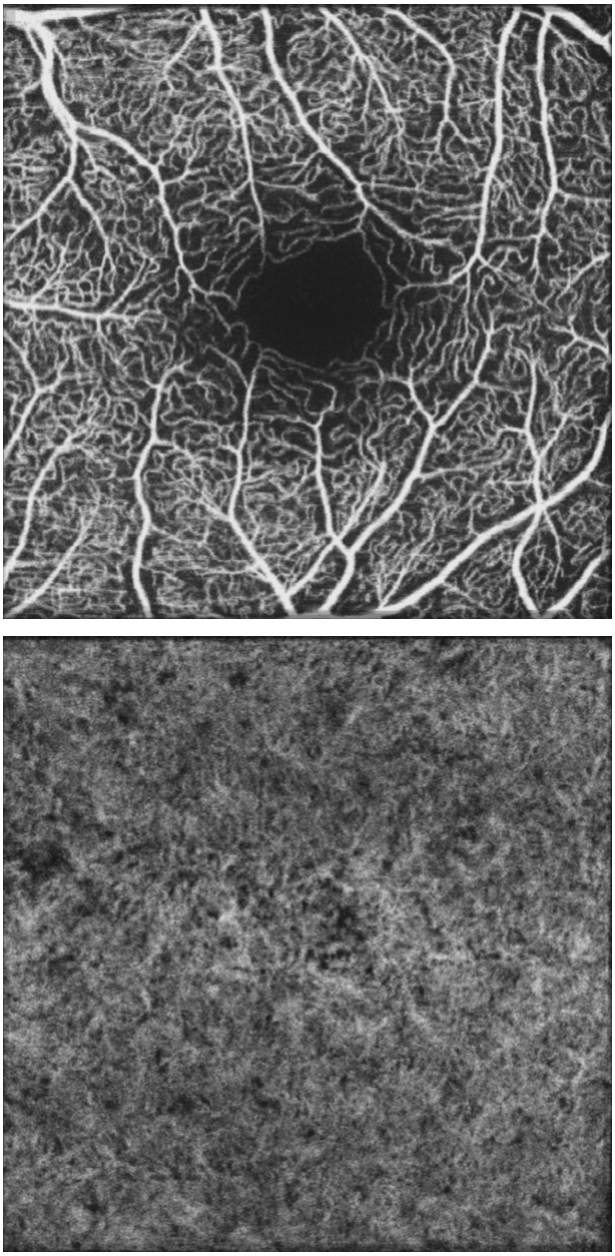

Figure 3.17. Results of the registration, the averaging process and the SK reconstruction on the images of Figure 3.15. At the top, we have the SCP image, while at the bottom the corresponding CC. To highlight the enhancement provided by the SK algorithm, the images are shown with the same visual scale with respect to Figure 3.15: for this reason they appear doubled in size. It is evident the improvement of the visualization for the medical visual diagnosis and investigation.

Type of Processing	$PSNR$	MSE	Area
Averaged (SCP_A)	24.524	229.427	318095 (565×563)
Averaged+SK (SCP_{SK})	25.217	195.804	1272380

Table 3.8. $PSNR$ and MSE from the comparison of the fluoroangigraphic image with the image achieved after the averaging process with and without the SK reconstruction. The Area column shows the number of pixels of the whole image.

2. the SCP after the SK reconstruction (SCP_{SK}) to the SK-filtered fluoroangiographic reference.

The SK reconstruction of the fluoroangigraphic image is needed to compare it with the SCP_{SK} images without applying any other magnification procedure to SCP_{SK}.

Using the $PSNR$ index (see, e.g., [48]) to quantify the improvement related with the SK reconstruction the results shown in Table 3.8 have been achieved.

Since the $PSNR$ in the case of SCP_{SK} is bigger than SCP_A this means that the application of the SK algorithm improves the correspondence with the gold standard images.

In Table 3.9 the results of the cluster counting procedure is shown. The number of clusters of SK reconstructed images is lower than all the other corresponding images in which SK algorithm has not been applied. Moreover, their areas (scaled by the factor R^2) are bigger too. Further, the standard deviation of the areas of the clusters decreases, in proportion, in SK elaborated images. This means that the SK reconstruction method tends to reconstruct in a more realistic way the anatomy of the retinal fundus. In the CC case the matching with the gold standard image, represented by a generic histological image, has been tested using the cluster analysis. The image in Figure 3.18 shows how the vascular network tends to become fully connected, according with the numerical results of Table 3.10 that shows how the number of clusters decreases (mean and standard deviation) contrary to their extension. A textural analysis using ASM and E has been introduced to quantify the improvement coming from the SK reconstruction. In Table 3.11 and Table 3.12 the values of ASM and E are reported for $\theta = \{0°, 45°, 90°, 135°\}$. In all the measurements ASM increases and E decreases after the SK reconstruction. This means that, as expected from theory, the SK tends to filter the high frequency noise in the reconstructed image. The application of the SK algorithm for the enhancement of retinal OCT images allows to improve the visual diagnosis connected with the evaluation of the shape and the density of the vessels in the eye fundus. Moreover, quantitative analysis shows an effective improvement of the images, thanks to the SK algorithm that behaves as a low-pass filter, suppressing, indeed, the main spurious high frequencies components.

SCP P. Nr.	Method	Cluster Nr.	Mean Area	Std. dev. Area	Img. Pixels
1	AVG	523	411.9	5239.7	585225
2	AVG	426	508.9	9461.6	585209
3	AVG	366	597.5	10702.0	585221
4	AVG	351	627.6	11329.0	580635
5	AVG	468	486.0	8529.6	576065
6	AVG	328	727.5	12588.0	586755
7	AVG	1452	118.6	1248.01	579105
8	AVG	1347	154.0	1341.5	588289
9	AVG	845	262.4	5982.2	580643
10	AVG	629	386.2	8409.8	586707
11	AVG	555	427.6	8572.7	588285
12	AVG	492	504.8	9862.8	588285
13	AVG	275	836.4	12941.0	585209
14	AVG	264	844.8	13049.0	580619
15	AVG	326	770.8	13383.0	585209
16	AVG	275	917.7	14337.0	591361
17	AVG	417	520.7	9088.8	583695
18	AVG	371	604.8	10204.0	589823
19	AVG	411	507.0	93196.0	580595
20	AVG	493	427.7	6427.1	591357
MEAN		530	532.1	9100.8	
1	AVG+SK	221	1951.1	13606.0	2340900
2	AVG+SK	166	2627.2	28340.0	2340836
3	AVG+SK	147	3040.8	33358.0	2340884
4	AVG+SK	124	3570.8	35738.0	2322540
5	AVG+SK	173	2764.0	31064.0	2304260
6	AVG+SK	127	3928.7	42016.0	2347020
7	AVG+SK	620	592.7	4107.4	2316420
8	AVG+SK	481	956.6	6054.4	2353156
9	AVG+SK	361	1279.0	10231.0	2322572
10	AVG+SK	246	2066.3	20910.0	2346828
11	AVG+SK	189	2689.9	31299.0	2353140
12	AVG+SK	192	2744.1	23813.0	2353140
13	AVG+SK	85	5550.6	45776.0	2340836
14	AVG+SK	106	4212.9	39619.0	2322476
15	AVG+SK	108	4941.1	49048.0	2340836
16	AVG+SK	115	4645.5	45949.0	2365444
17	AVG+SK	191	2300.9	15641.0	2334780
18	AVG+SK	146	3184.4	29992.0	2359292
19	AVG+SK	179	2196.9	15028.0	2322380
20	AVG+SK	157	2549.4	16942.0	2365428
MEAN		206	2889.6	26926.6	

Table 3.9. From the left to the right: the sequential number describing the patient from which the image comes from (SCP P. Nr.); the method used to modify the image (AVG=averaging only, AVG+SK=averaging and SK algorithm); the number of clusters constituting the network of vessels (Cluster Nr.); the mean of the area of all the previous clusters (Mean Area) and the corresponding standard deviation (Std. dev. Area); the number of pixels of the whole image.

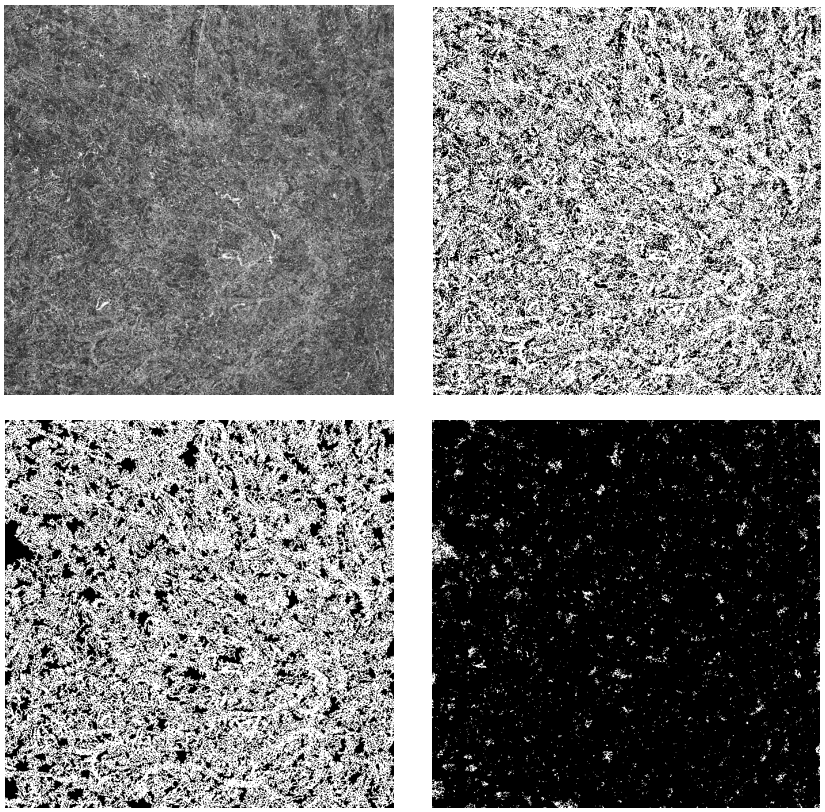

Figure 3.18. Top: on the left the histological image; on the right the corresponding binary image achieved after the application of the automatic Phansalkar thresholding procedure. Bottom: on the left the image of the main cluster coming from histological tissue after the thresholding (points belonging to vessel in white), on the right the remaining clusters (in white pixels belonging to clusters).

CC P. Nr.	Method	Cluster Nr	Mean Area	Std. dev. Area	Img. Pixels
1	AVG	1688	170.0	3247.4	585225
2	AVG	1601	189.7	5717.9	585209
3	AVG	1562	194.7	6245.8	585221
4	AVG	1242	248.8	7607.8	580635
5	AVG	1204	253.2	6418.6	576065
6	AVG	1445	210.6	6353.4	586755
7	AVG	1548	199.3	5872.5	579105
8	AVG	1552	183.4	3147.2	588289
9	AVG	1583	179.6	2500.5	580643
10	AVG	1510	190.8	4327.8	586707
11	AVG	1625	175.3	4101.6	588285
12	AVG	1592	184.6	4421.9	588285
13	AVG	1509	186.3	4338.4	585209
14	AVG	1621	181.3	3677.3	580619
15	AVG	1584	179.2	2647.9	585209
16	AVG	1988	148.6	4454.9	591361
17	AVG	1602	190.5	6164.4	583695
18	AVG	2489	103.4	673.3	589823
19	AVG	2506	109.6	1482.9	580595
20	AVG	1900	134.0	776.1	591357
MEAN		1667	180.6	4208.9	
1	AVG+SK	558	1169.3	17315.0	2340900
2	AVG+SK	513	1348.3	26487.0	2340836
3	AVG+SK	505	1371.2	27361.0	2340884
4	AVG+SK	411	1721.1	28150.0	2322540
5	AVG+SK	400	1735.4	27088.0	2304260
6	AVG+SK	444	1542.1	27967.0	2347020
7	AVG+SK	546	1283.6	24116.0	2316420
8	AVG+SK	493	1324.3	14875.0	2353156
9	AVG+SK	495	1311.6	13392.0	2322572
10	AVG+SK	513	1282.2	19406.0	2346828
11	AVG+SK	491	1328.7	16821.0	2353140
12	AVG+SK	517	1300.9	20944.0	2353140
13	AVG+SK	512	1252.6	18982.0	2340836
14	AVG+SK	540	1232.0	16969.0	2322476
15	AVG+SK	532	1213.3	11848.0	2340836
16	AVG+SK	693	977.9	20377.0	2365444
17	AVG+SK	521	1328.9	22686.0	2334780
18	AVG+SK	869	678.0	4029.6	2359292
19	AVG+SK	766	831.4	10052.0	2322380
20	AVG+SK	646	908.2	4266.1	2365428
MEAN		548	1257.0	18656.6	

Table 3.10. From the left to the right: the sequential number describing the patient from which the image comes from (CC P. Nr.); the method used to modify the image (AVG=averaging only, AVG+SK=averaging and SK); the number of clusters constituting the network of vessels (Cluster Nr.); the mean of the area of the previous clusters (Mean Area) and the corresponding standard deviation (Std. dev. Area); the number of pixels of the whole image.

CC P. Nr.	Method	ASM $\theta = 0°$	ASM $\theta = 45°$	ASM $\theta = 90°$	ASM $\theta = 135°$
1	AVG	4,45E-004	3,23E-004	4,24E-004	3,19E-004
2	AVG	4,07E-004	2,89E-004	3,78E-004	2,89E-004
3	AVG	3,32E-004	2,37E-004	3,06E-004	2,34E-004
4	AVG	4,03E-004	2,85E-004	3,72E-004	2,85E-004
5	AVG	4,80E-004	3,42E-004	4,44E-004	3,40E-004
6	AVG	4,54E-004	3,20E-004	4,10E-004	3,17E-004
7	AVG	6,57E-004	4,53E-004	5,86E-004	4,61E-004
8	AVG	4,77E-004	3,29E-004	4,19E-004	3,30E-004
9	AVG	5,26E-004	3,69E-004	4,85E-004	3,72E-004
10	AVG	4,28E-004	3,03E-004	3,87E-004	2,97E-004
11	AVG	4,23E-004	3,01E-004	3,92E-004	3,01E-004
12	AVG	5,38E-004	3,81E-004	4,93E-004	3,82E-004
13	AVG	4,21E-004	3,01E-004	3,96E-004	3,02E-004
14	AVG	3,85E-004	2,76E-004	3,60E-004	2,75E-004
15	AVG	4,35E-004	2,91E-004	3,72E-004	3,01E-004
16	AVG	4,49E-004	3,11E-004	3,92E-004	3,09E-004
17	AVG	4,13E-004	2,95E-004	3,87E-004	2,93E-004
18	AVG	4,16E-004	2,94E-004	3,85E-004	2,95E-004
19	AVG	4,03E-004	2,79E-004	3,60E-004	2,80E-004
20	AVG	4,02E-004	2,88E-004	3,79E-004	2,88E-004
MEAN		4,45E-004	3,13E-004	4,06E-004	3,13E-004
1	AVG+SK	4,45E-004	3,23E-004	4,24E-004	3,19E-004
2	AVG+SK	9,51E-004	6,70E-004	9,27E-004	6,68E-004
3	AVG+SK	8,43E-004	5,88E-004	7,93E-004	5,79E-004
4	AVG+SK	9,73E-004	6,79E-004	9,22E-004	6,75E-004
5	AVG+SK	1,27E-003	8,86E-004	1,20E-003	8,78E-004
6	AVG+SK	1,17E-003	8,05E-004	1,07E-003	7,95E-004
7	AVG+SK	1,77E-003	1,20E-003	1,63E-003	1,23E-003
8	AVG+SK	1,25E-003	8,42E-004	1,13E-003	8,53E-004
9	AVG+SK	1,23E-003	8,59E-004	1,20E-003	8,75E-004
10	AVG+SK	1,10E-003	7,76E-004	1,03E-003	7,47E-004
11	AVG+SK	1,04E-003	7,27E-004	9,99E-004	7,27E-004
12	AVG+SK	1,34E-003	9,30E-004	1,28E-003	9,44E-004
13	AVG+SK	1,05E-003	7,44E-004	1,03E-003	7,46E-004
14	AVG+SK	9,47E-004	6,74E-004	9,22E-004	6,63E-004
15	AVG+SK	1,13E-003	7,40E-004	9,94E-004	7,73E-004
16	AVG+SK	1,21E-003	8,20E-004	1,08E-003	8,11E-004
17	AVG+SK	1,00E-003	7,16E-004	9,93E-004	7,04E-004
18	AVG+SK	1,02E-003	7,12E-004	9,87E-004	7,17E-004
19	AVG+SK	1,01E-003	6,88E-004	9,22E-004	6,90E-004
20	AVG+SK	1,03E-003	7,23E-004	9,97E-004	7,23E-004
MEAN SK		1,09E-003	7,55E-004	1,03E-003	7,56E-004

Table 3.11. From the left to the right: the sequential number describing the patient from which the image comes from (CC P. Nr.); the method used to modify the image (AVG=averaging only, AVG+SK=averaging and SK); ASM values for $\theta = 0°$, $\theta = 45°$, $\theta = 90°$, $\theta = 135°$.

CC P. Nr.	Method	E 0°	E 45°	E 90°	E 135°
1	AVG	8,009	8,325	8,056	8,335
2	AVG	8,103	8,438	8,174	8,441
3	AVG	8,291	8,624	8,373	8,634
4	AVG	8,112	8,451	8,190	8,450
5	AVG	7,928	8,260	8,008	8,268
6	AVG	7,982	8,327	8,085	8,337
7	AVG	7,667	8,034	7,785	8,016
8	AVG	7,956	8,318	8,077	8,313
9	AVG	7,843	8,189	7,920	8,180
10	AVG	8,051	8,390	8,152	8,409
11	AVG	8,062	8,394	8,135	8,394
12	AVG	7,832	8,171	7,917	8,168
13	AVG	8,073	8,404	8,138	8,401
14	AVG	8,161	8,491	8,225	8,492
15	AVG	8,038	8,436	8,198	8,403
16	AVG	7,999	8,363	8,138	8,369
17	AVG	8,077	8,405	8,140	8,412
18	AVG	8,074	8,415	8,150	8,413
19	AVG	8,096	8,461	8,215	8,456
20	AVG	8,102	8,432	8,163	8,432
MEAN AVG		8,023	8,366	8,112	8,366
1	AVG+SK	7,117	7,440	7,122	7,467
2	AVG+SK	7,253	7,596	7,275	7,602
3	AVG+SK	7,355	7,712	7,416	7,730
4	AVG+SK	7,220	7,580	7,271	7,581
5	AVG+SK	6,954	7,313	7,013	7,320
6	AVG+SK	7,021	7,394	7,109	7,406
7	AVG+SK	6,641	7,032	6,732	7,004
8	AVG+SK	6,983	7,372	7,081	7,361
9	AVG+SK	6,978	7,334	7,004	7,314
10	AVG+SK	7,106	7,456	7,167	7,485
11	AVG+SK	7,159	7,512	7,195	7,510
12	AVG+SK	6,911	7,273	6,955	7,260
13	AVG+SK	7,148	7,496	7,172	7,492
14	AVG+SK	7,261	7,601	7,283	7,613
15	AVG+SK	7,074	7,502	7,209	7,457
16	AVG+SK	7,010	7,396	7,124	7,410
17	AVG+SK	7,188	7,517	7,193	7,533
18	AVG+SK	7,188	7,538	7,217	7,537
19	AVG+SK	7,168	7,556	7,268	7,553
20	AVG+SK	7,160	7,510	7,188	7,508
MEAN SK		7,095	7,456	7,150	7,457

Table 3.12. From the left to the right: the sequential number describing the patient from which the image comes from (CC P. Nr.); the method used to modify the image (AVG=averaging only, AVG+SK=averaging and SK); E values for $\theta = 0°$, $\theta = 45°$, $\theta = 90°$, $\theta = 135°$.

Chapter 4

Application of Sampling Kantorovich operators to problems arising from energy and acoustic engineering

Engineering applications ordinarily face approximation problems. The approximation, in real-world scenarios, depends on different limitations arising at the same time: the intrinsic limitations of the measuring instruments contributes to a not exact data availability; the environmental noise corrupts, by its side, the authenticity of the investigated signal; data missing, together with not exact mathematical models, determine a quite intractable situation. As seen reviewing the theory, as well as considering the results achieved in the medical field, SK operators seem suitable to reduce, by construction, some of the above described limitations. For this reason, the energetic problem connected with the segmentation of thermal bridges for the evaluation of energetic losses in building, and the 3D localization of sources of acoustic noise, have been examined, using the developed theory.

4.1 Detection of Thermal Bridges for Energy Losses estimation [1]

In this section a procedure for the detection of the contours of thermal bridges from thermographic images is proposed, in order to study the energetic performance in buildings. This new method is algorithmically divisible in two logical parts:

- the enhancement of the thermographic images by an optimized version of the SK operators;
- the application of a suitable histogram based thresholding procedure of the enhanced thermographic images.

Finally, an improvement in the accuracy of the parameters defining the thermal bridge is obtained.

The thermographic survey on the building envelope is a useful non invasive method to detect thermal bridges, causes of reduction of the overall energy performance of buildings. In civil and energy engineering, in order to perform non invasive investigations, infrared thermography images are commonly used. The thermography is a technique which allows to measure the heat flux associated

[1] Results contained in this section are published in [7, 8].

with the infrared radiation emitted from every object without direct contact. It supplies a non invasive technique for investigating buildings, see, e.g., [33, 22, 23]. The thermography exploits the peculiarity that any object, having a certain temperature higher than the absolute zero, emits radiations in the infrared range (wavelength from 700 nm to 1 mm, corresponding to the interval of frequencies [300 GHz, 430THz]). The infrared band is located between the visible radiation (in particular the red component, from which the name) and the microwave range.

The result of a thermographic survey is a bidimensional thermal mapping of the heat flux of the object expressed by temperature values, when the emissivity is known.

Thermal bridges are zones of buildings that present a thermal flow higher than the adjacent constructive elements. For this reason, thermographic images appear to be an appropriate tool to study such a problem. The presence of thermal bridges determines the energy losses of efficiency in buildings and this impacts on structural and comfort aspects. In [5, 6] the above investigation has been performed by the help of a suitable index, the so called *incidence factor of thermal bridge* I_{tb} (see formula 4.1 in this section), which points out the energetic incidence of a thermal bridge on the basis of the temperature decrement that it causes. Because of the higher heat flux through the walls, the areas affected by thermal bridges appear colder than the neighborhoods (i.e., darker) in the fictitious visual representation provided by the thermal camera. Measuring the temperature along a single direction results, in presence of thermal bridges, in a U-shaped not uniform trend, as in Figure 4.1. The accuracy of the analysis for the energy performance estimation depends on

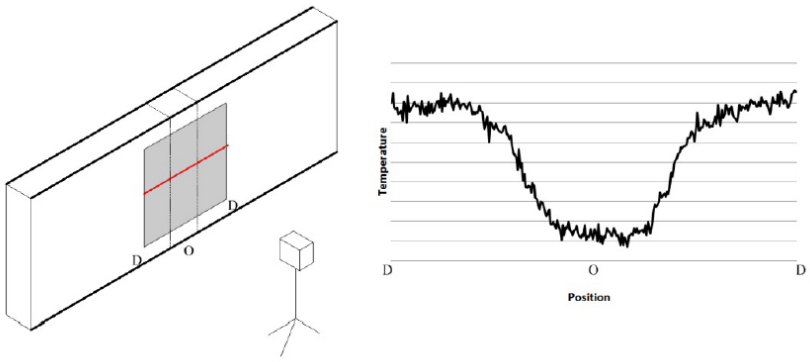

Figure 4.1. Typical U-shaped temperature trend in presence of thermal bridge. The measurement on the right part of the figure corresponds to the red line on the left.

various aspects:

- the correct detection of the areas belonging to the thermal bridges, strictly operator dependent;
- the quality (i.e., the resolution) of the available thermographic data.

The depth of the U-shape is strongly linked to the thermal bridge weakness. Given these limitations, the new method proposed in this section introduces a segmentation procedure which allows to detect the thermal bridges from thermographic images, automating the energetic analysis of the buildings and retrieving more accurate results respect to the original methodology described in [5].

The new algorithm is characterized by various steps. Firstly, the thermographic images are reconstructed and enhanced in their resolution, by the application of the SK operator (see, e.g., [41, 42]). The SK algorithm has been firstly introduced in [49], but its original implementation

was not optimized and required a much longer CPU time for the execution. In this contest a new optimized version of the SK algorithm is given.

For the aim of this problem, the SK algorithm for image enhancement has been implemented by a bidimensional Jackson type kernel and the original resolution of thermographic images improved.

Then, by a probabilistic interpretation of the histogram of the data associated to the above enhanced thermographic images (see, e.g., [77]), a suitable threshold value for the thermal bridge segmentation is determined.

The validation of the proposed method has been obtained from the experimental results effected in a hot box setup with controlled laboratory conditions (see, e.g., [9, 13]). More precisely, three types of bidimensional thermal bridges, with different geometrical shape, have been assembled and subsequently tested. The numerical results show that the proposed algorithm, other to improve the energy analysis of the buildings with respect to the original approach, is able to identify the geometry of the thermal bridges generated in composite walls (i.e., constructed by different materials).

Indeed, such improvement has been validated by a comparison among the factor I_{tb}, firstly computed measuring the temperatures detected by the probes in the hot box, and then by the new method here proposed, i.e., working with the thermographic images, enhanced by the SK algorithm with the shape of the thermal bridge extracted by the automatic thresholding procedure. Moreover, numerical results show that, in thermal bridges caused by the presence of different materials, the method here introduced provides results closer to the reference approach, i.e., to the one completed using probes.

Three cases of thermal bridges have been studied, classified depending on the morphology of the walls on which they appear:

1. 2D thermal bridges - pillar;

2. 2D thermal bridges - beam-pillar joint;

3. 2D thermal bridges -wall-wall joint.

The first two types of thermal bridges occur on plain walls, the first one developing in a straight direction, the second one drawing an angle on the surface. The last category of thermal bridges considers energy losses occurring on two different walls joining with an orthogonal corner. In Figure examples of the pillar and wall-wall joint thermal bridges, specially assembled in laboratory, are shown.

In order to effect a complete analysis on thermal bridges and their energy performance, hot box examples of each one of the typologies above described have been built.The availability of these specimens in a laboratory allows to know all their thermal characteristics. The latter fact will be used to evaluate the goodness of the analysis performed with the new methodology.

Data showed in Figure 4.3, have been acquired by a Flir b360 thermal camera with a 320x240 pixel resolution. The values retrieved from the thermal camera represent temperature data but they can be also interpreted as gray levels of an image, and displayed in a eye-readable format.

As it usually happens in literature, the thermal values have been represented by images coded with a certain color map instead of a grayscale one. Currently, it seems that no automatic procedures are available for the segmentation of the thermal bridges.

At the aim of achieving this result, a specific procedure has been implemented and applied to the original matrix dataset $I = [N \times M]$, with N=320, M=240. To improve the accuracy of the border extraction, the SK algorithm has been used on the native thermal data I, with a scaling factor $R = 2$, $w = 15$, and by bidimensional Jackson type kernel generated by $\mathcal{J}_{12}^2(x)$. In order to speed up the procedure, the SK operators have been approximated by truncation, neglecting all

Figure 4.2. Examples of the pillar structured thermal bridge (left) and the wall-wall joint one (right). Specimens have been build in laboratory for temperature measurements.

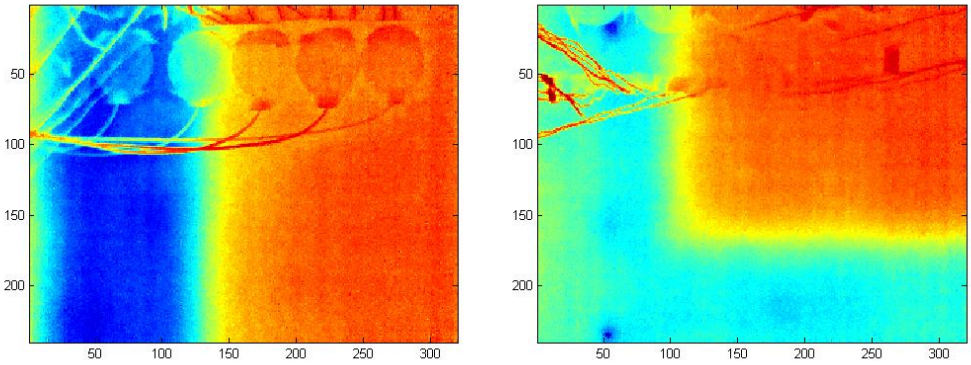

Figure 4.3. The thermal bridges built in a hot-box: on the left, a pillar 2D thermal bridge; on the right, a beam-pillar-joint 2D thermal bridge.

terms with values less than 10^{-4}. This value has been computed taking into account the accuracy of the measurements (that here is 10^{-2}), together with other parameters.

Once the data have been reconstructed using the SK algorithm, the contours of the thermal bridges are extracted by a thresholding procedure, using a parameter obtained from the associated histogram of temperatures (see Figure 4.4).

The procedure for the identification of the threshold value considers that, by definition, the thermal bridges boundaries are zones where the temperature shows a significant gradient compared to its mean value on the entire surrounding area.

More precisely, by the above assumption, it is possible to verify as the data associated histogram

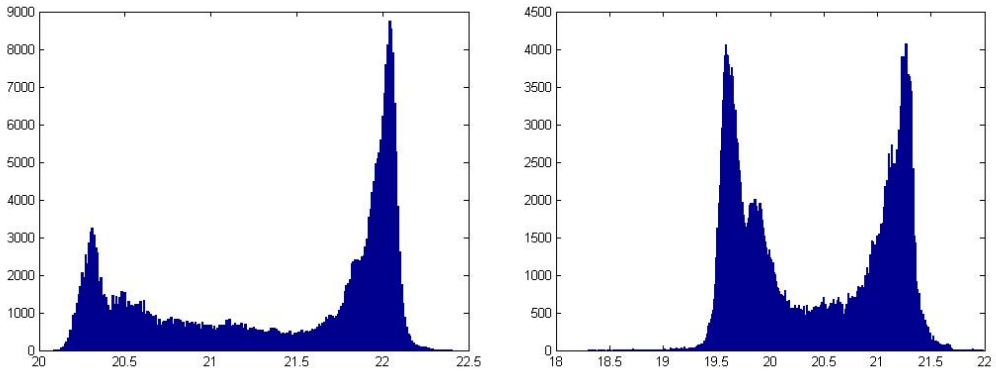

Figure 4.4. Histograms corresponding to the thermal bridges shown in figure 4.3, respectively, which have been processed by the SK algorithm.

exhibits two peaks corresponding to the two biggest relative maximum P_1 and P_2 ($P_1 < P2$), respectively at coordinates $T_{P,1}$ and $T_{P,2}$, with an absolute minimum T_m belonging to the interval $[T_{P,1}, T_{P,2}]$ (see, e.g., Figure 4.5). The threshold value T_m has been chosen as the temperature corresponding to the minimum between P_1 and P_2. This choice is made associating T_m to the minimum error due to the wrong classification of pixels located inside the thermal wall but classified as external, and viceversa (see Figure 4.6).

Note that, if the minimum is achieved at more than one temperature, the higher value among P_1 and P_2 is preferable.

In Figure 4.5, $T_{P,1}$ and $T_{P,2}$ represent the points around which homogeneous temperatures are distributed; therefore, they highlight the thermal bridge area A_B and the external homogeneous area A_E.

From the previous considerations, assuming P_1 and P_2 to be the maximum of two distinct bell shaped functions representing the distribution of probability of a point to belong to A_B or A_E, it is possible to segment the original image I choosing the threshold value equal to T_m. The results obtained from the above segmentation procedure concerning the thermal bridges of Figure 4.3, have been shown in Figure 4.7, and a pseudo-code of the algorithm for the determination of the threshold values T_m is given in Table 4.1. Fixed T_m, it is possible to classify the data in the two mutually exclusive zones A_B and A_E. This method has been standardly used in literature for image segmentation (e.g., [83, 68]) as well as for bimodal distribution statistical analysis. In table 4.2, the temperature of thresholding T_m, determined using the described procedure, is given for each one of the two thermal bridges under analysis.

The results obtained from the applications of the procedure described in this section are represented in Figure 4.7, where the segmentation results are relative to the thermal bridges of Figure 4.3.

The SK reconstruction procedure, when implemented according to Table 4.1, essentially reduces itself to multiply the chosen bidimensional kernel, computed in a suitable grid of nodes, by the starting data set, i.e., the gray levels image I. This numerical calculation can be operated following two basically different approaches:

(1) for each point to reconstruct, runtime recalculating the kernel matrix (see Figure 4.8, left);

(2) at first calculating, for any nodes needed to complete the whole procedure, the kernel matrix,

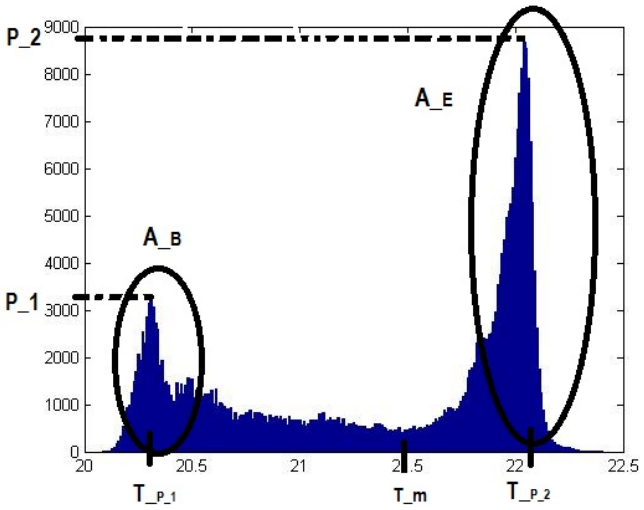

Figure 4.5. Identification of the various parameters on the histogram of the temperatures (concerning the first thermal bridge of figure 4.3), needed in order to compute the threshold value for the segmentation. The oval shaped curves are drawn only to approximatively indicate pixels belonging to the two bigger homogeneous areas, denoted by A_B and A_E.

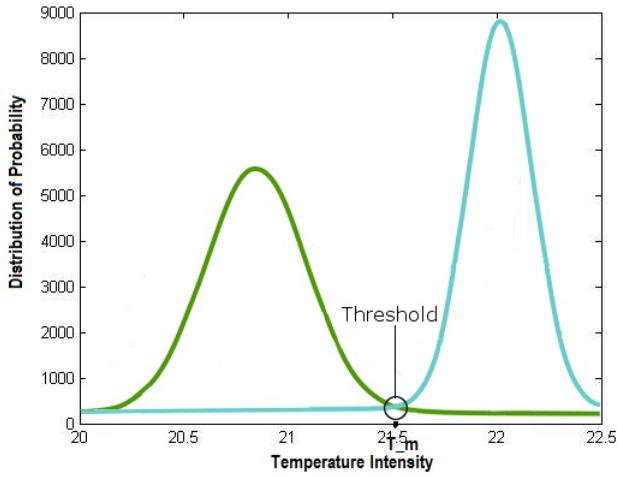

Figure 4.6. Probabilistic interpretation of data values.

sized according to w, and then selecting the portion of interest for any data point (see Figure 4.8, right). In this case, a numerical truncation of the above kernel matrix is convenient, in order to neglect all the values that, certainly, are not significant in the final computation for the reconstruction. This is possible, since the main part of the kernel that provides the most meaningful contribution to the quasi interpolation procedure, is concentrated in a small portion of the domain (see Figure 4.8 again).

Objective: Segmentation of thermal bridges from thermographic data

Inputs: thermographic data of thermal bridges of size 320×240 points

- Application of the sampling Kantorovich algorithm with scaling factor $R = 2$ and $w = 15$ obtaining a matrix of size 640×480;
- Generation of the histogram associated to the data;
- Computation of the minimum between $T_{P,1}$ and $T_{P,2}$.

Output: The scalar threshold value T_m.

Table 4.1. Pseudo-code of the segmentation algorithm for thermal bridge individuation.

Thermal bridge number	T_m
TB. n. 1	21.50 °C
TB. n. 2	20.36 °C

Table 4.2. Threshold values for the analyzed thermal bridges.

Each of these approaches has its advantage: the coding policy (1) requires less memory occupation than (2), while (2) requires a significant small number of arithmetic operations than (1).

In the case (1), given a grayscale image of size $N \times M$, the kernel memory occupation can be estimated by:

$$N\,M\,w^2\,B,$$

where B is the number of bits used for the representation of every data value. On the other hand, in item (2) it results equal to:

$$N\,M\,w^2\,R^2\,B,$$

where R is the scaling factor. It is clear that if $R > 1$, for the same value of w, N, M and B, the approach (2) is more expensive in therms of memory occupation than (1).

Moreover, since approach (2) computes the kernel matrix only once, and it is further numerically optimized (truncation), it requires a smaller number of arithmetic operations than case (1).

More precisely, the numerical truncation of (2) consists in determining a threshold value $\overline{k} > 0$, useful to identify all the elements of the kernel matrix that can be neglected, being not significant in the output computation.

Recalling that the current thermographic data have been recorded by a thermal camera whose measurament resolution is $P := 10^{-2}$, the threshold value $\overline{k}$ can be expressed as

$$\overline{k} \;=\; \frac{4 \cdot 10^{-1}\,P}{w^2\,N\,M\,A},$$

where:

$$A \;:=\; \max\{a_{i,j} :\; i = 1, ..., N,\; j = 1, ..., M\}, \qquad I = (a_{i,j})_{i,j}.$$

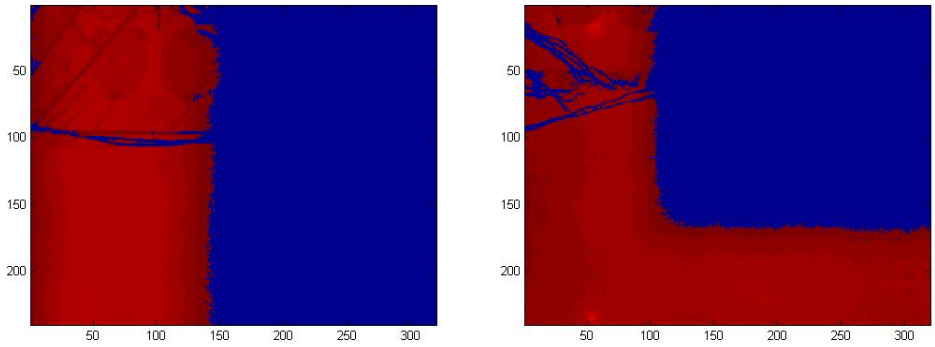

Figure 4.7. Thermal bridges extracted using the threshold temperatures calculated by the algorithm. The homogeneous dark areas represent the zones outside the thermal bridges.

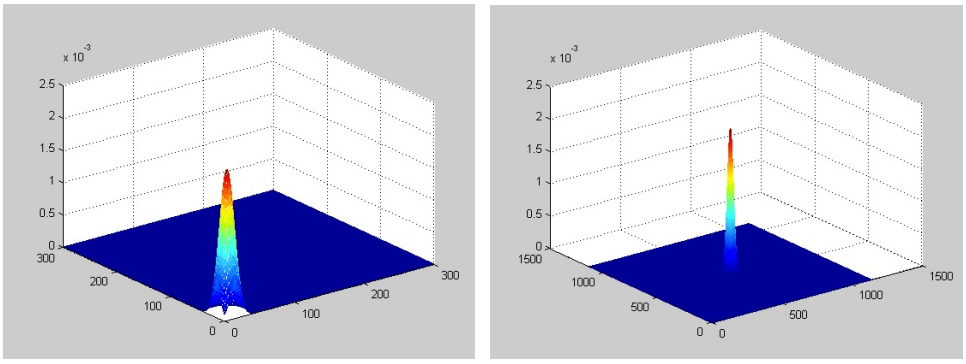

Figure 4.8. Example of the bidimensional Jackson type kernel $\mathcal{J}_2^2$: (left) calculated in a single step (1), (right) computed as in (2).

By this approach, all values which contribute (in the worse case) of an amount less or equal to $0.4\,P$ are neglected. For instance, in case of the two thermal bridges considered in this section, the value of A is equal to 22.5 and 22, respectively. Hence, recalling that $w = 15$, $N = 320$, and $M = 240$, we have that k is approximatively equal to 1.0288×10^{-11} and 1.0522×10^{-11}, respectively.

With the purpose to estimate the performance of the optimized version of the SK algorithm, the CPU time for the reconstruction of some data sets on a computer system equipped with i7 quad core CPU and 8 GB of ram has been measured, running Matlab© ver. R2014b on Windows© OP Windows 7©, Service pack 1, 64-bit parallelism. The rate of growth of the CPU time (expressed in seconds) has been considered in relation to the size $N \times M$, and to $w > 0$, for the two approaches.

From the results of Table 4.3, Table 4.4 and Table 4.5, it is clear that the approach (2) is faster than (1).

N x M	**w=1**	**w=4**	**w=9**	**w=25**	**w=100**	**w=400**
1×1	0.041870	0.040219	0.041105	0.038928	0.042712	0.039214
2×2	0.042075	0.042040	0.041391	0.041092	0.040991	0.042992
3×3	0.043006	0.042132	0.041864	0.044914	0.043080	0.048435
5×5	0.044211	0.048586	0.047370	0.048077	0.055869	0.060404
10×10	0.064676	0.066046	0.068574	0.074969	0.093118	0.227232

Table 4.3. CPU time for the data sets of the dimension listed in the first column, corresponding to each value of w, for the approach (1).

N x M	**w=1**	**w=4**	**w=9**	**w=25**	**w=100**	**w=400**
1×1	0.043561	0.040653	0.042252	0.043928	0.040932	0.041430
2×2	0.043919	0.044333	0.043065	0.043307	0.043592	0.045282
3×3	0.043289	0.043140	0.044113	0.043985	0.041659	0.044925
5×5	0.043000	0.043482	0.043960	0.044029	0.044554	0.045373
10×10	0.045015	0.045146	0.045300	0.046053	0.058119	0.147052

Table 4.4. CPU time for the data sets of the dimension listed in the first column, corresponding to each value of w, for the approach (2).

The advantage provided by the approach (2) appears more evident increasing the matrices size with respect to those considered in Table 4.3 and Table 4.4. Indeed, in Table 4.5 a matrix of dimension 20×20 has been tested, varying w.

Approach	**w=10**	**w=20**	**w=30**	**w=40**	**w=50**	**w=60**
(1)	0.236207	1.943428	4.20498	8.0352	12.3671	17.9449
(2)	0.14637	0.158876	0.18029	0.20343	0.23314	0.24744

Table 4.5. CPU time for a matrix of size 20×20 for both approaches (1) and (2), for different values of w.

The results of Table 4.5 have been plotted in Figure 4.9; the execution times using the algorithm based on (1) is longer than the corresponding ones based on (2).

On the basis of the previous considerations, approach (2) results faster than approach (1): for these reasons it has been preferred for the algorithmic implementation.

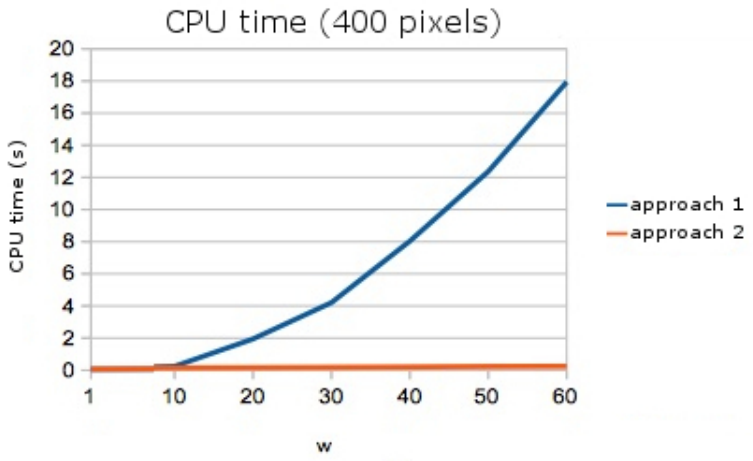

Figure 4.9. Comparison between the CPU time for the approaches (1) and (2), in function of $w > 0$ for an image of size 20×20.

The segmentation method described above is applied in order to detect the shape of thermal bridges of the building envelope from thermographic images. Moreover, it also allows to determine their heat losses, using a suitable *incidence factor of thermal bridge*, i.e., the index I_{tb}, previously introduced in [5, 6] and defined as

$$I_{tb} := \frac{\sum_{p=1}^{N} (T_i - T_p)}{N(T_i - T_{1D})}, \tag{4.1}$$

where T_i is the internal air temperature, T_p is the acquired surface temperature of the single pixel from the infrared camera, T_{1D} is the surface temperature of the undisturbed zone of the wall, evaluated with infrared camera as well, and N is the number of the pixels that compose an imaginary line (see, e.g., Figures 4.10, 4.11, 4.12) along the thermal bridge. The I_{tb} parameter is higher than one and gives information on the thermal bridge effects on the overall energy performance of the surface under investigation. The accuracy of I_{tb} depends on the resolution of the thermal map but it is independent from the length of the imaginary line chosen for its computation.

Its value has been calculated using the original thermographic images as well as by the corresponding reconstructed version after the application of the SK algorithm. In the first case, the shape of the thermal bridge has been manually delineated, while in the second case it has been automatically extracted by the proposed segmentation algorithm. The above achieved results have been compared with a reference index computed with the real data coming from the experimental setup, i.e., with the thermal parameters detected by heat flow meters and thermocouples in the hot box setup with controlled laboratory conditions. The I_{tb} index computed thanks to the application of the segmentation algorithm developed in this section provides results that are closer to the experimental reference I_{tb} respect to the user dependent not SK reconstructed methodology.

In this direction, I_{tb} estimations computed by the native method described in [5], i.e., from the original not-enhanced thermographic images, are 1.611 for pillar type thermal bridges, 1.467 for

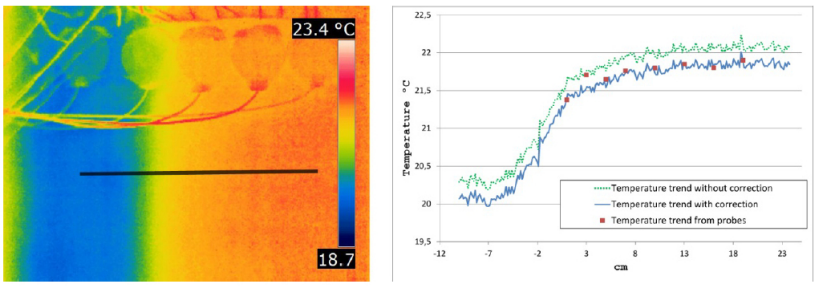

Figure 4.10. Thermographic image from pillar type thermal bridge. The black line has been used for the computation of the index I_{tb}. On the right, the values of I_{tb} resulting from the probes measurements I_{tb_probe} and from the thermographic technique proposed in [5] ($I_{tb\_infrared}$).

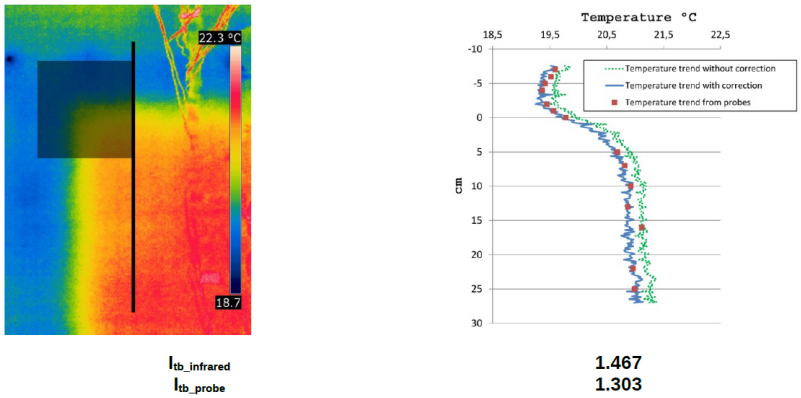

Figure 4.11. Thermographic image from beam-pillar joint type thermal bridge. The black line has been used for the computation of the index I_{tb}. On the right, the values of I_{tb} resulting from the probes measurements I_{tb_probe} and from the thermographic technique proposed in [5] ($I_{tb\_infrared}$).

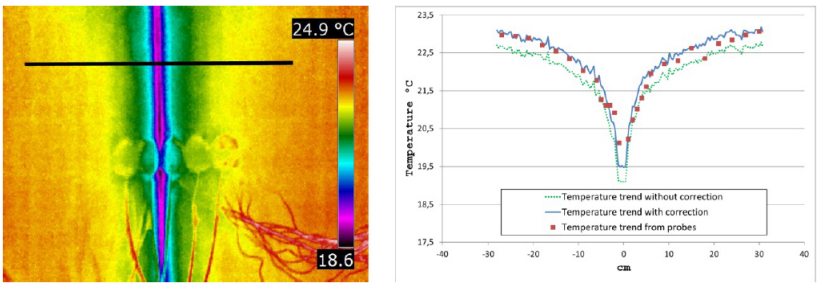

Figure 4.12. Thermographic image from wall-wall joint type thermal bridge. The black line has been used for the computation of the index I_{tb}. On the right the values of I_{tb} resulting from the probes measurements I_{tb_probe} and from the thermographic technique proposed in [5] ($I_{tb\_infrared}$).

beam-pillar joint thermal bridges and 1.369 for wall-wall joint thermal bridges. On the other hand, the corresponding ones, computed by the application of the proposed algorithm, respectively are 1.585, 1.462 and 1.378. The latter are closer to the reference values of I_{tb} (resulting by probes measurements), which are 1.439 and 1.303. Indeed, from the estimation of the ratio between the absolute errors for each one of the two different methods respect to the I_{tb} reference, it turns out that the new approach gains an improvement of around 15% and 4%, in case of pillar and beam-pillar joint thermal bridges type. For what concerns the wall-wall joint, the results are less significant, mainly because the geometrical issues related to the experimental setup: the impossibility to place the heat flux meters in proximity of the corner. In general, these results moves into the direction of a more accurate heat loss estimation. In the above examples, one of the main aspects that allows to achieve such improvement is given by the fact that the thermal bridges are generated by different materials: the proposed segmentation algorithm detects with a high accuracy the boundary separating the two different zones.

In conclusion, the above experimental results demonstrate the enhancement of the new procedure respect to the standard approach for the evaluation of heat losses in buildings. In addition, further advantages of the present algorithm consist in the possibility to automatically detect the exact geometry of the thermal bridge, eliminating the operator-induced dependencies.

4.2 Localization of Acoustic Bridges in 3D spaces [2]

In this section, a new procedure for three dimensional detection of sources of industrial noise and evaluation of their Euclidean distances in space is introduced. The above method is based on the analysis of acoustic and optical data recorded by an acoustic camera (AC) [36]. An AC is an array of microphones, distributed in a more or less regular geometry (preferably on a plane, depending on the specific application) to which an optic camera is connected. In this way an AC can provide sound pressure data rigidly connected with visual ones (see Figure 4.16). In order to improve the resolution of the data, interpolation and quasi interpolation algorithms for digital data processing have been used, such as the bilinear, bicubic and SK operators. According with the results of Section 2.3, the

[2] Results contained in this section have been submitted in [10, 11].

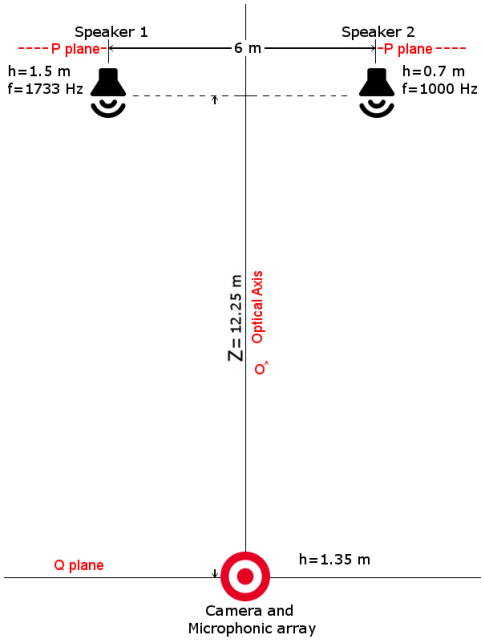

Figure 4.13. Experimental setup: planar view.

experimental tests show the best performance of SK algorithm compared to the other considered methods.

The main techniques available for the realization of acoustic cameras can be classified in beamforming (BF) and acoustic holography. BF uses the hypotesis of far field in the acoustic signal processing, assuming the signal propagating on a plane front from an infinitely diffused source. Compared to acoustic holography, BF is more suitable for investigation of big sized industrial implants. In this application field, BF is preferable compared to acoustic holography. A detailed description of the mathematical model for BF is provided in [12, 60, 99].

The experimental set up was built using two sources of noise: two speakers S_1 and S_2, respectively on the left and on the right of the AC optical axis O^A, have been tuned to sinusoidal signals of frequency of $f_1 = 1733Hz$ and $f_2 = 1000Hz$. S_1 and S_2 have been considered two point-sources with sound emitting element in the center of each speaker. Having two signals whose frequencies are not integer multiples each other, avoids any summation effects that could result from spurious harmonics superposition.

In Figure 4.13 the disposition of the two speakers is shown. The horizontal distance of S_1 and S_2 from O^A is 3000 mm, the height of S_1, $h_{S_1} = 1500$ mm, the height of S_2, $h_{S_2} = 700$ mm. The Euclidean distance between the sources is $d(S_1, S_2) \simeq 6053mm$. The acoustic camera used for the measurement is composed by a matrix of microphones rigidly connected with a single optical camera in the center of the system, so that all the sensors (microphones and optical camera) lie on the same plane Q. P indicates the (vertical) plane passing for S_1 and S_2 and parallel to Q (see Figure 4.13 again).

The distance between the acoustic camera AC and the plane P is $Z = 12250$ mm. Then, two measurements M_1 and M_2, of both sound pressure and corresponding visual scene have been

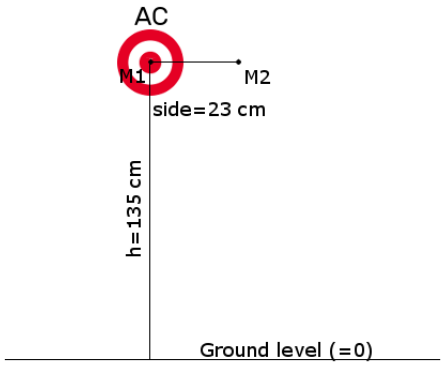

Figure 4.14. Acoustic camera shifting between M_1 and M_2.

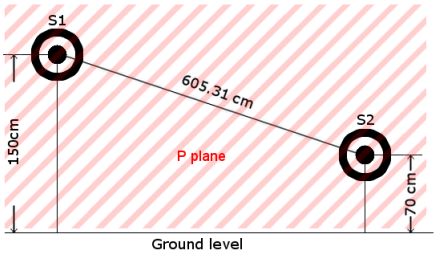

Figure 4.15. Experimental setup: frontal view of the P plane.

performed by AC. The data obtained from the above measurements have been stored in two matrices for each, M_1^O, M_2^O, M_1^A, M_2^A, the ones with apex O (standing for Optical) containing the optical data expressed by gray level 8 bit coded images, the other ones with apex A (standing for Acoustic) containing acoustic data expressed in dB. The measurement M_1 has been acquired with AC at a height of $h_{M_1} = 1350$ mm and O^A equidistant from the projection of S_1 and S_2 on the ground baseline (like in Figure 4.13), while the measurement M_2 has been acquired horizontally shifting AC of 230 mm to the right. Figure 4.14 shows the shifting procedure and Figure 4.15 the frontal view of the system to be measured.

The ground of the experimental setup is made of asphalt, with an acoustic reflectivity coefficient of 0.95 constant for any frequencies [56].

The size of the matrices M_1^A, M_2^A is 16×21, and the data have been stored in TDMS (Technical Data Management Solution by National Instruments$^{\text{TM}}$) files and expressed in dB with a scaling factor of $2 \cdot 10^5$ Pa. A normalization by this factor has been operated as follows

$$P_{dB} = 20 \cdot \log_{10} \frac{P_{TDMS}}{2 \cdot 10^5} ,$$

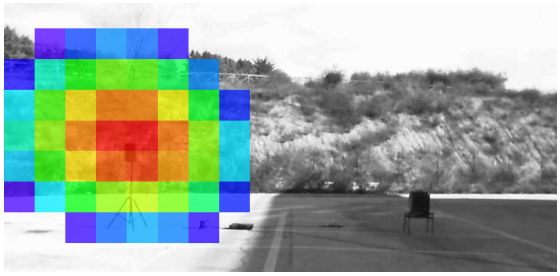

Figure 4.16. Acoustic resolution over the optical one. The colored square represent the acoustic "pixel" size.

where P_{TDMS} is any value of M_1^A or M_2^A.

From the matrices M_1^A, M_2^A it is possible to select, using certain software filters, the spectral components contained in a band of 100 Hz tuned to f_1 and f_2, obtaining from each one two new matrices denoted by $M_{1_{S_1}}^A$, $M_{1_{S_2}}^A$, and $M_{2_{S_1}}^A$, $M_{2_{S_2}}^A$, respectively. By the above construction $M_{1_{S_1}}^A$, and $M_{2_{S_1}}^A$ contain the acoustic data from the speaker S_1, while $M_{1_{S_2}}^A$ and $M_{2_{S_2}}^A$ the acoustic data from the speaker S_2.

The matrices M_1^O and M_2^O consist of grayscale images of 1024×780 pixels; an acoustic "pixel" contained in one of M_j^A, $j = 1, 2$, approximately corresponds to a square of 48×48 optical pixels (see Figure 4.16). The acoustic camera guarantees a rigid superposition of the acoustic data with the optical ones.

In the whole post-processing procedure for the spatial individuation of the noise sources (the speakers S_1 and S_2) the correspondence "1 acoustic pixel = 48×48 optical pixels" holds.

In order to improve the resolution of the acoustic data, such that to each pixel of the optical acquisition can be assigned a single value of sound pressure, two standard bidimensional interpolation methods are used: bilinear and bicubic.

The aim of this section is to suggest a new method to improve the reconstruction results achieved by the above standard methods, using the SK quasi interpolation, theoretically more performing than standard interpolation algorithms.

In order to quantify the Euclidean distance $d(S_1, S_2)$ between S_1 and S_2, the estimation of Z, the distance between the plane of the sources and the acoustic camera (which in general is unknown) is needed and can be achieved from the available data using a triangulation procedure, similar to the one used for GPS localization of points on the Earth surface [88, 101, 90].

The knowledge of Z is necessary to quantify the corresponding dimension, in world units (mm), of a single pixel at that distance. Accordingly to 3D scene reconstruction from multiple measurements techniques, a pointwise correspondence between the values of $M_{1_{S_j}}^A$ and $M_{2_{S_j}}^A$, $j = 1, 2$ is needed. In this specific case, it is sufficient to find a match only between the maximum points of the above matrices, in which S_1 and S_2 are obviously localized. Thus

$$\mathcal{M}_\nu^1 := (i_{MAX_{M_{1_{S_\nu}}^A}}, j_{MAX_{M_{1_{S_\nu}}^A}}) := \arg\max_{i,j}\{M_{1_{S_\nu}}^A(i,j)\},$$

$i = 1, ..., 16$, $j = 1, ..., 21$, corresponds to

$$\mathcal{M}_\nu^2 := (i_{MAX_{M_{2_{S_\nu}}^A}}, j_{MAX_{M_{2_{S_\nu}}^A}}) := \arg\max_{i,j}\{M_{2_{S_\nu}}^A(i,j)\},$$

$\nu = 1, 2$.

S_1	Z (mm)	$d(S_1, S_2)(pixel)$	$E_d(pixels)$	$p_{size}(Z)$	$E_{p_{size}(Z)}(mm)$	$E_Z(mm)$	$E_{TOT}(mm)$
Raw	499928	10.198	490.058	496.58	484.48	487678	237425.14
Bilinear	10634.360	489.506	10.750	10.56	1.54	1615	16.52
Bicubic	13151.447	482.685	17.571	13.06	0.96	901	16.93
SK	11783.416	488.922	11.334	11.70	0.39	467	4.88

Table 4.6. Error estimation for S_1 considering raw data, bilinear, bicubic and SK reconstructions.

The Euclidean distance $d^* := d(\mathcal{M}_\nu^1, \mathcal{M}_\nu^2)$, $\nu = 1, 2$, in 3D scene reconstruction from multiple measurements, is called *disparity*, see, e.g., [18].

The estimation of Z can be obtained as follows:

$$Z = f \cdot \frac{b}{d^*}, \tag{4.2}$$

where f is the focal length of the camera, a characteristic constructive parameter and b is the amount of displacement of the AC position in M_1 and M_2. In this specific case $b = 230$ mm. For the calculation of f the method introduced by Zhang [128] and available for camera calibration in Matlab^{TM}has been used. This technique, together with the available data, provides $f = 2173.6$ pixel.

Since the value of the disparity changes on the bases of the interpolation and quasi interpolation techniques used for the acoustic matrices magnification, different estimation of Z are achieved.

Moreover, once Z is determined, it is possible to calculate the size of a single pixel, using the linear equation

$$p_{size}(Z) = p_{size}(D) \cdot \frac{D}{Z}, \tag{4.3}$$

where D is a depth for which the size $p_{size}(D)$ of a single pixel in mm is known; $p_{size}(Z)$ is the size of a pixel in mm at distance Z. From the previous 4.3 equation naturally descends the need to know the dimension of some reference objects inside the image.

Then, the numerical results achieved for each one of the used interpolation and quasi interpolation methods are given in Table 4.6: it shows the results of the estimations of Z (mm); $d(S_1, S_2)(pixel)$, i.e., the distance (in pixels) between S_1 and S_2; E_d, i.e., the number of wrong pixels between the reference of $d(S_1, S_2)(pixel)$ and its estimations; $p_{size}(Z)$, i.e., the size (in mm) of one single pixel at distance Z; $E_{p_{size}(Z)}$ (mm), i.e., the error between the reference value and its estimations for each single pixel; $E_{TOT} := E_d \cdot E_{p_{size}(Z)}$.

In particular, for what concerns the SK operator, the reconstructions have been performed with $w = 20$ and bidimensional Jakson type kernel $\mathcal{J}_{12}^2(x)$, obtaining an enhanced acoustic image with size increased by a scale factor of 48.

The simplest way to convert the error E_d, originally expressed in pixel, into mm, is to multiply it by the estimated pixel size $p_{size}(Z)$. This procedure is inaccurate, not taking into account the error on the estimation of $p_{size}(Z)$. In order to avoid this inaccuracy, E_{TOT} is introduced as the most correct index expressing and evaluating the goodness of the results. In this case, the SK algorithm performs better than the other proposed methods according to [48].

The same considerations can be repeated in the case of the following relative errors:

$$E_{r_d} = \frac{E_d(pixels)}{d(S_1, S_2)(pixel)}, \tag{4.4}$$

$$E_{r_Z} = \frac{E_Z(mm)}{Z_{ref}}, \tag{4.5}$$

S_1	Z (mm)	$d(S_1, S_2)(pixel)$	E_{r_d} (4.4)	$E_{r_Z}(2)$ (4.5)	$E_{r_{p_{size}(Z)}}$ (4.6)	$E_{r_{TOT}}$ (4.7)
Bilinear	10634.360	489.506	0.021	0.131	0.127	0.0027
Bicubic	13151.447	482.685	0.035	0.073	0.080	0.0028
SK	11783.416	488.922	0.022	0.038	0.032	0.0007

Table 4.7. Error estimation for S_1 in case of raw data, bilinear, bicubic and SK reconstructions. The columns have the same meaning that in table 4.6 except that now the introduced relative errors (1), (2), (3), (4) are shown.

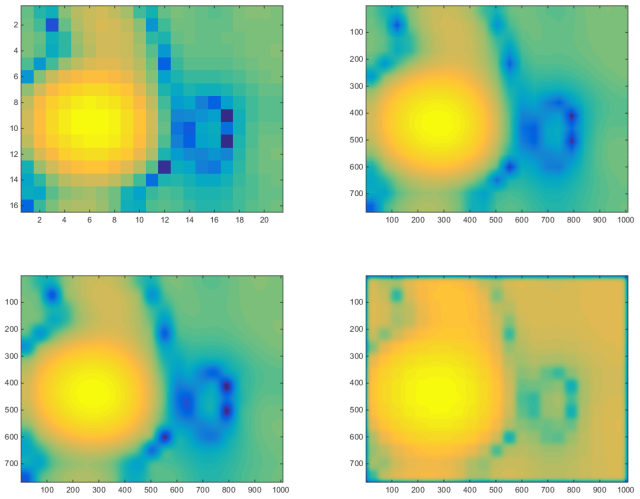

Figure 4.17. From left to right, top to down: raw data of $M^A_{1_{S_1}}$, bilinear interpolation of $M^A_{1_{S_1}}$, bicubic interpolation of $M^A_{1_{S_1}}$, SK quasi interpolation of $M^A_{1_{S_1}}$.

$$E_{r_{p_{size}(Z)}} = \frac{E_{p_{size}(Z)}(mm)}{p_{size}(D)(mm)}, \tag{4.6}$$

$$E_{r_{TOT}} = E_{r_d} \cdot E_{r_{p_{size}(Z)}}, \tag{4.7}$$

where E_{r_d} is compared to the reference distance $d(S_1, S_2)$, $E_{r_{p_{size}(Z)}}$ to the reference size $p_{size}(D)(mm)$, and E_{r_Z} to $Z_{ref} = 12250\ mm$. Results are shown in Table 4.7.

In Figures 4.17 and 4.18 the planar distributions of sound pressures are shown before and after the application of the interpolation and quasi interpolation methods.

In Figures 4.19 and 4.20 the three dimensional distributions of sound pressures are shown before and after the application of the interpolation and SK quasi interpolation methods.

For what concerns S_2, the results are different. Due to the reduced height of the speaker $h_{S_2} \simeq \frac{h_{S_1}}{2}$, to the not directivity of S_2 and to the reflectivity coefficient of the asphalt, the estimation of Z results evidently wrong. This error is caused by the reflections occurring on the ground at a distance that is half of the distance of S_1 from the acoustic camera, see table 4.8. In the case of S_1 the contributions of the reflections are negligible, being the sound source distant enough from the asphalt ground and being the sound waves enough attenuated, such that they do not influence the estimation of the Z. Moreover, in accordance with the dependence from the height of the speakers,

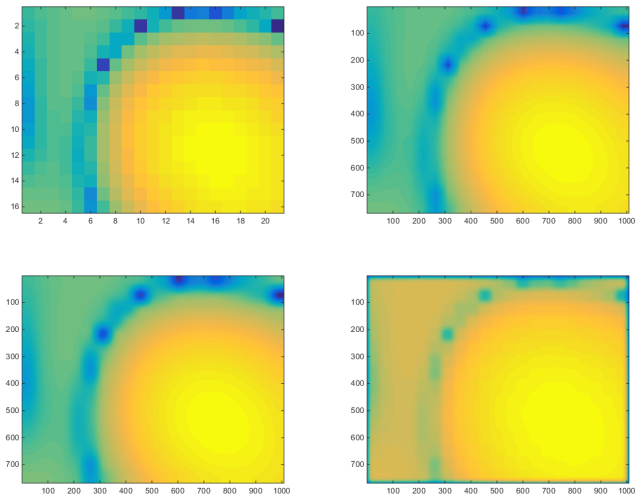

Figure 4.18. From left to right, top to down: raw data of $M^A_{1_{S_2}}$, bilinear interpolation of $M^A_{1_{S_2}}$, bicubic interpolation of $M^A_{1_{S_2}}$, SK quasi interpolation of $M^A_{1_{S_2}}$.

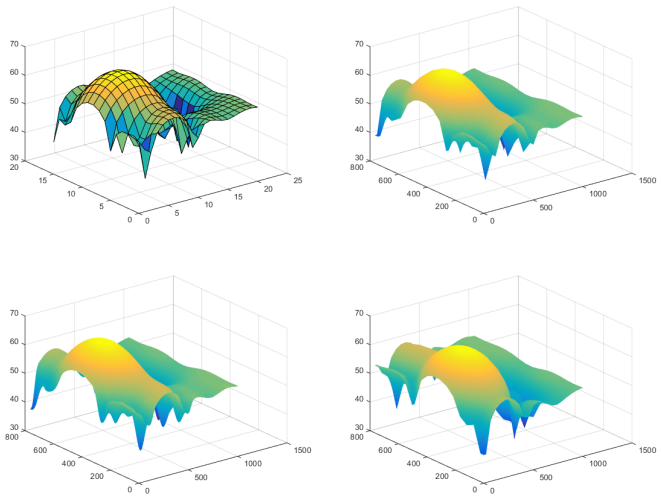

Figure 4.19. From left to right, top to down: three dimensional raw data of $M^A_{1_{S_1}}$, bilinear interpolation of $M^A_{1_{S_1}}$, bicubic interpolation of $M^A_{1_{S_1}}$, SK quasi interpolation of $M^A_{1_{S_1}}$.

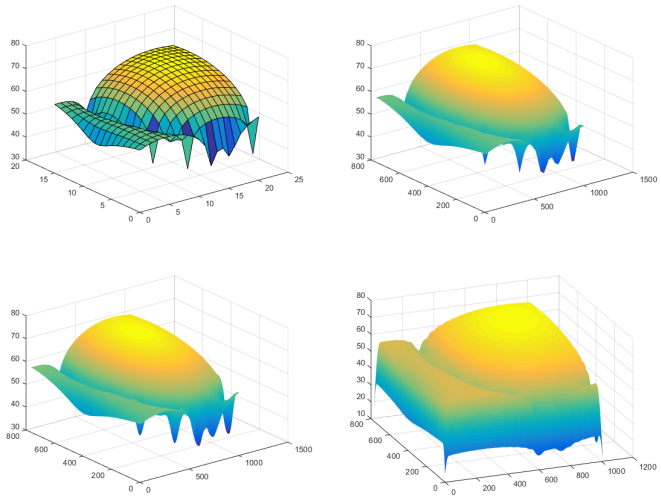

Figure 4.20. From left to right, top to down: three dimensional raw data of $M^A_{1_{S_2}}$, bilinear interpolation of $M^A_{1_{S_2}}$, bicubic interpolation of $M^A_{1_{S_2}}$, SK quasi interpolation of $M^A_{1_{S_2}}$.

S_2	Z (mm)
Raw	249964
Bilinear	5207.583
Bicubic	6096.683
SK	5434

Table 4.8. Distance estimation relative to S_2 for raw data, bilinear, bicubic and Sampling Kantorovich interpolated data. Z (mm) is the achieved depth of the plane of the source S_2.

the estimation of Z for S_2 is approximately half of what resulted for S_1.

Thanks to triangulation techniques the location of the sources of noise in a 3D orthogonal system is correctly identified. The poor resolution of the microphonic array poses the need for the introduction of interpolation or quasi interpolation methods (standard bilinear and bicubic interpolation together with SK quasi interpolation methods). Numerical results show that by means of the data enhanced with the SK algorithm, a more accurate detection of noise sources is possible compared to what achieved by means of the standard bilinear and bicubic interpolation (see [10, 11]), as easily deductible from the values of E_{TOT} in Tables 4.6 and 4.7.

Conclusions

The aim of this thesis has been the investigation and the understanding of the Sampling Kantorovich operators in view of real-world practical applications. In this last section a summary of what has been developed is reported.

Sampling Kantorovich operators have been introduced in mathematical literature with the aim to reconstruct functions not necessarily continuous. Firstly, one dimensional formulation and its extended multidimensional theory has been developed. Thanks to the achieved theoretical results and their implementation, reconstruction of two dimensional signals has been possible. From a physical point of view, the most meaningful advantage introduced by the SK operators is a precise modeling of the sampling process, if compared with previous formulations of the sampling theorems (WKS and Generalized). This modeling, based on a mean process around each sample, reduces, by construction, the time jitter error, connected with the practical impossibility to realize an exact equi-spaced sampling. SK operators have seen to perform like low pass filters, reducing high frequency noise, inevitably present in every real-world measurement process.

A comparison with other interpolation and quasi-interpolation methods, well known in literature, has been done: the achieved results have shown better quantitative performances of the SK algorithm with respect to the other methods [48].

The experimental results encouraged the application of SK operators in medical as in engineering fields.

From the medical point of view, the individuation of the pervious lumen of the aorta artery in presence of ateroma and without the introduction of contrast medium has been possible with a good localization of the occluded areas [39, 46, 40, 47]. The procedure, integrated with Digital Image Processing algorithms, has shown great performances, measured by specific indexes of similarity, compared to the gold standard contrast medium reference. To the knowledge of the author, at the present time, this seems to be the first attempt to segment the pervious lumen of aorta artery without contrast medium introduction.

In the ophtalmological field, SK algorithm has been used to improve the visualization of OCT images of the Superficial Capillary Plexus (SCP) as of the Choriocapillaris tissue (CC). The low-pass filtering properties of the SK method processed the images suppressing the high frequency noise, allowing as to improve the final quality, as to individuate and measure the number of anatomical connected vessels in the ocular fundus. Thanks to this, a more accurate visual diagnosis and a quantification of the rate of interconnection for the vessels have been possible, resulting in a more precise early individuation of pathologies.

Diagnostic procedures are important, as well, in the engineering field: for this reason the SK algorithm has been used to evaluate the thermal bridges extension in buildings [7, 8] and the three-dimensional localization, in space, of noise sources in acoustically polluted environments [10, 11]. In both cases the results overpassed the quality achieved using other standard methods, even in this cases confirming the theoretical performances of SK operators.

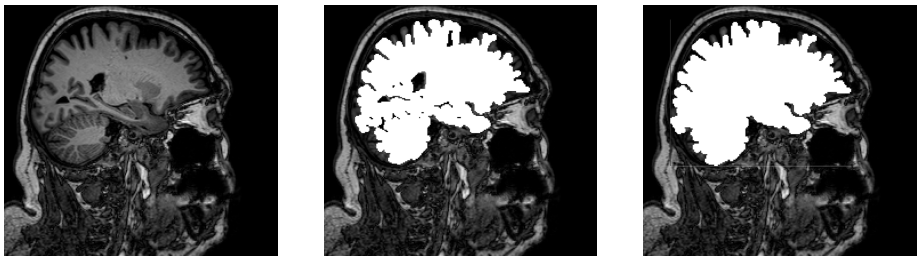

Figure 4.21. Sagittal section of human head. From left to right: the original MRI acquisition; the brain segmentation (in white) on the original MRI; the brain segmentation (in white) on the SK reconstruction with $R = 2$. From the anatomy of the brain, the improvement in the case of SK reconstruction is evident.

As a future research, a trial originated by the work developed in this thesis about the localization of the pervious lumen in aortic diseases, is going on to improve the achieved results, also considering the development of new segmentation methods based on Neural Networks.

Moreover, other planned researches, interested by the application of the Sampling Kantorovich operators, will investigate the brain segmentation in Magnetic Resonance Imaging (MRI) for the precocious Alzheimer's disease diagnosis (see Fig. 4.21 for an example of a preliminary work).

Bibliography

[1] I. Abraham, R. Abraham, M. Bergounioux, G. Carlier, Tomographic reconstruction from a few views: a multi-marginal optimal transport approach, Appl. Math. Optim., 75, (2017), 55-73.

[2] G. Allasia, R. Cavoretto, A. De Rossi, A class of spline functions for landmark-based image registration, Math. Methods Appl. Sci. 35 (2012), 923-934.

[3] L. Angeloni, D. Costarelli, G. Vinti, A characterization of the convergence in variation for the generalized sampling series, Annales Academiae Scientiarum Fennicae Mathematica, 43, (2018), 755-767.

[4] I. Arganda-Carreras, C. O. S. Sorzano, R. Marabini, J. M. Carazo, C. Ortiz-de Solorzano, J. Kybic, Consistent and Elastic Registration of Histological Sections using Vector-Spline Regularization, Lecture Notes in Computer Science, CVAMIA: Computer Vision Approaches to Medical Image Analysis, 4241/2006, (2006), 85-89.

[5] F. Asdrubali, G. Baldinelli, Thermal transmittance measurements with the hot box method: calibration, experimental procedures, and uncertainty analyses of three different approaches. Energy Build 43, (2011), 1618-26.

[6] F. Asdrubali, G. Baldinelli, F. Bianchi, A quantitative methodology to evaluate thermal bridges in buildings. *Applied Energy* 97, (2012), 365-373.

[7] F. Asdrubali, G. Baldinelli, F. Bianchi, D. Costarelli, L. Evangelisti, A. Rotili, M. Seracini, G. Vinti, A model for the improvement of thermal bridges quantitative assessment by infrared thermography, Applied Energy, 211, (2018), 854-864.

[8] F. Asdrubali, G. Baldinelli, F. Bianchi, D. Costarelli, A. Rotili, M. Seracini, G. Vinti, Detection of thermal bridges from thermographic images by means of image processing approximation algorithms, Applied Mathematics and Computation, 317, (2018), 160-171.

[9] F. Asdrubali, G. Baldinelli, F. Bianchi, A.L. Pisello, Infrared thermography assessment of thermal bridges in building envelope: Experimental validation in a test room setup. *Sustainability* 6 (10), (2014), 7107-7120.

[10] F. Asdrubali, G. Baldinelli, F. Bianchi, D. Costarelli, F. D'Alessandro, F. Scrucca, M. Seracini, G. Vinti, Innovative techniques for the improvement of industrial noise sources identification by acoustic holography and beamforming, submitted (2020).

[11] F. Asdrubali, G. Baldinelli, F. Bianchi, D. Costarelli, F. D'Alessandro, F. Scrucca, M. Seracini, G. Vinti, Mathematical models for the improvement of detection techniques of industrial noise sources from acoustic images, submitted (2020).

[12] M. R. Bai, J. Lee, Industrial noise sources identification by using an acoustic beamforming system, Journal of Vibration and Acoustics, 120 (2), (1998), 426-433.

[13] G. Baldinelli, F. Bianchi, A. Presciutti, A. Rotili, Transient Heat Transfer in Radiant Floors: A Comparative Analysis between the Lumped Capacitance Method and Infrared Thermography Measurements. J. Imaging 2 (3) 22, (2016), 1-10.

[14] I. Bankman, Handbook of Medical Image Processing and Analysis, Academic Press Inc., (2011), 1000.

[15] C. Bardaro, P. L. Butzer, R. L. Stens and G. Vinti, Kantorovich-type generalized sampling series in the setting of Orlicz spaces, Sampling Theory in Signal and Image Processing, 6 (1), (2007), 29-52.

[16] C. Bardaro, I. Mantellini, Voronovskaya formulae for Kantorovich type generalized sampling series, International Journal of Pure and Applied Mathematics, 62 (3), (2010), 247-262.

[17] C. Bardaro, J. Musielak, G. Vinti, Nonlinear Integral Operators and Applications, De Gruyter Series in Nonlinear Analysis and Applications 9, (2003), 213.

[18] S. T. Barnard, W. B. Thompson, Disparity Analysis of Images, IEEE Transactions on Pattern Analysis and Machine Intelligence, 1-2 (4), (1980), 333-340.

[19] K. A. Berthe, K. J. Vinoy, A new method for segmentation using fractal properties of images, International Journal of Electronics & Communication Technology, 2 (4), (2011), 23-28.

[20] T. Blu, M. Unser, Quantitative Fourier Analysis of Approximation Techniques: Part I - Interpolators and Projectors, IEEE Transactions on Signal Processing, 47 (10), (1999), 2783-2795.

[21] T. Blu, M. Unser, Quantitative Fourier Analysis of Approximation Techniques: Part II - Wavelets, IEEE Transactions on Signal Processing, 47 (10), (1999), 2796-2806.

[22] S. Boccardi, G. M. Carlomagno, C. Meola, An Excursus on Infrared Thermography Imaging, Journal of Imaging, 2 (36), (2016), 1-16.

[23] S. Boccardi, G. M. Carlomagno, C. Meola, The added value of infrared thermography in the measurement of temperature-stress coupled effects, Sensors and Transducers, 201 (6), (2016), 43-51.

[24] J. L. Brown, On the error in reconstructing a non-bandlimited function by means of the bandpass sampling theorem, Journal of Mathematical Analysis and Applications, 18 (1), (1967), 75-84, 1.

[25] M. Brown, R. Szeliski, S. Winder, Multi-Image Matching Using Multi-Scale Oriented Patches, Proceedings of the 2005 IEEE Computer Society Conference on Computer Vision and Pattern Recognition, 1, (2005), 510-517.

[26] P. L. Butzer, P. J. S. G. Ferreira, R. J. Higgins, G. Schmeisser, R. L. Stens, The sampling theorem, Poisson's summation formula, general Parseval formula, reproducing kernel formula and the Paley-Wiener theorem for bandlimited signals-their interconnections, Appl. Anal., (3-4), (2011), 431-461.

[27] P. L. Butzer, A. Fisher, R. L. Stens, Generalized sampling approximation of multivariate signals: theory and applications, Note di Matematica, 10 (1), (1990) 173-191.

[28] P. L. Butzer, J. R. Higgins, R. L. Stens, Classical and Approximate sampling theorems; studies in $L^p()$ and the uniform norm, J. Approx. Theory, 137, (2005), 250-263.

[29] P. L. Butzer, R. J. Nessel, Fourier Analysis and Approximation I, Academic Press, (1971), 554.

[30] P. L. Butzer, S. Ries, R. L. Stens, Approximation of continuous and discontinuous functions by generalized sampling series, J. Approx. Theory, 50, (1987), 25-39.

[31] P. L. Butzer, W. Splettstö ßer, R. L. Stens, The sampling theorem and linear prediction in signal analysis, Jahresber. Deutsch. Math.-Verein., 90, (1988), 1-70.

[32] P. L. Butzer, R. L. Stens, Linear prediction by samples from the past, Advanced Topics in Shannon Sampling and Interpolation Theory, (1993), 157-183.

[33] G. M. Carlomagno, G. Cardone, Infrared thermography for convective heat transfer measurements, Experiments in Fluids, 49 (6), 2010, 1187-1218.

[34] R. E. Carlson, F. N Fritsch, An Algorithm for monotone piecewise bicubic interpolation, SIAM J. Numer. Anal., 26 (1), (1985), 230-238.

[35] M. J. Chen, C. H. Huang, W. L. Lee, A fast edge-oriented algorithm for image interpolation, Image and Vision Computing, 23 (9), (2005), 791-798.

[36] J. Christensen, J. Hald, J. MÃ¸rkholt, A. Schuhmacher et al., A Review of Array Techniques for Noise Source Location, SAE Technical Paper 2003-01-1691, (2003), 1-9.

[37] Z. Chu, H. Zhou, Y. Cheng, Q. Zhang, R. K. Wang, Improving visualization and quantitative assessment of choriocapillaris with swept source OCTA through registration and averaging applicable to clinical systems, Nature Scientific Reports, 8:16826, (2018), 1-13.

[38] C. K. Chui, and H. Diamond, A natural formulation of quasi-interpolation by multivariate splines. Proc. American Math. Society, 99 (4), (1987), 643-646.

[39] E. Cieri, B. Fiorucci, D. Costarelli, G. Isernia, M. Seracini, G. Simonte, G. Vinti, Computed Tomography Postprocessing for Abdominal Aortic Aneurysm Lumen Recognition in Unenhanced Examinations, Annals of Vascular Surgery, 60, (2018), 407-414.

[40] E. Cieri, B. Fiorucci, D. Costarelli, G. Isernia, M. Seracini, G. Simonte, G. Vinti, An Automatized Algorithm to Evaluate the Patent Aortic Lumen in Non Contrast Computed Tomographies, European Journal of Vascular and Endovascular Surgery, vol. 58, 6, (2019), 275-276.

[41] F. Cluni, D. Costarelli, A.M. Minotti, G. Vinti, Enhancement of thermographic images as tool for structural analysis in earthquake engineering, NDT & E International, 70, (2015), 60-72.

[42] F. Cluni, D. Costarelli, A.M. Minotti and G. Vinti, Applications of sampling Kantorovich operators to thermographic images for seismic engineering, J. Comput. Anal. Appl. 19 (4), (2015), 602-617.

[43] L. Condat, T. Blu, M. Unser, Beyond interpolation: optimal reconstruction by quasi interpolation, IEEE Trans. Image Proc., 16, (2007), 1195-1206.

[44] D. Constales, H. De Bie, P. Lian, A new construction of the Clifford-Fourier kernel, Journal of Fourier Analysis and Applications, 23 (2) (2017), 462-483.

[45] D. Costarelli, A. M. Minotti, G. Vinti, Approximation of discontinuous signals by sampling Kantorovich series, Journal of Mathematical Analysis and Applications, 450 (2), (2017), 1083-1103.

[46] D. Costarelli, M. Seracini, G. Vinti, Approximation problems for digital image processing and applications, Computational Science and Its Applications - O. Gervasi et al. (Eds.): ICCSA 2018, Springer International Publishing AG, part of Springer Nature, (2018), 1-13.

[47] D. Costarelli, M. Seracini, G. Vinti, A segmentation procedure of the pervious area of the aorta artery from CT images without contrast medium, Mathematical Methods in the Applied Sciences, 43 (1), (2020), 114-133.

[48] D. Costarelli, M. Seracini, G. Vinti, A comparison between the sampling Kantorovich algorithm for digital image processing with some interpolation and quasi interpolation methods, Applied Mathematics and Computation, 374, (2020), 125046, 18 pp.

[49] D. Costarelli, G. Vinti, Approximation by multivariate generalized sampling Kantorovich operators in the setting of Orlicz spaces, Bollettino U.M.I., 9 (IV), (2011), 445-468.

[50] D. Costarelli, G. Vinti, Degree of approximation for nonlinear multivariate sampling Kantorovich operators on some functions spaces, Numerical Functional Analysis and Optimization, 36 (8), (2015), 964-990.

[51] D. Costarelli, G. Vinti, Approximation by max-product neural network operators of Kantorovich type, Results in Mathematics, 69 (3), (2016), 505-519.

[52] D. Costarelli, G. Vinti, An inverse result of approximation by sampling Kantorovich series, Proc. Edinb.Math.Soc., 62 (1), (2019), 265-280.

[53] D. Costarelli, G. Vinti, Inverse results of approximation and the saturation order for the sampling Kantorovich series, Journal of Approximation Theory, 242, (2019), 64-82.

[54] H. T. Croft, K. J. Falconer, R. K. Guy, Unsolved Problems in Geometry, Springer-Verlag, (1991), 199.

[55] W.R. Crum, O. Camara, D. L. G. Hill, Generalized Overlap Measures for Evaluation and Validation in Medical Image Analysis, IEEE Transcations on Medical Imaging, 25 (11), (2006), 1451-1461.

[56] R. A. Cruz, C. R. Correa, G. A. Diaz-Ramirez, Acoustic properties of concrete modified with an asphalt/styrene butadiene emulsion, Journal of Physics: Confernce Series 1247 , 012036, (2019), 1-9.

[57] J. Czajkowska, C. Feinen, M. Grzegorzek, M. Raspe, R. Wickenhöfer, A New Aortic Aneurysm CT Series Registration Algorithm, Information Technologies in Biomedicine, 3 , (2014), 15-26.

[58] T. M. Deserno, Biomedical Image Processing, Biological and Medical Physics, Biomedical Engineering, Springer Heidelberg Dordrecht, London New York, (2011), 595.

[59] L. R. Dice, Measures of the amount of ecologic association between species, Ecology, 26, (1945), 297-302.

[60] H. Ding, H. Lu, C. Li , J. Jing, D. Mei, G. Chai, Localization and identification of three-dimensional sound source with beamforming based acoustic tomography, Proc. Mtgs. Acoust. 19, 065063, (2013).

[61] R. O. Duda, P. E. Hart, Pattern Classification and Scene Analysis, Wiley, (1973).

[62] P. Dutilleux, An implementation of the "algorithme á trous" to compute the wavelet transform, In: Wavelets, Springer Berlin Heidelberg, (1989), 298-304.

[63] M. A. Fischler, R. C. Bolles, Random sample consensus: a paradigm for model fitting with applications to image analysis and automated cartography. Communications of the ACM, 24 (6), (1981), 381-395.

[64] P. Flandrin, P. Goncalves, G. Rilling, Empirical mode decomposition as a filter bank, IEEE signal processing letters, 11 (2), (2004), 112-114.

[65] G. B. Folland, Fourier Analysis and its Applications, AMS, Pure and Applied Undergraduated Text, (2009), 433.

[66] J. Fourier, Théorie Analytique de la Chaleur, (1822), reprinted in Cambridge Library Collection - Mathematics, Cambridge University Press., (2009), 676.

[67] B. R. Ganapathy, D. Manimegalai, D. M. Sugantharathnam, Wavelets and ridgelets for biomedical image denoising, WSEAS Trans. on Systems 12 (3), (2013), 165-178.

[68] R. C. Gonzales, R. E. Woods, Digital Image Processing, Prentice Hall, (2008), 954.

[69] G. Golub, C. F. Van Loan, Matrix Computations, The Johns Hopkins University Press, (1983), 728.

[70] R. M. Haralick, K. Shanmugam, I. H. Dinstein, Textural Features for Image Classification, IEEE Transactions on Systems, Man, and Cybernetics, SMC-3 (6), (1973), 610-621.

[71] J. R. Higgins, Five short stories about the cardinal series, Bull. Amr. Math. Soc., 12 (1985), 45-89.

[72] J. R. Higgins, Sampling Theory in Fourier and Signal Analysis, Oxford Science Pubbl., Clarendon Press, (1996), 236.

[73] G. Içoz, A Kantorovich variant of a new type Bernstein-Stancu polynomials, Applied Mathematics and Computation, 218 (17), (2012), 8552-8560.

[74] P. Jaccard, Nouvelles recherches sur la distribution florale, Bulletin de la Societe Vaudoise des Scences Naturelles, 44, (1908), 223-270.

[75] T. Kaijser, Computing the Kantorovich distance for images, J. Math. Imaging Vision, 9, (1998), 173-191.

[76] D. J. Kang, A fast and stable snake algorithm for medical images, Pattern Recognition Letters, 20 (5), (1999), 507-512.

[77] J. N Kapur, P.K. Sahoo, and A.K. Wong, A new method for gray-level picture thresholding using the entropy of the histogram, Computer vision, graphics, and image processing, 29 (3), (1985), 273-285.

[78] M. Kass, A. Vitkin, D. Terzopoulos, Snakes: Active Contour Models, WSEAS Trans. on Signal Processing, 10, (2014), 288-300.

[79] R. G. Keys, Cubic Convolution Interpolation for Digital Image Processing, IEEE Transactions on Acoustics, Speech, and Signal Processing, 29 (6), (1981), 1153-1160.

[80] T. Kitasaka, K. Morib, J. Hasegawac, J. Toriwakia, K. Katadad, Automated Extraction of Aorta and Pulmonary Artery in Mediastinum from 3D Chest X-ray CT Images without Contrast Medium, Proceedings of SPIE, 4684, (2002), 1496-1507.

[81] A. Kivinukk, T. Metsmagi, On boundedness inequalities of some semi-discrete operators in connection with sampling operators, 2015 International Conference on Sampling Theory and Applications, SampTA 2015, (2015), 48-52.

[82] A. Kivinukk, and G. Tamberg, Interpolating generalized Shannon sampling operators, their norms and approximation properties, Sampling Theory in Signal and Image Processing, 8, (2009), 77-95.

[83] E. Klein, H. J. Metz, P. Stucki, Advances in Digital Image Processing Theory, Application, Implementation, Springer - USA, (1979), 332.

[84] V. A. Kotelnikov, On the transmission capacity of the "ether" and wire in electrocommunications, translated from the Russian by V. E. Katsnelson, Appl. Numer. Harmon. Anal., Modern sampling theory, Birkhäuser Boston, Boston, MA, (2001), 27-45.

[85] A. Krivoshein, M. A. Skopina, Multivariate sampling-type approximation, Analysis and Applications, 15 (4), (2017), 521-542.

[86] T. M. Lehmann, C. Gonner, K. Spitzer, Interpolation Methods in Medical Image Processing, IEEE Transactions on Medical Imaging, 18 (11), (1999), 1049-1075.

[87] D. G. Lowe, Distinctive Image Features from Scale-Invariant Keypoints, International Journal of Computer Vision, 60 (2), (2004), 91-110.

[88] M. A. Mahammed, A. I. Melhum, F. A. Kochery, Object distance measurement by stereo vision, International Journal of Science and Applied Information Technology, 2 (2), (2013), 5-8.

[89] E. H. W. Meijering, W. J. Niessen, M. A. Viergever, Quantitative evaluation of convolution-based methods for medical image interpolation, Medical Image Analysis, 5, (2001), 111-126.

[90] A. Mohamed, C. Yang, A. Cangelosi, Stereo vision based object tracking control for a movable robot head, IFAC-Papers On Line 49-5, (2016), 155-162.

[91] S. M. Mousavi, A. Naghsh, A. S. R. Abu-Bakar, Watermarking techniques used in medical images: a survey, J. Digit Imaging, 27, (2014), 714-729.

[92] J. Musielak, Orlicz Spaces and Modular Spaces, Springer-Verlag, Lecture Notes Math., (1983), 226.

[93] H. Nyquist, Certain factors affecting telegraph speed, Bell System Technical Journal, 3, (1924), 324-346.

[94] H. Nyquist, Certain topics in telegraph transmission theory, Trans. AIEE, 47, (1928), 617-644, reprint as classic paper in: Proc. IEEE, 90 (2), (2002), 280-305.

[95] E. Olson, Particle Shape Factors and Their Use in Image Analysis Part 1: Theory, Journal of GXP Compliance, 15 (3), (2011), 85-96.

[96] A. Oppenheim, R. W. Schafer J. R. Buch, Discrete-time Signal Processing, Prentice Hall, New Jersey, (1989), 870.

[97] O. Orlova, G. Tamberg, On approximation properties of generalized Kantorovich-type sampling operators, Journal of Approximation Theory, 201, (2016), 73-86.

[98] N. Otsu, A Threshold Selection Method from Gray-Level Histograms, IEEE Transactions on Systems, Man and Cybernetics, 9 (1), (1979), 62-66.

[99] T. Padois, M. A. Gaudreau, P. Marcotte, F. Laville, Identification of noise sources using a time domain beamforming on pneumatic, gas and electric nail guns, Noise Control Engineering Journal 67 (1), (2019), 11-22.

[100] J. A. Parker, R. V. Kenyon, D. E. Troxel, Comparison of interpolating methods for image resampling, IEEE Transactions on Medical Imaging, (2), (1983), 31-39.

[101] D. K. Patel, P. A. Bachani, N. R. Shah, Distance measurement system using binocular stereo vision approach, International Journal of Engineering Research & Technology, 2 (12), (2013), 2461-2464.

[102] N. Phansalkar, S. More, A. Sabale, M. Joshi, Adaptive Local Thresholding for Detection of Nuclei in Diversity Stained Cytology Images, International Conference on Communications and Signal Processing, (2011), 218-220.

[103] C. L. Philips, J. Parr, E. A. Riskin, Signals, Systems, and Transforms (4th Edition), Prentice Hall, (2007), 784.

[104] C. Ó. Sanchez Sorzano, P. Thévenaz, M. Unser, Elastic Registration of Biological Images Using Vector-Spline Regularization, IEEE Transactions on Biomedical Engineering, 52 (4), (2005), 652-663.

[105] L. Schwartz, Transformation de Laplace des distributions, Comm. SÃ©m. Math. Univ. Lund, (1952), 196-206.

[106] C. E. Shannon, A Mathematical Theory of Communication, The Bell System Technical Journal, 27, (1948), 379-423, 623-656.

[107] C. E. Shannon, Communication in presence of noise, Proc. I.R.E., 37, (1949), 10-21.

[108] V. Skala, Fast interpolation and approximation of scattered multidimensional and dynamic data using radial basis functions, WSEAS Trans. on Mathematics, 12 (5), (2013), 501-511.

[109] M.A. Skopina, Band-limited scaling and wavelet expansions, Applied and Computational Harmonic Analysis, 36 (1), (2014), 143-157.

[110] T. Takayama, D. Yamanouchi, Aneurysmal disease: the abdominal aorta, Surgical Clinics, 93 (4), (2013), 877-891.

[111] G. Tamberg, On truncation errors of some generalized Shannon sampling operators, Numerical Algorithms, 55 (2), (2010), 367-382.

[112] B. D. Thackray, A.C. Nelson, Semi-Automatic Segmentation of Vascular Network Images Using a Rotating Structuring Element (ROSE) with Mathematical Morphology and Dual Feature Thresholding, IEEE Transactions on Medical Imaging, 12 (3), (1993), 385-392.

[113] P. Thévenaz, U.E. Ruttimann, M. Unser, A Pyramid Approach to Subpixel Registration Based on Intensity, IEEE Transactions on Image Processing, 7 (1), (1998), 27-41.

[114] J. Tian, K. K. Ma, A survey on super-resolution imaging, Signal, Image and Video Processing, 5, (2011), 329-342.

[115] A. Uji, S. Balaubramaian, J. Lei, E. Baghdasaryan, M. Al-Sheikh, S. R. Sadda, Choricapillaris Imaging Usin Multiple En Face Optical Coherence Tomography Angiography Image Averaging, Jama Ophtalmology, 135 (11), (2017), 1197-1204.

[116] A. Uji, S. Balasubramanian, J. Lei, E. Baghdasaryan, M. Al-Sheikh, S.R. Sadda, Impact of Multiple En Face Image Averaging on Quantitative Assessment from Optical Coherence Tomography Angiography Images, Ophthalmology, 124 (7), (2017), 944-952.

[117] A. Uji , S. Ooto, M. Hangai, S. Arichika, N. Yoshimura, Image Quality Improvement in Adaptive Optics Scanning Laser Ophthalmoscopy Assisted Capillary Visualization Using B-spline-based Elastic Image Registration, Plos One, 8 (11), (2013), 1-13.

[118] M. A. Unser, Ten good reasons for using spline wavelets, Optical Science, Engineering and Instrumentation'97. International Society for Optics and Photonics, (1997), 422-431.

[119] M. A. Unser, Splines, A perfect fit for Signal and Image Processing, IEEE Signal Processing Magazine, (1997), 22-38.

[120] R. Verfurth, Error estimates for some quasi-interpolation operators, ESAIM: Mathematical Modelling and Numerical Analysis, 33 (4), (1999), 695-713.

[121] G. Vinti, A general approximation result for nonlinear integral operators and applications to signal processing, Applicable Analysis, 79, (2001), 217-238.

[122] G. Vinti and L. Zampogni, Approximation by means of nonlinear Kantorovich sampling type operators in Orlicz spaces, J. Approx. Theory, 161, (2009), 511-528.

[123] A. Vretblad, Fourier Analysis and its Applications, Springer-Verlag, (2003), 272.

[124] P. Weiss, An estimate of the error arising from misapplication of the sampling theorem, Amer. Math. Sot. Notices, 10, (1963), 351.

[125] O. Wink, W. J. Niessen, M. A. Viergever, Fast Delineation and Visualization of Vessels in 3-D Angiographic Images, IEEE Transactions on medical imaging, 19 (4), (2000), 337-346.

[126] E. T. Whittaker, On the functions which are represented by the expansion of the interpolation theory, Proc. Roy. Soc. Edinburgh, 35, (1915), 181-194.

[127] Y. Xie, J. Padgett, A. M. Biancardi, A.P. Reeves, Automated Aorta Segmentation in low-dose chest CT images, International Journal of Computer Assisted Radiology and Surgery, 9 (2), (2014) 211-219.

[128] Z. Zhang, A flexible new technique for camera calibration, IEEE Transactions on Pattern Analysis and Machine Intelligence, 22 (11), (2014), 1330-1334.

[129] L. Zhang, W. Wu, An edge-guided image interpolation algorithm via directional filtering and data fusion, IEEE Trans. Image Proc., 15 (8), (2006), 2226-2238.

[130] A. Zygmund, Trigonometric series, vol I and II, Cambridge Univ. Press, Third Edition, (2002), 784.